



University of Kentucky  
UKnowledge

---

Theses and Dissertations--Physics and  
Astronomy

Physics and Astronomy

---

2018

## PROBING THE LOW-X GLUON HELICITY DISTRIBUTION WITH DIJET DOUBLE SPIN ASYMMETRIES IN POLARIZED PROTON COLLISIONS AT $\sqrt{S} = 510$ GEV

Suvarna Ramachandran

University of Kentucky, [suvarna.r@uky.edu](mailto:suvarna.r@uky.edu)

Digital Object Identifier: <https://doi.org/10.13023/etd.2018.416>

[Right click to open a feedback form in a new tab to let us know how this document benefits you.](#)

---

### Recommended Citation

Ramachandran, Suvarna, "PROBING THE LOW-X GLUON HELICITY DISTRIBUTION WITH DIJET DOUBLE SPIN ASYMMETRIES IN POLARIZED PROTON COLLISIONS AT  $\sqrt{S} = 510$  GEV" (2018). *Theses and Dissertations--Physics and Astronomy*. 58.

[https://uknowledge.uky.edu/physastron\\_etds/58](https://uknowledge.uky.edu/physastron_etds/58)

This Doctoral Dissertation is brought to you for free and open access by the Physics and Astronomy at UKnowledge. It has been accepted for inclusion in Theses and Dissertations--Physics and Astronomy by an authorized administrator of UKnowledge. For more information, please contact [UKnowledge@lsv.uky.edu](mailto:UKnowledge@lsv.uky.edu).

## **STUDENT AGREEMENT:**

I represent that my thesis or dissertation and abstract are my original work. Proper attribution has been given to all outside sources. I understand that I am solely responsible for obtaining any needed copyright permissions. I have obtained needed written permission statement(s) from the owner(s) of each third-party copyrighted matter to be included in my work, allowing electronic distribution (if such use is not permitted by the fair use doctrine) which will be submitted to UKnowledge as Additional File.

I hereby grant to The University of Kentucky and its agents the irrevocable, non-exclusive, and royalty-free license to archive and make accessible my work in whole or in part in all forms of media, now or hereafter known. I agree that the document mentioned above may be made available immediately for worldwide access unless an embargo applies.

I retain all other ownership rights to the copyright of my work. I also retain the right to use in future works (such as articles or books) all or part of my work. I understand that I am free to register the copyright to my work.

## **REVIEW, APPROVAL AND ACCEPTANCE**

The document mentioned above has been reviewed and accepted by the student's advisor, on behalf of the advisory committee, and by the Director of Graduate Studies (DGS), on behalf of the program; we verify that this is the final, approved version of the student's thesis including all changes required by the advisory committee. The undersigned agree to abide by the statements above.

Suvarna Ramachandran, Student

Dr. Renee H. Fatemi, Major Professor

Dr. Christopher Crawford, Director of Graduate Studies

PROBING THE LOW-X GLUON HELICITY DISTRIBUTION WITH DIJET  
DOUBLE SPIN ASYMMETRIES IN POLARIZED PROTON COLLISIONS AT  
 $\sqrt{S} = 510$  GEV

---

DISSERTATION

---

A dissertation submitted in partial  
fulfillment of the requirements for  
the degree of Doctor of Philosophy  
in the College of Arts and Sciences  
at the University of Kentucky

By  
Suvarna Ramachandran  
Lexington, Kentucky

Director: Dr. Renee H Fatemi, Professor of Physics  
Lexington, Kentucky 2018

Copyright© Suvarna Ramachandran 2018

## ABSTRACT OF DISSERTATION

### PROBING THE LOW-X GLUON HELICITY DISTRIBUTION WITH DIJET DOUBLE SPIN ASYMMETRIES IN POLARIZED PROTON COLLISIONS AT $\sqrt{S} = 510$ GEV

The proton is a complex subatomic particle consisting of quarks and gluons, and one of the key questions in nuclear physics is how the spin of the proton is distributed amongst its constituents. Polarized deep inelastic scattering experiments with leptons and protons estimate that the quark spin contribution is approximately 30%. The limited kinematic reach of these experiments, combined with the fact that they are only indirectly sensitive to the electrically neutral gluon, means they can provide very little information about the gluon contribution to the spin of the proton. In contrast, hadronic probes, such as polarized proton collisions provide direct access to the gluon helicity distribution.

The production of jets in polarized proton collisions at STAR is dominated by quark-gluon and gluon-gluon scattering processes. The dijet longitudinal double spin asymmetry ( $A_{LL}$ ) is sensitive to the polarized parton distributions and may be used to extract information about the gluon contribution to the spin of the proton. Previous STAR jet measurements at  $\sqrt{s} = 200$  GeV show evidence of polarized gluons for gluon momentum fractions above 0.05. The measurement of dijet  $A_{LL}$  at  $\sqrt{s} = 510$  GeV will extend the current constraints on the gluon helicity distribution to low momentum fractions and allow for the reconstruction of the partonic kinematics. Information about the initial state momentum provides unique constraints on the functional form of the gluon helicity distribution, thus reducing the uncertainty on extrapolations to poorly constrained regions. This thesis will present the first measurement of the dijet  $A_{LL}$  at  $\sqrt{s} = 510$  GeV, from polarized proton data taken during the 2012 RHIC run.

KEYWORDS: Helicity,  $A_{LL}$

Author's signature: Suvarna Ramachandran

Date: November 4, 2018

PROBING THE LOW-X GLUON HELICITY DISTRIBUTION WITH DIJET  
DOUBLE SPIN ASYMMETRIES IN POLARIZED PROTON COLLISIONS AT  
 $\sqrt{S} = 510$  GEV

By  
Suvarna Ramachandran

Director of Dissertation: Renee H Fatemi

Director of Graduate Studies: Christopher Crawford

Date: November 4, 2018

To one of the happiest people I have ever met!

Renee,

Thank you for your patience, support and guidance all of these years.

Thank you for being the wonderful person that you are.

## ACKNOWLEDGMENTS

To my husband Jimin, I could not have done this without you. Thank you for being my rock, for always being my inspiration and for making me laugh in even the most stressful times during the past few years. To my parents and my brother, thank you for always encouraging me to pursue my dream.

I am very grateful to a lot of people for their help and support during the past few years of research. To Dr. Zilong Chang, Dr. Kevin Adkins and Dr. Grant Webb, thank you for always being so very generous with your time and resources. Thank you to Dr. Carl Gagliardi and Dr. Jim Drachenberg, for all your support and valuable suggestions throughout my research period at STAR. Thank you to Dr. Dmitry Kalinkin, Dr. Brian Page, Dr. Elke Aschenauer and Dr. Jerome Lauret for the very useful assistance during the time of my analysis. To Dr. Tim Gorringe, thank you for taking the time and helping me start my research in Experimental Particle Physics.

To Jasminka, thank you for your friendship.

# TABLE OF CONTENTS

Acknowledgments . . . . .	iii
List of Tables . . . . .	vi
List of Figures . . . . .	vii
Chapter 1 Motivation and Historical Introduction . . . . .	1
1.1 The Proton . . . . .	1
1.2 The Spin Puzzle . . . . .	3
1.3 Gluon Polarization at RHIC . . . . .	6
1.3.1 Dijet $A_{LL}$ at 510 GeV . . . . .	10
Chapter 2 RHIC and The STAR Detector . . . . .	14
2.1 The Relativistic Heavy Ion Collider . . . . .	14
2.1.1 Protons in RHIC . . . . .	14
2.2 The STAR Detector . . . . .	17
Chapter 3 Data Selection . . . . .	23
3.1 Dataset . . . . .	23
3.2 Triggers . . . . .	23
3.3 Event-Level Quality Analysis . . . . .	24
Chapter 4 Jet and Dijet Reconstruction . . . . .	29
4.1 Jets . . . . .	29
4.1.1 Jet Reconstruction . . . . .	29
4.1.2 <i>Anti</i> - $k_T$ Algorithm . . . . .	30
4.1.3 Jet-finding Cuts . . . . .	31
4.2 Dijets . . . . .	33
4.2.1 Underlying Event Subtraction . . . . .	33
4.2.2 Dijet Cuts . . . . .	35
Chapter 5 Monte Carlo Simulation . . . . .	40
5.1 Embedding . . . . .	41
5.2 Data - Embedding Comparison . . . . .	42
Chapter 6 Dijet Longitudinal Double Spin Asymmetry . . . . .	50
6.1 Introduction . . . . .	50
6.2 Calculation of $A_{LL}$ . . . . .	50
6.2.1 Spin Bits . . . . .	50
6.2.2 Definition of $A_{LL}$ . . . . .	51
6.2.3 Relative Luminosities . . . . .	52



6.2.4	Beam Polarization . . . . .	53
6.2.5	Detector Topologies . . . . .	54
6.3	False Asymmetries . . . . .	55
6.4	Corrections . . . . .	60
6.4.1	Invariant Mass Shift . . . . .	60
6.4.2	Trigger and Reconstruction Bias . . . . .	60
Chapter 7	Systematic Uncertainties . . . . .	64
7.1	Underlying Event and Relative Luminosity Systematic . . . . .	64
7.2	Dilution due to Vertex Finding . . . . .	67
7.3	Residual Transverse $A_{LL}$ Uncertainty . . . . .	67
7.4	Non-Collision Background Uncertainty . . . . .	67
7.5	Jet Energy Scale Uncertainties . . . . .	68
7.6	Trigger and Reconstruction Bias Errors . . . . .	72
Chapter 8	Results and Conclusions . . . . .	75
Appendix:	List Of Runs . . . . .	82
Bibliography	. . . . .	85
Vita	. . . . .	89

## LIST OF TABLES

3.1	Jet Patch Trigger Thresholds . . . . .	24
4.1	Track and tower cuts . . . . .	32
5.1	Simulation statistics for the 2012 analysis . . . . .	41
6.1	Spin configurations . . . . .	50
6.2	Detector Topologies . . . . .	54
7.1	The corrections and systematic uncertainties assigning parton dijet $M_{inv}$ to the detector-level dijet $M_{Inv}$ bins for the four topologies. $\delta M_{inv} = \langle M_{inv,parton} - M_{inv,detector} \rangle$ . All values are in $\text{GeV}/c^2$ . . . . .	73
7.2	The corrections and systematic uncertainties in $A_{LL}$ for dijet production. In addition to the uncertainties enumerated here, there are two that are common to all the points, a shift uncertainty of $\pm 0.00022$ associated with the relative luminosity measurement and a scale uncertainty of $\pm 6.5\%$ associated with the beam polarization. . . . .	74
8.1	$A_{LL}$ as a function of parton dijet $M_{Inv}$ (in $\text{GeV}/c^2$ ) in $\sqrt{s} = 510 \text{ GeV}$ $pp$ collisions. There is an additional $\pm 6.5\%$ scale uncertainty from the beam polarization that is common to all the measurements. . . . .	81

## LIST OF FIGURES

1.1	Combined HERA data . . . . .	2
1.2	Unpolarized PDFs . . . . .	3
1.3	Polarized PDFs . . . . .	5
1.4	Sub process Fractions . . . . .	6
1.5	2009 Inclusive Jet $A_{LL}$ . . . . .	8
1.6	Current knowledge of $\Delta G$ . . . . .	9
1.7	2012 Inclusive Jet $A_{LL}$ Preliminary . . . . .	10
1.8	x distributions from dijets and inclusive jets . . . . .	11
1.9	STAR 2009 Dijet $A_{LL}$ results . . . . .	12
2.1	RHIC Complex Layout . . . . .	15
2.2	STAR Detector . . . . .	17
2.3	Time Projection Chamber . . . . .	19
2.4	BEMC Tower Layout . . . . .	20
2.5	The STAR BBC . . . . .	21
2.6	The STAR VPD . . . . .	22
3.1	Average BEMC $E_T$ vs. Run Index . . . . .	25
3.2	Average BEMC $E_T$ vs. Run Index . . . . .	25
3.3	Average EEMC $E_T$ vs. Run Index . . . . .	26
3.4	Average EEMC $E_T$ vs. Run Index . . . . .	27
3.5	Average track $p_T$ vs. Run Index . . . . .	27
3.6	Average track $p_T$ vs. Run Index . . . . .	28
4.1	Off-Axis Cones . . . . .	34
4.2	Track $p_T$ vs jet $p_T$ ratio - Before cut . . . . .	36
4.3	Track $p_T$ vs jet $p_T$ ratio - After cut . . . . .	37
5.1	Partonic $p_T$ spectrum . . . . .	42
5.2	Leading jet $p_T$ . . . . .	43
5.3	Away-side jet $p_T$ . . . . .	43
5.4	Leading jet $\eta$ . . . . .	44
5.5	Away-side jet $\eta$ . . . . .	44
5.6	Leading jet $\phi$ . . . . .	45
5.7	Away-side jet $\phi$ . . . . .	45
5.8	Leading jet $R_T$ . . . . .	46
5.9	Away-side jet $R_T$ . . . . .	46
5.10	Dijet $M_{inv}$ . . . . .	47
5.11	Dijet $\Delta\phi$ . . . . .	48
5.12	Dijet $\Delta\eta$ . . . . .	48
5.13	Z Vertex . . . . .	49

6.1	$A_Y$ . . . . .	56
6.2	$A_B$ . . . . .	57
6.3	$A_{LS}$ . . . . .	58
6.4	$A_{US}$ . . . . .	59
6.5	Corrected $M_{inv}$ . . . . .	61
6.6	Parton level Dijet $A_{LL}$ . . . . .	62
6.7	Detector level Dijet $A_{LL}$ . . . . .	63
7.1	$A_{LL}$ from UE . . . . .	66
7.2	$\Delta M$ for various tunes . . . . .	70
7.3	Systematic Uncertainties . . . . .	71
7.4	UE contribution in data and simulation . . . . .	72
8.1	Dijet $x_1$ and $x_2$ . . . . .	76
8.2	$A_{LL}$ . . . . .	76
8.3	Dijet $x_1$ and $x_2$ . . . . .	77
8.4	$A_{LL}$ . . . . .	77
8.5	Dijet $x_1$ and $x_2$ . . . . .	78
8.6	$A_{LL}$ . . . . .	78
8.7	Dijet $x_1$ and $x_2$ . . . . .	79
8.8	$A_{LL}$ . . . . .	79

## Chapter 1 Motivation and Historical Introduction

### 1.1 The Proton

Rutherford discovered the atomic nucleus, which is composed of protons and neutrons. Since its discovery, experimental and theoretical physicists have been trying to understand and study its properties in detail. The simple "static quark model", where the proton consists of three massive stationary quarks, can reproduce many of the properties of the proton, such as the charge, magnetic moment and isospin, from the quantum numbers of the three quarks. However, according to this model, the spin of the proton is equal to the sum of the spins carried by the three quarks. This theory has been disproved by experimental results. In the 1970s the theory of Quantum Chromodynamics (QCD) was developed as the full theory of strong interactions, according to which quarks were confined inside the proton and their interactions were mediated by the massless gluons. These gluons, which are constantly being emitted and absorbed by the valence quarks, produce quark anti-quark pairs, collectively referred to as sea quarks. One of the essential concepts of QCD is that it allows for factorization of high-energy and low-energy contributions, and a combination of experiments and theory is needed to extract the pieces that cannot be calculated from first principles.

Early studies of the proton's internal structure utilized lepton-scattering experiments. Typically these experiments focused on elastic scattering with electrons, in which the electron transferred a small amount of momentum to the proton and the proton stayed intact. These measurements gave information about some of the very important properties of the proton, such as its charge radius. Deep inelastic scattering (DIS) experiments, where the lepton scatters elastically off the quarks instead of the proton, provided new insights into proton structure. The major advantage

of using leptons to probe the small-scale properties, is that leptons have no internal structure. Figure 1.1 shows the combined HERA data [1] for the inclusive neutral current (NC) electron-proton and positron-proton cross sections along with the fixed target data. It also shows the predictions of HERAPDF2.0 at next-to-leading order (NLO). The electron-proton scattering cross sections are related to the unpolarized parton distribution functions (PDF) convoluted with a hard scattering cross section that can be calculated in NLO perturbative QCD (pQCD). Note that the cross section data for a given  $x$  does not scale with  $Q^2$ ,  $x$  is the momentum fraction of the parton inside the proton and  $Q^2$  is the momentum transfer. The deviations from flat are the scaling violations due to gluon emission.

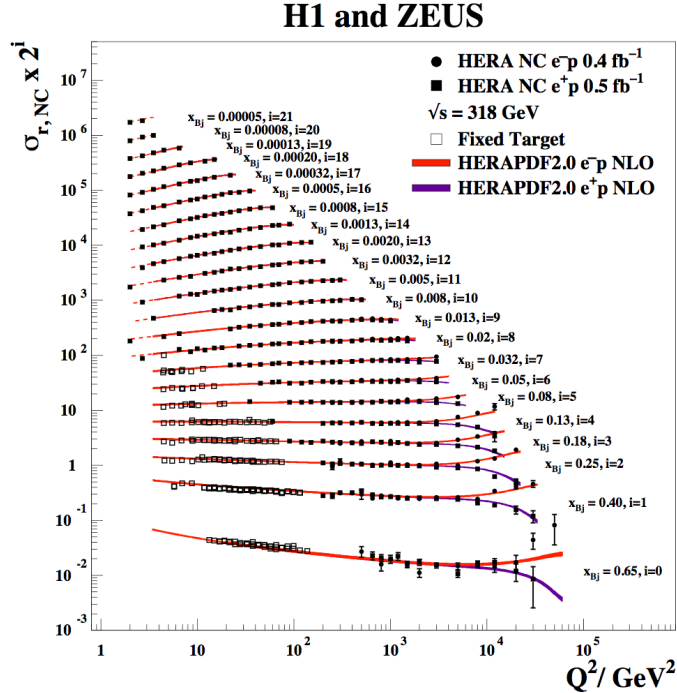


Figure 1.1: **Combined HERA data** - The combined HERA data for the inclusive NC  $e^- - p$  and  $e^+ - p$  cross sections along with the fixed target data. The predictions of HERAPDF2.0 at NLO are also shown.

Figure 1.2 [1] shows the extraction of the unpolarized PDFs for u and d, gluons and the sea quarks at next-to-leading order. The gluon and sea distributions are scaled down by a factor of 20.

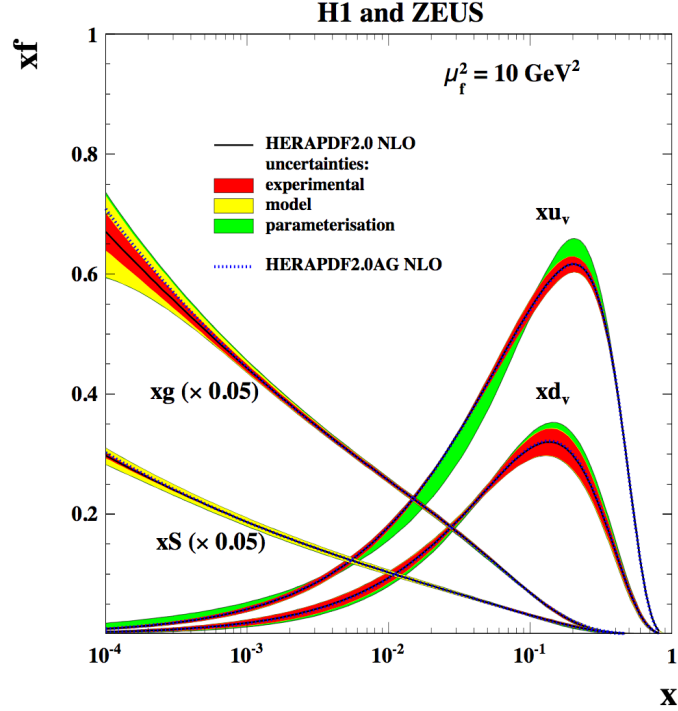


Figure 1.2: **Unpolarized PDFs** - The parton distribution functions for the u, d and sea quarks and the gluons of HERAPDF2.0 NLO are shown. The contributions from the sea quark and gluon distributions are scaled down by a factor of 20.

## 1.2 The Spin Puzzle

The spin of the proton was understood in great detail through similar experimental approaches using polarized deep inelastic scattering experiments, using both initial leptons and initial hadrons polarized [2]. In terms of the components from its constituents, namely quarks and gluons, the spin of the proton can be written as:

$$\frac{1}{2} = \frac{1}{2}\Delta\Sigma + \Delta G + L_Q + L_G \quad (1.1)$$

where  $\frac{1}{2}\Delta\Sigma$  and  $\Delta G$  are the spin contributions from the quarks and gluons and  $L_Q$  and  $L_G$  are the orbital angular momentum contributions [3].

The quark and gluon spin contributions can be written as:

$$\Delta\Sigma(Q^2) = \int_0^1 (\Delta u(x, Q^2) + \Delta\bar{u}(x, Q^2) + \Delta d(x, Q^2) + \Delta\bar{d}(x, Q^2) + \Delta s(x, Q^2) + \Delta\bar{s}(x, Q^2)) dx \quad (1.2)$$

$$\Delta G(Q^2) = \int_0^1 \Delta g(x, Q^2) dx \quad (1.3)$$

In the above equations,  $\Delta u$ ,  $\Delta d$  and  $\Delta s$  (and  $\Delta\bar{u}$ ,  $\Delta\bar{d}$  and  $\Delta\bar{s}$ ) are the polarized quark distributions and  $\Delta g$  is the polarized gluon distribution. The polarized (spin dependent) distributions characterize the distribution of momentum and spin of the quarks and gluons in the proton, and can be written as:

$$\Delta f(x, Q^2) = f^+(x, Q^2) - f^-(x, Q^2) \quad (1.4)$$

where  $f^+(x, Q^2)$  and  $f^-(x, Q^2)$  are the probabilities to find a parton with a momentum fraction  $x$  and spin polarized parallel and anti-parallel to that of the proton respectively.

While the Quark Parton Model predicted 100%, the inclusion of relativistic effects suggested that 75% of the spin of the proton comes from quarks. On the other hand, early experiments such as the EMC [4] showed negligible contributions from quarks, but this was just due to low statistics. Additional data from polarized deep inelastic scattering experiments have shed more light into the study of polarized quark distributions. Recent global analyses of polarized PDFs have shown that quark contribution to the spin of the proton is  $\sim 30\%$  [5] [6].

Figure 1.3 shows the polarized PDFs from DSSV [7], along with the uncertainty bands at  $Q^2 = 10$  GeV. These are extracted from data from deep inelastic scattering and semi-inclusive deep inelastic scattering. The distributions of the valence quarks



are very well constrained, while the constraints on the polarized gluon distributions are poor. Since there has never been a polarized electron-proton collider, it is very challenging to achieve the high precision seen in the unpolarized data for polarized experiments.

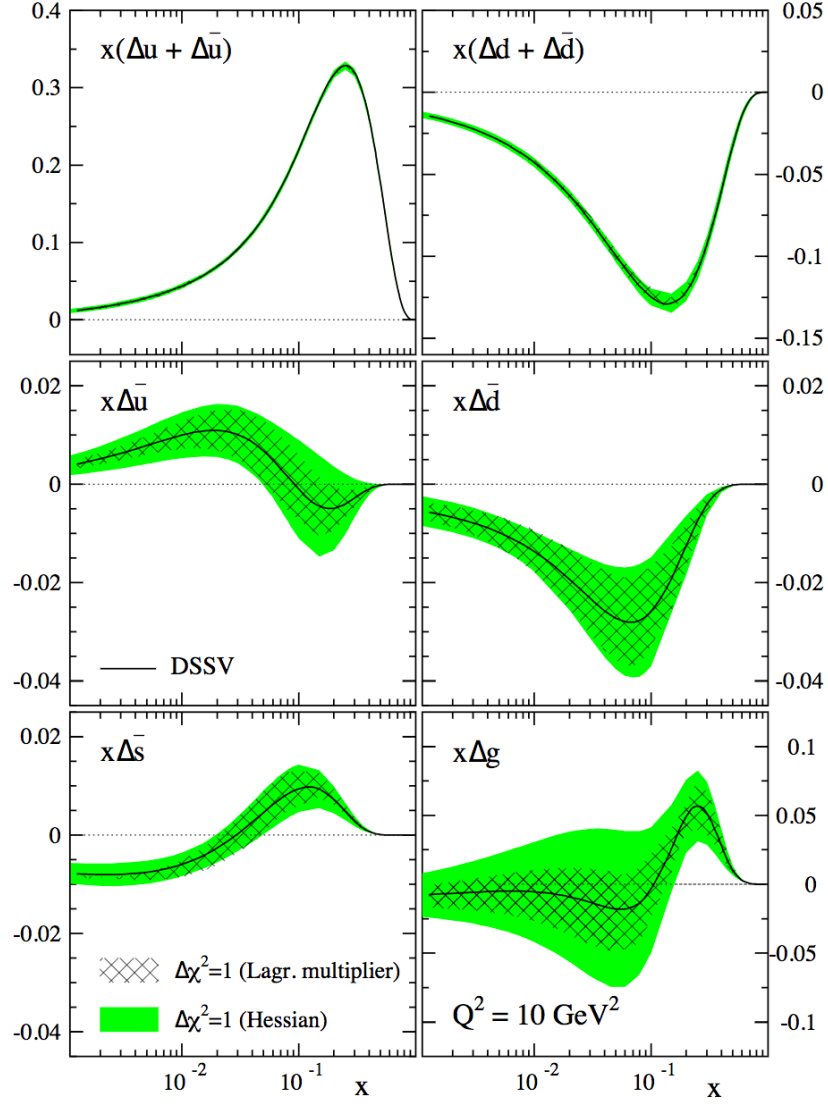


Figure 1.3: **Polarized PDFs** - The polarized parton distribution functions from DSSV for the u, d and sea quarks and the gluons along with the uncertainty bands are shown.

### 1.3 Gluon Polarization at RHIC

Since leptons do not directly couple to gluons, polarized DIS measurements have only an indirect access to the polarized gluon distributions. On the other hand, longitudinally polarized protons at RHIC can access  $\Delta g(x, Q^2)$  directly through quark-gluon and gluon-gluon scattering. The fractions of the leading order sub-processes as a function of jet  $x_T$  ( $= 2p_T/\sqrt{s}$ ) in proton-proton scattering are shown in Figure 1.4. Notice that gluon scattering processes dominate at low  $x_T$ . One of the observables sensitive to  $\Delta g(x, Q^2)$  in polarized proton collisions is the dijet longitudinal double spin asymmetry, denoted as  $A_{LL}$ .

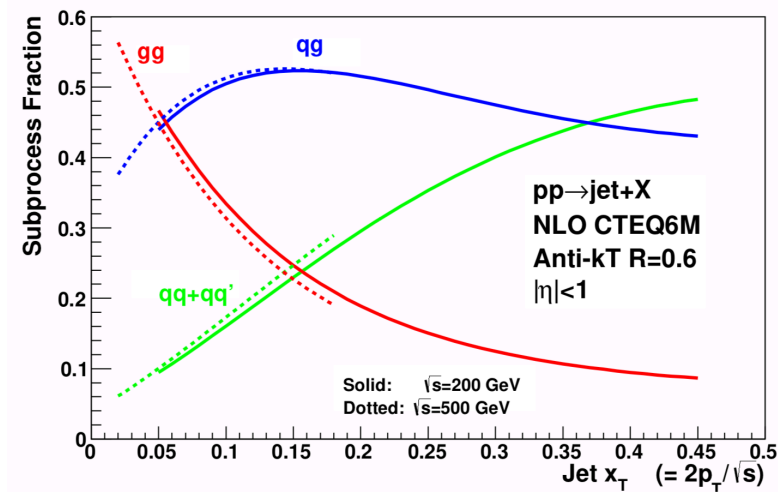


Figure 1.4: **Sub process Fractions** - The quark-quark, quark-gluon, and gluon-gluon sub process fractions for the inclusive jet production in  $pp$  collisions at  $\sqrt{s} = 200$  and  $500$  GeV, as a function of  $x_T = 2p_T/\sqrt{s}$  [8, 9].

$A_{LL}$  is defined as:

$$A_{LL} = \frac{\sigma^{++} - \sigma^{+-}}{\sigma^{++} + \sigma^{+-}} \propto \frac{\sum_{a,b} \Delta f_a \Delta f_b a_{LL}}{\sum_{a,b} f_a f_b} \quad (1.5)$$

where  $\sigma^{++}$  and  $\sigma^{+-}$  are the dijet cross sections with same and opposite helicities for the initial state protons.  $a$  and  $b$  denote quarks and gluons, and the summation leads to the three different subprocesses  $qq, qg$  and  $gg$  in the above expression.  $\Delta f_{a,b}$  are the polarized PDFs,  $f_{a,b}$  are the unpolarized PDFs and  $\hat{a}_{LL}$  is the partonic  $a_{LL}$ . The partonic  $a_{LL}$  is the longitudinal double spin asymmetry of the partons participating in the hard interaction.

The difference of the cross sections are related to the polarized PDFs convoluted with the partonic  $a_{LL}$ . The PDFs are the non-perturbative part that characterizes the spin structure of the proton and the  $\hat{a}_{LL}$  is the perturbative part that is currently calculated to NLO in pQCD. Inclusive hadrons, such as charged and neutral pions are also sensitive to  $\Delta g(x, Q^2)$ . But in that case, the expression in equation the above equation would also require a fragmentation function. This complicates the extraction of the gluon helicity distribution and motivates the use of jet observables for these types of measurements.

The 2009 inclusive jet double spin asymmetries, measured at  $\sqrt{s} = 200$  GeV, were the first evidence for non-zero gluon polarization in the proton. Figure 1.5 shows the STAR  $A_{LL}$  results, plotted as a function of the jet transverse momentum, corrected for detector and hadronization effects. The data are plotted for two pseudorapidity regions, assessing different regions of  $x$  and  $\cos\theta^*$  where  $\theta^*$  is the scattering angle of the hard partons in the center of mass frame. The partonic  $a_{LL}$  varies as a function of  $\cos\theta^*$ . The theoretical curves are generated using the jet  $A_{LL}$  code [9] that incorporates the PDFs extracted from various global analyses (a global analysis incorporates experimental measurements into a pQCD theoretical framework in order to extract PDFs). On this particular plot, all of the curves use some combination of inclusive and semi-inclusive lepton-proton scattering data but only DSSV had incorporated the inclusive jet and pion RHIC data [7, 10].

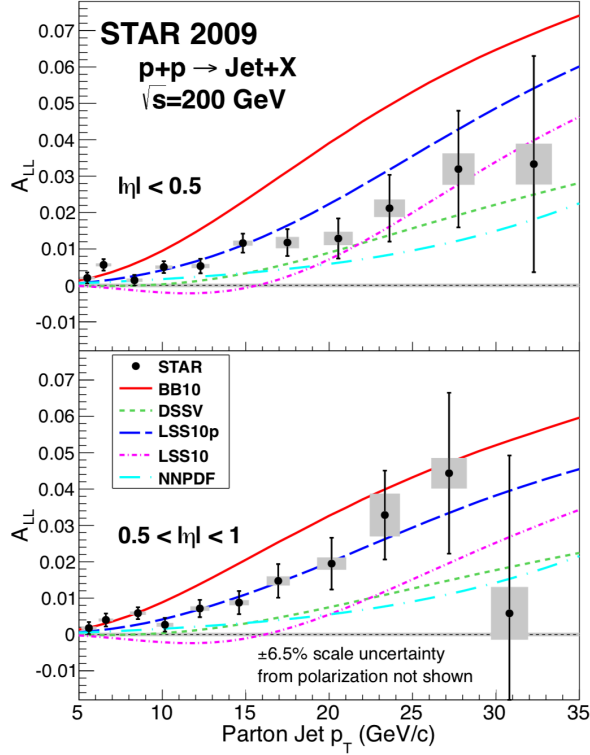


Figure 1.5: **2009 Inclusive Jet  $A_{LL}$**  - The 2009 STAR inclusive jet  $A_{LL}$  at  $\sqrt{s} = 200$  GeV for two different pseudorapidity regions.

The global analysis from the DSSV group (which included the RHIC data until 2006) [11] extracted gluon helicity values that were consistent with zero, but it is clear that the data points for the 2009  $A_{LL}$  stay substantially above the DSSV curve, pointing towards a significant non-zero value of  $\Delta G$  in the region of  $x$  sampled by these measurements.

The current knowledge of  $\Delta G$  is summarized in Figure 1.6. The red curve shows the best fit extraction of the truncated integral of  $\Delta G$  from the DSSV 2014 global analysis [5]. This version of the global analysis includes the 2009 inclusive jet data shown in Figure 1.5. Note that the integral is converging toward a value of 0.36, which translates to over 70% of the proton spin! This value however is accompanied by a very large error bar. The light blue curve, which starts to expand rapidly around

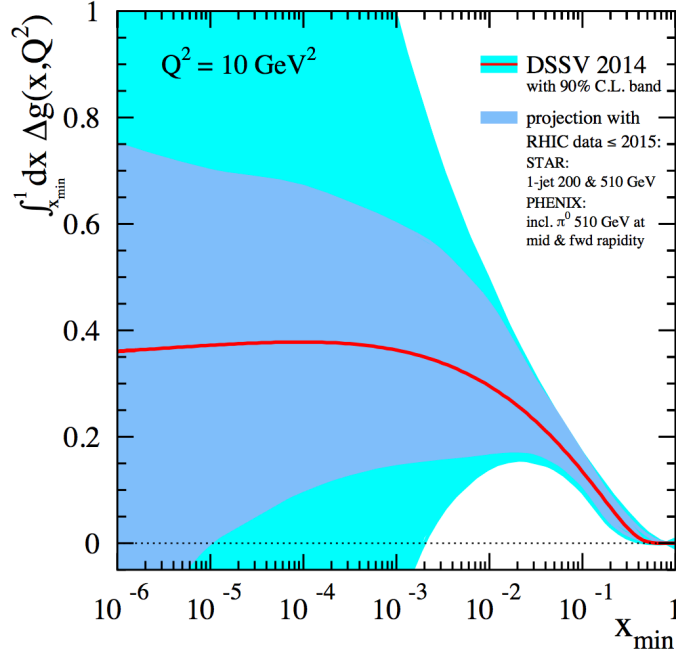


Figure 1.6: **Current knowledge of  $\Delta G$**  - The most recent results from the DSSV 2014 global analysis showing the running integral of the gluon helicity distribution. At any given point of  $x_{\min}$  it shows the truncated integral of  $\Delta g(x)$ .

$x \sim 0.02$  shows the 90% confidence level band for the DSSV14 extraction. The dark blue error band shows the additional constraints that will be placed once the 2015  $\sqrt{s} = 200$  GeV and 2012+2013  $\sqrt{s} = 510$  GeV inclusive jet and pion data are included in the fits. The reduction of the error band at lower  $x$  is driven by the addition of the 510 GeV data. The relationship between the momentum fraction of the parent parton and the  $p_T$  and  $\eta$  of the reconstructed jet is  $x \sim \frac{2p_T}{\sqrt{s}} e^{\pm\eta}$ . As a result the average  $x$  for a given jet  $p_T$  is pushed lower as the  $\sqrt{s}$  is pushed higher.

The inclusive jet  $A_{LL}$  preliminary results from STAR at 510 GeV are shown in Figure 1.7 [12], a comparison to the 2009 200 GeV results as a function of the jet  $x_T$  ( $= \frac{2p_T}{\sqrt{s}}$ ) is shown as well. At a given  $x_T$ , there is a very similar fraction of qq, qg, and gg scattering and very similar  $x$  ranges for each of the partons (Figure 1.4), so the asymmetries are expected to be similar for 200 and 510 GeV. The solid and dotted lines are the theory curves for different PDF scenarios. Comparing the results, it can

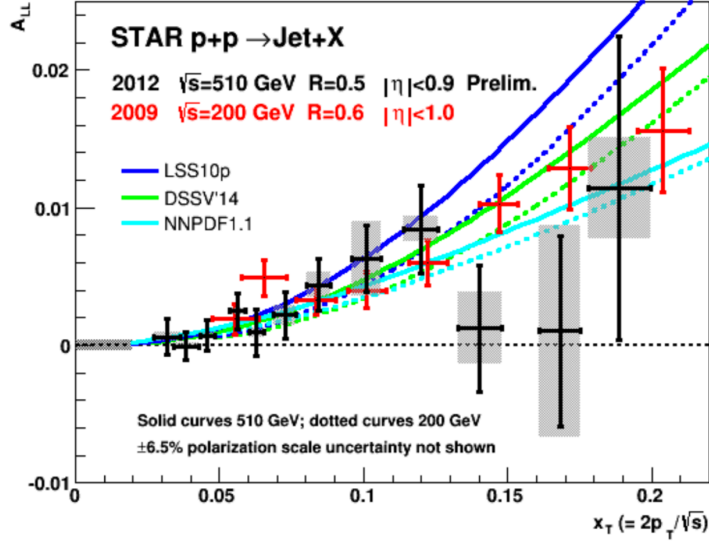


Figure 1.7: **2012 Inclusive Jet  $A_{LL}$  Preliminary** - The 2012 STAR inclusive jet  $A_{LL}$  Preliminary results at  $\sqrt{s} = 510$  GeV compared to the 2009 200 GeV results as a function of the jet  $x_T$ .

be seen that there is very good agreement between the two center of mass regimes in the region of overlap. The  $\sqrt{s} = 510$  GeV data push down to lower  $x$  compared to the 200 GeV data, where  $x_T$  scales with  $x$ .

### 1.3.1 Dijet $A_{LL}$ at 510 GeV

Inclusive jet measurements take into account all of the final state jets in a given event. These measurements also integrate over a large region in the  $x$  of the initial state partons for a given transverse momentum of the final state. To understand more the dependence of  $\Delta g(x)$  on  $x$ , it is necessary to measure the  $A_{LL}$  of correlation observables such as dijets because it tightly constrains the kinematics of the colliding partons. At leading order, the  $x_1$  and  $x_2$  of the partons involved in hard scattering can be defined by the transverse momenta ( $p_{T_3}$  and  $p_{T_4}$ ) and pseudorapidities ( $\eta_3$  and

$\eta_4$ ) of the reconstructed dijet pair, as shown by equations 1.6 and 1.7.

$$x_1 = \frac{1}{\sqrt{s}}(p_{T_3}e^{\eta_3} + p_{T_4}e^{\eta_4}) \quad (1.6)$$

$$x_2 = \frac{1}{\sqrt{s}}(p_{T_3}e^{-\eta_3} + p_{T_4}e^{-\eta_4}) \quad (1.7)$$

Figure 1.8 shows the  $x_1$  (red) and  $x_2$  (blue) distributions from the 2009 dijet analysis at 200 GeV [13] for the invariant mass range of 19-23 GeV. It also shows the momentum fraction distribution ( $x$ ) from the inclusive jet analysis (shown in gray) at 200 GeV scaled down by a factor of 20, for a jet  $p_T$  range of 8.4-11.7 GeV. It is clear that in the case of an inclusive jet analysis, the accessible  $x$  range is very broad, while accessing dijets constrains the initial partonic kinematics for both the initial partons.

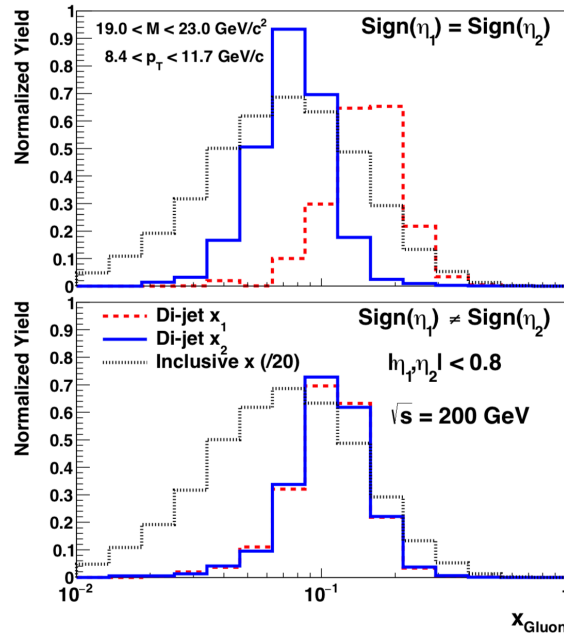


Figure 1.8:  $x$  distributions from dijets and inclusive jets - Momentum fraction distributions of the initial colliding partons from the 2009 dijet analysis at 200 GeV. The broad  $x$  distribution from the inclusive jet data is also shown.

Figure 1.9 shows the first published  $A_{LL}$  for mid-rapidity dijets in  $\sqrt{s} = 200$  GeV proton-proton collisions. The  $A_{LL}$  values are measured as a function of the dijet invariant mass, in two different pseudorapidity ranges. The results are well above the theoretical predictions at low invariant masses, which suggests higher gluon polarizations at lower x values.

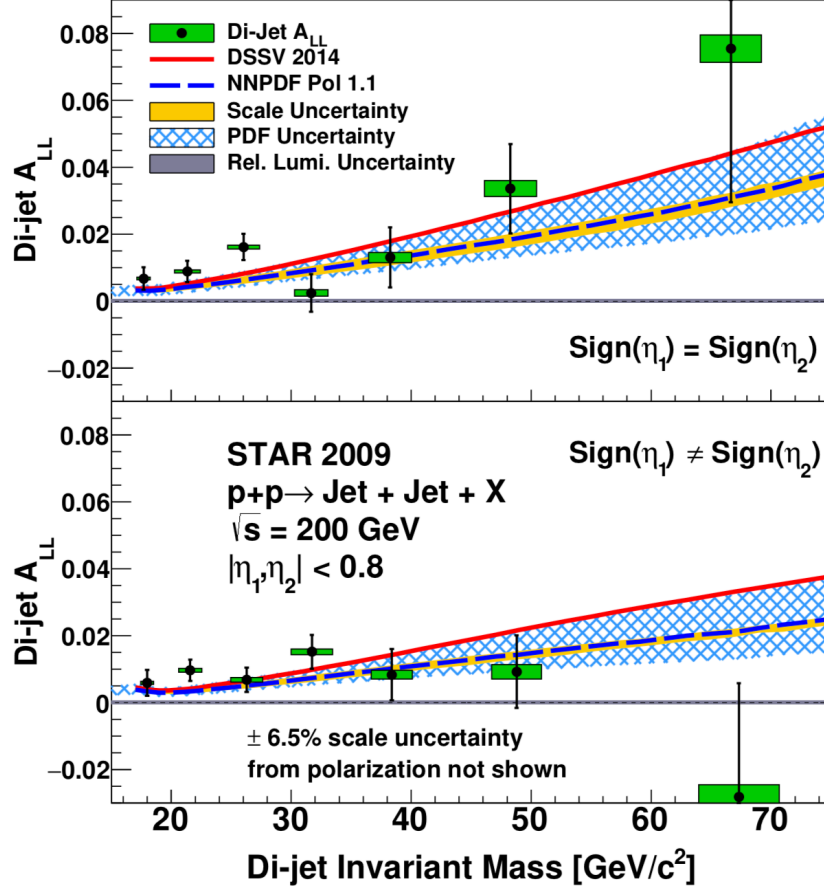


Figure 1.9: **STAR 2009 Dijet  $A_{LL}$  results** - The 2009 Dijet  $A_{LL}$  results from STAR in two different detector topologies, compared with the predictions from various global analyses.

This thesis presents the first measurement of dijet  $A_{LL}$  at  $\sqrt{s} = 510$  GeV. These measurements will provide additional insight into the gluon polarization distributions at lower momentum fractions than the 200 GeV results. Analysing dijets also gives access to the initial state partonic kinematics. In order to maximize the range of achievable momentum fractions, for this analysis, four detector topologies were looked



at, constructed using three different  $\eta$  regions of the detector. Analysing the data topology-separated, helps extract the initial state partonic kinematics to much lower values of momentum fractions, and separates the regions accessing different ranges of  $x$  and  $\cos\theta^*$ .

## Chapter 2 RHIC and The STAR Detector

The Relativistic Heavy Ion Collider (RHIC), located at BNL in Upton NY, is the world's first and only polarized proton collider. The proton collisions used for this analysis were detected by the Solenoidal Tracker at RHIC (STAR). This chapter will discuss the major components of the RHIC accelerator complex and the relevant STAR detector subsystems.

### 2.1 The Relativistic Heavy Ion Collider

RHIC consists of two 3834 m long rings which carry particles in opposite directions and can collide them at center of mass energies between 50 and 510 GeV. Looking down on the RHIC ring from above, the blue beam travels clockwise and the yellow beam travels counterclockwise. Figure 2.1 shows a layout of the RHIC accelerator complex. There are six interaction points (IP) along the ring where the beams of particles collide, located at 12, 2, 4, 6, 8, and 10 o'clock. At present, only STAR and PHENIX (IP 6 and 8, respectively) are active.

#### 2.1.1 Protons in RHIC

Polarized hydrogen beams are produced at the Optically Pumped Polarized Ion Source (OPPIS) [14], where 300  $\mu s$  pulses of a 0.5 mA current produces 35 keV transversely polarized  $H^-$  ions with  $\sim 85\%$  polarization. These are then accelerated by a Radio Frequency Quadrupole magnet and 200 MHz linear accelerator to 200 MeV. Then the electrons are stripped off and the polarized protons are injected into the Booster to be accelerated up to 2.5 GeV, before being injected into the Alternating Gradient Synchrotron where they are accelerated up to 24 GeV. They are then ready to be transferred to the RHIC rings. There are 360 radio frequency (RF)

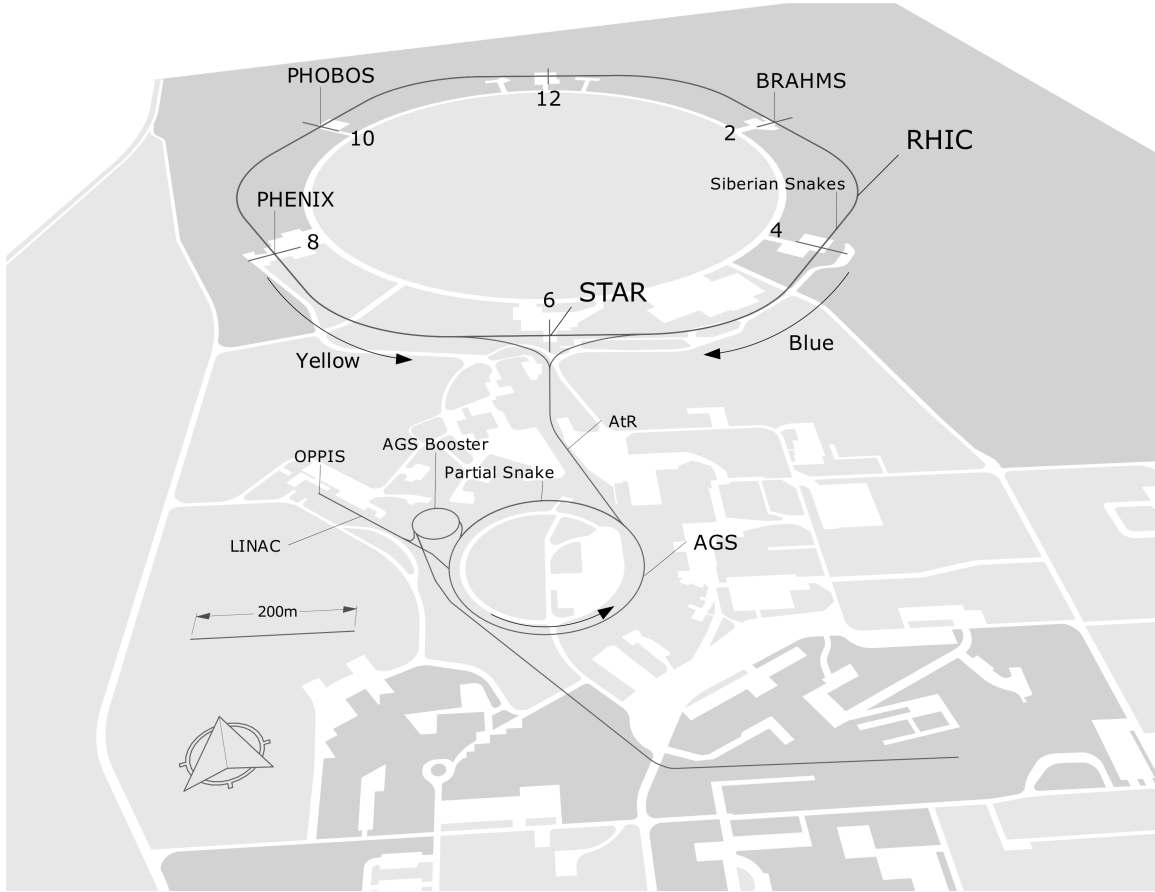


Figure 2.1: **RHIC Complex Layout** - The layout of the RHIC accelerator complex.

cavities (or buckets) in the RHIC ring which can be filled with bunches of polarized protons. During a run, only 120 of these buckets are filled with bunches, with two empty buckets between each bunch. In the 2012 run, 9 of these 120 bunches were left empty in each beam. These were called abort gaps. After injection into the RHIC rings, the beam can be accelerated, or ramped, up to center of mass energies ranging from 62 - 510 GeV. Once the beams are at full energy they are steered into collisions. Depending on the luminosity lifetime, the beams are kept in collision mode for 6-8 hours. A single iteration of this process is referred to as a "store" or "fill".

In each beam, a specific spin configuration is assigned to each beam bucket. This configuration, which repeats every eight bunches, denotes the direction of the polarization of the protons in each bunch. For 2012, there were four such configurations

named  $P1 - P4$ . The configurations have the following patterns:

$$P1 = + - + - - + - +$$

$$P2 = - + - + + - + -$$

$$P3 = + + - - + + - -$$

$$P4 = - - + + - - + +$$

When one beam was set to pattern P1 or P2, the other beam was set to P3 or P4 and vice versa. None of the bunches are identical - there are variations in shape and average polarization values. Therefore, changing the spin configuration fill-by-fill helps in randomizing these bunch characteristics among different spin states and will reduce the systematic effects that could result from sampling one spin configuration more than another.

When injected, the beams are transversely polarized. Spin rotator magnets located before and after the interaction regions are used to orient the proton spins longitudinally. The protons are highly polarized when they are produced, but there are depolarization resonances caused by imperfections in the bending and focusing magnets that will reduce the polarization of the beam [15]. Siberian snakes [16] are used to counteract these depolarizing effects and help maintain the relatively high polarization of the beam. They operate by flipping the spins of the protons in a given bunch by 180 degrees and thereby canceling any spin perturbations.

The polarization of the beams are measured using a Hydrogen Jet Polarimeter [17] and a pCarbon Coulomb Nuclear Interference (CNI) polarimeter [18] which provide absolute and relative polarization measurements respectively. The polarization time dependence can then be used to weight each event by the correct beam polarization. The pCarbon measurements are made several times a fill and are used to determine the time dependence [19].

## 2.2 The STAR Detector

The Solenoidal Tracker at RHIC (STAR) [20] is a multi-purpose, large acceptance detector located at the 6 o'clock position on the RHIC ring. A schematic of the cross section of the STAR detector is shown in Figure 2.2, which denotes the overall size, coverage and the major sub-detectors. The  $z$ -axis along the beam line, with  $z = 0$  defined as the center of the interaction region. The STAR coordinate system follows a right handed notation with the  $+z$  axis pointing in the direction of the blue beam and  $+y$  pointing vertically upward. The geometric center of the detector is defined as  $x,y,z = 0,0,0$ . The relevant sub-detectors for this analysis are explained below.

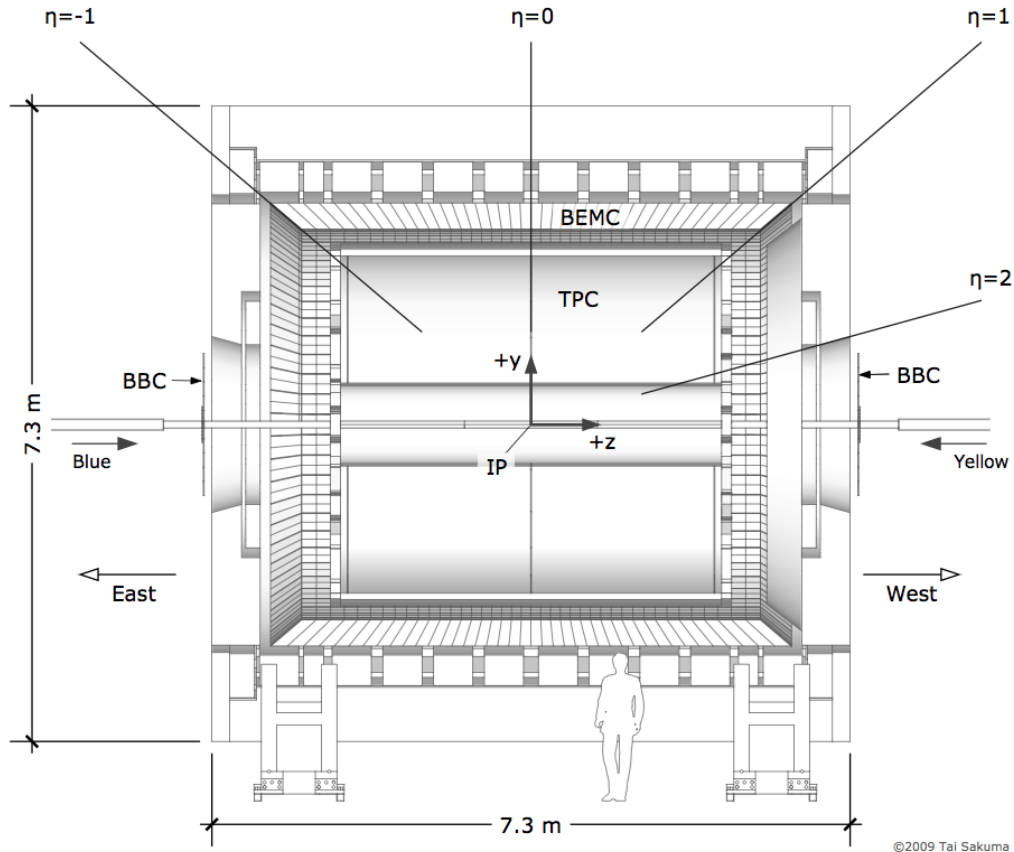


Figure 2.2: **STAR Detector** - The schematic of the STAR detector. [21]

The beam line is encapsulated in azimuth by the Time Projection Chamber (TPC) which reconstructs the momenta of the charged particles. The TPC can reconstruct

charge sign separated track momenta from 100 MeV to over 40 GeV. It has a diameter of 4 meters and total length 4.2 meters, and covers the range  $|\eta| < 1.3$  and  $\Delta\phi = 2\pi$ . The TPC is filled with mixture of 90% argon and 10% methane gas, held at 2 mbar above atmospheric pressure [22]. Charged particles moving through the gas inside the TPC leave a trail of ionized electrons, which then drift along the z-direction, towards the end of the TPC due to the constant electric field. Figure 2.3 shows a schematic of the TPC interior, where the central membrane is at  $z = 0$  and it is a cathode held at 28 kV. The ends of the TPC are anodes held at ground. The gas volume is bound by the inner and outer field cages at radii of 100 cm (inner) and 400 cm (outer). The original charged track can be reconstructed since the anode planes at each end also serve as a readout for the drifting electrons. The drift velocity of the ionized electrons in the TPC is measured multiple times throughout a fill. This velocity, combined with the collision start time permits the reconstruction in time and space of the original ionization. These points are used to reconstruct full tracks as well as the collision vertex.

As charged particles move through the volume, they are immersed in a uniform, 0.5 T magnetic field oriented parallel to the beamline and generated by a solenoidal magnet [24]. The magnetic field is aligned with the electric field to help minimize distortions to the tracks due to electrons spreading in the transverse or longitudinal direction.

The Barrel (BEMC) [25] and Endcap Electromagnetic Calorimeters (EEMC) [26], collectively referred to as the EMCs measure the energy of electromagnetically interacting particles, photons and electrons in the case of STAR. The BEMC and EEMC are positioned outside of the TPC. The BEMC provides  $-1 < \eta < 1$  coverage, and the same  $\Delta\phi = 2\pi$  coverage as the TPC. There are 4800 total calorimeter towers in the BEMC, each covering an area  $\Delta\eta \times \Delta\phi = 0.05 \times 0.05$ . These towers are grouped into 120 modules, with each module composed of a lead and scintillator stack. The

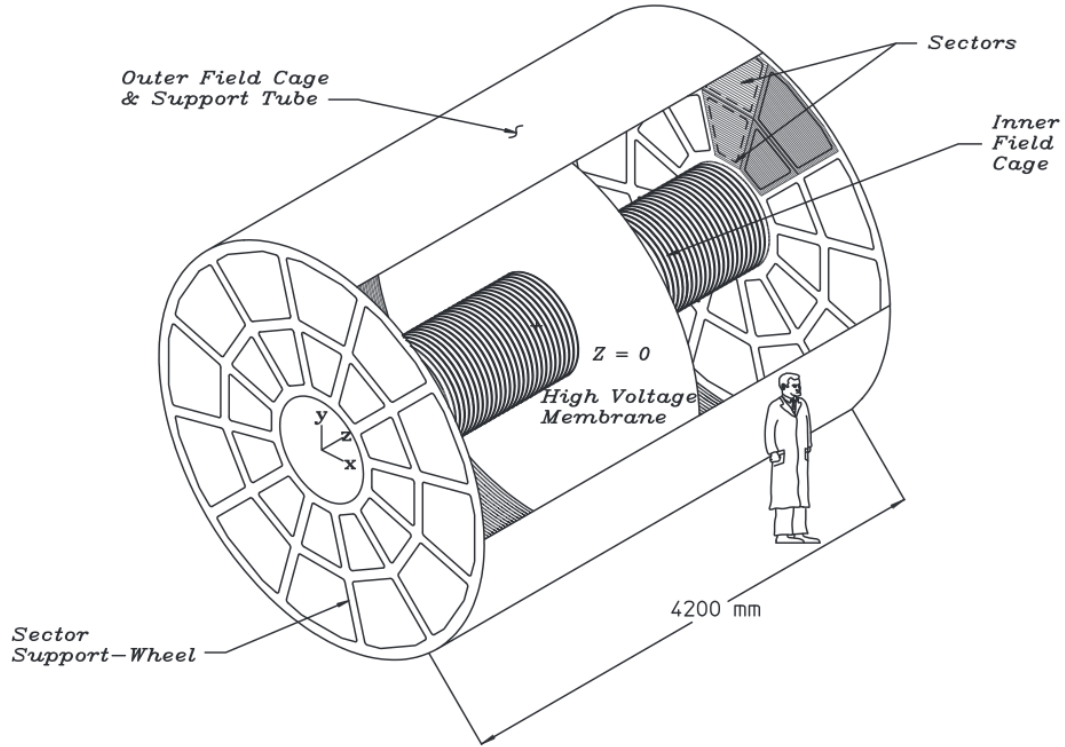


Figure 2.3: **Time Projection Chamber** - A schematic of the TPC. [23].

scintillator layers in each module are constructed as a "megatile", each containing 40 optically separated tiles. The optically separated tiles define the different towers in each megatile. The modules consist of 20 layers of 5 mm thick lead plates, alternating with 21 scintillating layers, for a total of about 20 radiation lengths at  $\eta = 0$ . The first two scintillating layers are 6 mm thick, while the remaining layers are 5 mm each. The light output from the first two scintillator layers is summed together to form a pre-shower layer. The light output from all 21 layers is also summed to provide the full tower readout. The tower configuration is sufficient to stop and contain a 60 GeV electromagnetic shower. For more specific analyses involving high resolution of photons, there is also a shower maximum detector (SMD) located at 5 radiation lengths at  $\eta = 0$ .

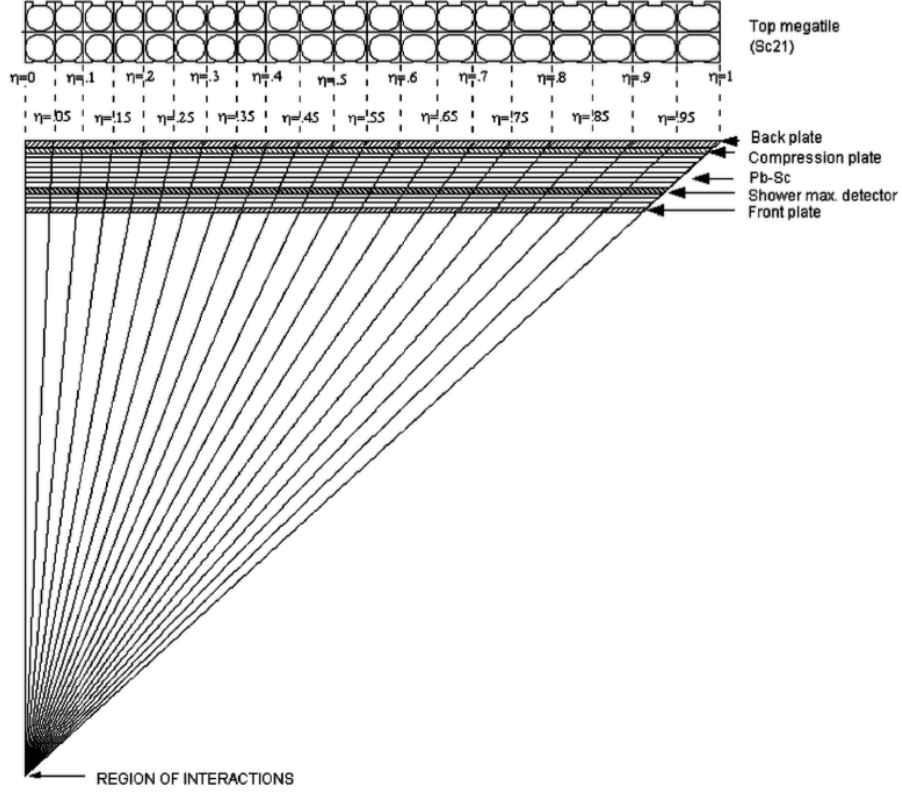


Figure 2.4: **BEMC Tower Layout** - Layout of the BEMC towers including the  $\eta$  coverage of each tower as well as how all towers project back to the interaction region.

The endcap electromagnetic calorimeter (EEMC) is installed at the west end of the STAR detector. It covers an  $\eta$  range of  $1.086 < \eta < 2$ . Just as the BEMC, the EEMC also uses a lead and scintillator stack. The scintillating layers are made into megatiles, containing optically separated tiles. These define the towers that project back towards the interaction region. The EEMC towers are also about 20 radiation lengths deep, similar to the BEMC. The EEMC also contains thick preshower layers as well as a shower maximum detector located in each tower at  $\sim 5$  radiation lengths. Post-shower scintillator layers are also added to the EEMC to differentiate between electrons and charged hadrons.

In addition to these, various detectors are used for providing the local polarimetry and relative luminosity, such as the Beam Beam Counter (BBC), Vertex Position Detector (VPD) and Zero Degree Calorimeter (ZDC).



The BBC [27] is mounted around the beam line outside of the STAR magnet at the east and west side of the collision center about 374 cm from the center. The BBC consists of two arrays of scintillators, each having 18 hexagonal tiles (Figure 2.5). There are 12 tiles in the outer annulus, they are called large tiles and 6 in the inner annulus, called small tiles. The small tiles have a coverage of  $3.4 < \eta < 5.0$  and  $0 < \phi < 2\pi$ , the signals from the small tiles are fed into 16 photomultiplier tubes (PMT). The outputs from these PMTs are then transferred to the STAR trigger system. The signals from the large tiles are not used in this analysis. The BBC is used for triggering on minimum bias events, measuring the local polarimetry, and also to monitor the overall luminosity and relative luminosities in bunch crossings.

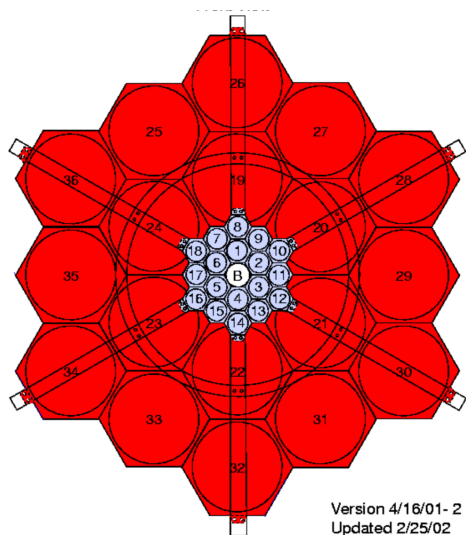


Figure 2.5: **The STAR BBC** - A schematic of the front view of the STAR beam-beam counter.

The VPDs [28] are located one on each side, at  $\sim 5.7$  m from the center of the detector, it has 19 individual detectors on each side. It covers an  $\eta$  range of 4.24 - 5.1. Figure 2.6 shows the individual detectors in one of the VPDs, it consists of a 6.4 mm

lead absorber (about 1.13 radiation lengths thick), a 10 mm scintillator and a PMT attached to the scintillator. Similar to the BBC, the VPD is also used to trigger on minimum bias events and to measure the relative luminosity.

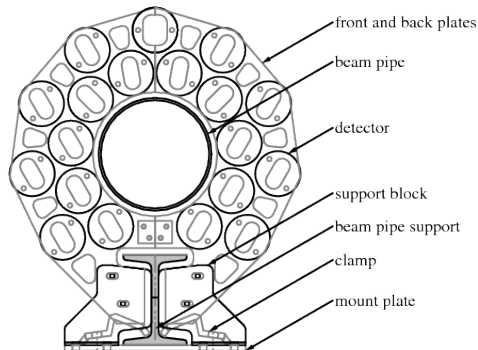


Figure 2.6: **The STAR VPD** - A schematic of the front view of the STAR vertex position detector.

The ZDC detectors [29] have three modules each 10 cm in width and 13.6 cm in length, located at the east and west sides of the center. Each module has alternating quartz and tungsten layers, the tungsten plate is 0.5 cm thick and it corresponds to 50 radiation lengths. These detectors are designed to detect evaporation neutrons from heavy ion collisions really close to the beamline. When the neutrons hit the detector, the charged particles in the showers produce Cherenkov light, which is then transported to a single PMT. Similar to the BBC and VPD, the ZDC detectors are also used to trigger on minimum bias events, monitor the overall luminosity and measure the relative luminosity in the bunch crossings.

## Chapter 3 Data Selection

### 3.1 Dataset

For the 2012 RHIC run, the STAR detector recorded  $\sim 50 \text{ pb}^{-1}$  of data from longitudinally polarized proton collisions at  $\sqrt{s}=510 \text{ GeV}$ . The data taking extended from March 15, 2012 to April 18, 2012. Data is collected as a set of "runs", and each run ranges from a few minutes to an hour in length. A total of 734 runs were recorded with the major detectors BEMC, EEMC and TPC in good status.

### 3.2 Triggers

Since it is not feasible to record all of the data from the collisions at STAR, events are recorded online only if they satisfy the requirements of at least one of the active "triggers" during the run. The BEMC and EEMC sub-detectors constitute the triggering system for high  $p_T$  particle and jet event studies, because they can read out data very fast and keep up with the collision rate ( $\sim 9.35 \text{ MHz}$ ) at RHIC. Every  $\sim 109 \text{ ns}$  the detector is read out and that data is funneled through the trigger system, which then decides whether the event satisfies the trigger conditions. If the event is a good triggered event, data from the tracking detectors are also stored.

The triggers used in this analysis are called the jet patch triggers. There are six patches on the east and west ends of the barrel, and 6 patches overlapping the other jet patches across  $\eta = 0$ . The EEMC also has 6 jet patches which cover  $1 \times 1 \eta - \phi$  regions. For each event, the ADC values from the BEMC and EEMC front end electronics are passed into a Data Storage and Manipulation (DSM) tree to apply the thresholds [30]. The approximate conversion from the DSM ADC thresholds to the

energy thresholds (in GeV) is done using Eq. 3.1.

$$E_T = 0.236 \times (ADC - 5) \tag{3.1}$$

Three jet patch triggers - JP0, JP1 and JP2 are used in this analysis, and Table 3.1 compares each of these triggers with the DSM ADC threshold and the corresponding energy threshold.

Table 3.1: **Jet Patch Trigger Thresholds**

Name	DSM ADC Threshold	$E_T$
JP0	28	5.4 GeV
JP1	36	7.3 GeV
JP2	66	14.4 GeV

### 3.3 Event-Level Quality Analysis

All recorded runs are subjected to a quality control analysis designed to weed out events recorded in runs with detector and/or trigger problems. In the data quality analysis, various reconstructed observables such as the average BEMC  $E_T$ , average EEMC  $E_T$  and the average track  $p_T$  are plotted as a function of run number. Runs with significant deviations from the average are subject to further investigation and possible removal from the final analysis.

As an example, Figure 3.1 shows a plot of the average BEMC  $E_T$  as a function of the run index for various triggers - JP0, JP1, JP2, L2JetHigh and VPDMB. From this plot it is clear that there are several runs that need to be investigated further because they deviate from the general trend. This is done using the shift log and the online trigger plots produced real-time during running. The decision to keep or remove the outliers was based on these investigations.

This procedure is repeated for the average EEMC  $E_T$  and the track  $p_T$  for all triggers, until all of the suspicious runs have been investigated. In case of clear

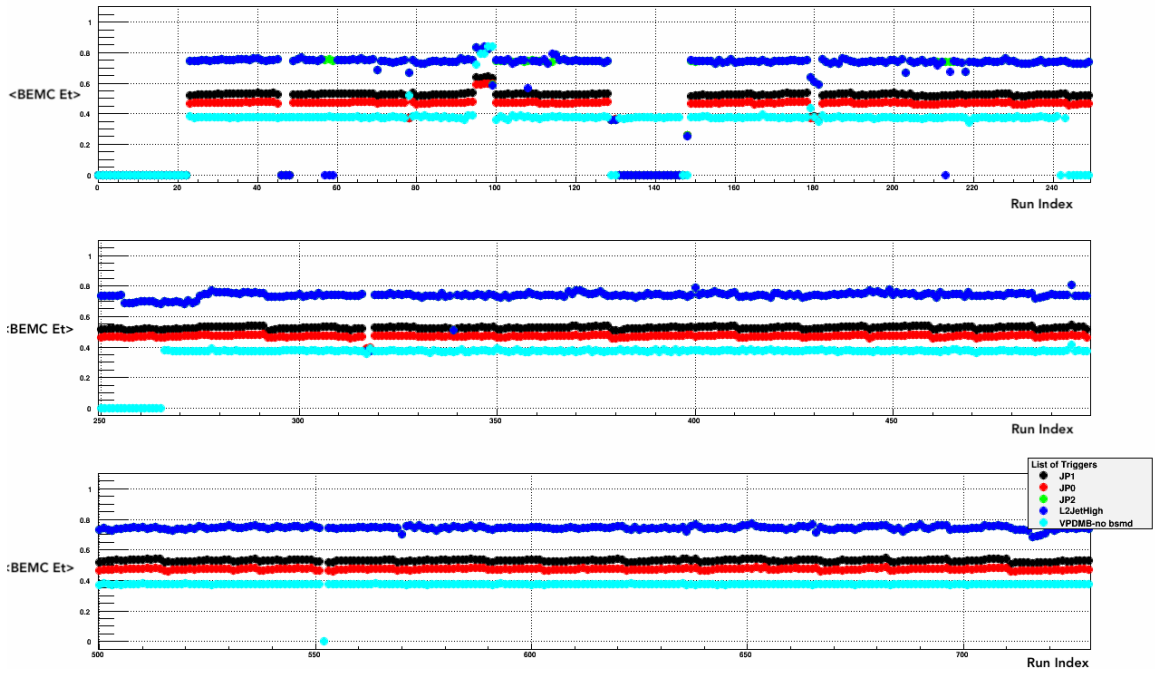


Figure 3.1: Average BEMC  $E_T$  vs. Run Index - The average BEMC  $E_T$  before QA.

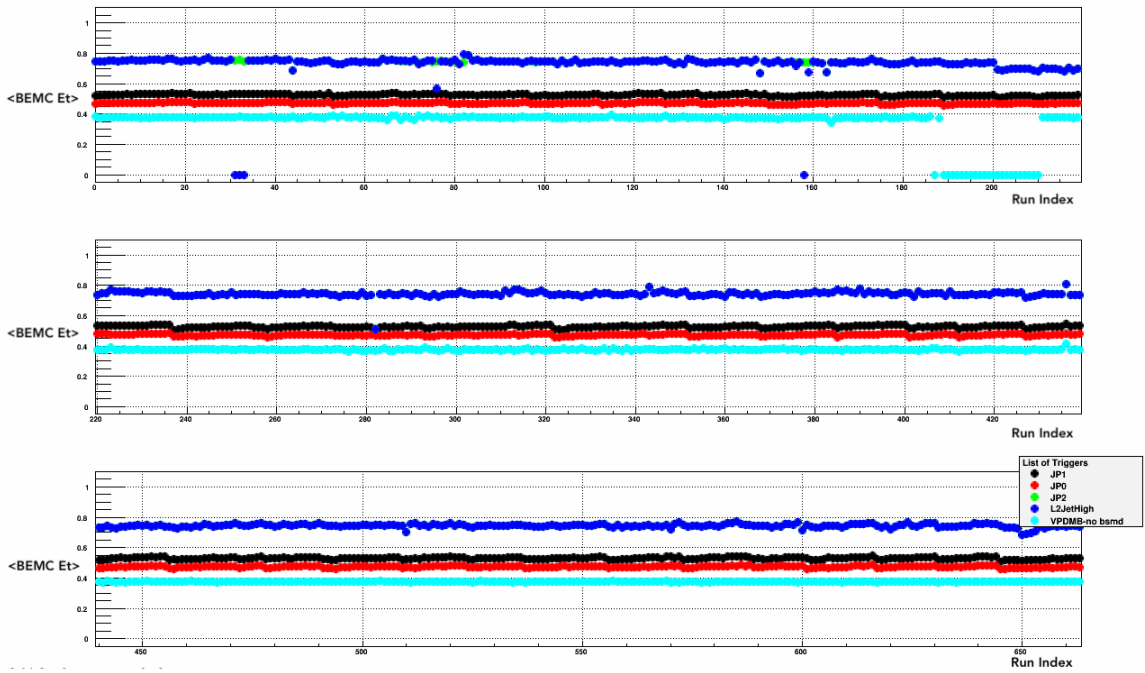


Figure 3.2: Average BEMC  $E_T$  vs. Run Index - The average BEMC  $E_T$  after removing the outliers.

reasons, the outlier runs are removed, but in case of absence of a sufficient reason, these runs are kept for the time being. After studying these three major observables, a total of 70 runs were removed. The major issues concerning these runs included triggers and pedestals not being correctly set up and statistics being extremely low in the first few runs, configuration issues (from the online Level-0 monitoring plots), bad pedestals (from the online Level-2 monitoring plots) and some problems in the crates. Figure 3.2 shows the plot after removing the suspicious runs.

Figures 3.3 and 3.4, and Figures 3.5 and 3.6 show the average EEMC  $E_T$  and the average track  $p_T$  before and after the quality analysis. The reasons for removing the outliers were (in most cases) the same as that of the average BEMC  $E_T$ . After the quality analysis at the event-level, it is ensured that all of the detector components are responding as expected and delivering consistent results throughout the 2012 longitudinal running period.

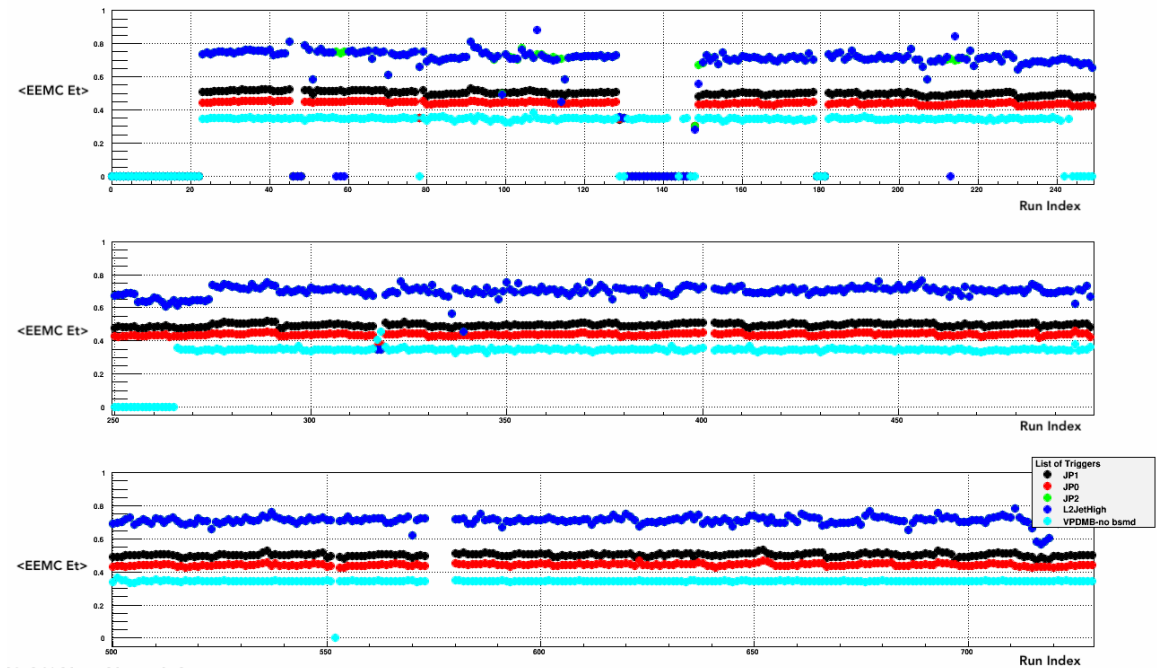


Figure 3.3: Average EEMC  $E_T$  vs. Run Index - The average EEMC  $E_T$  before QA.

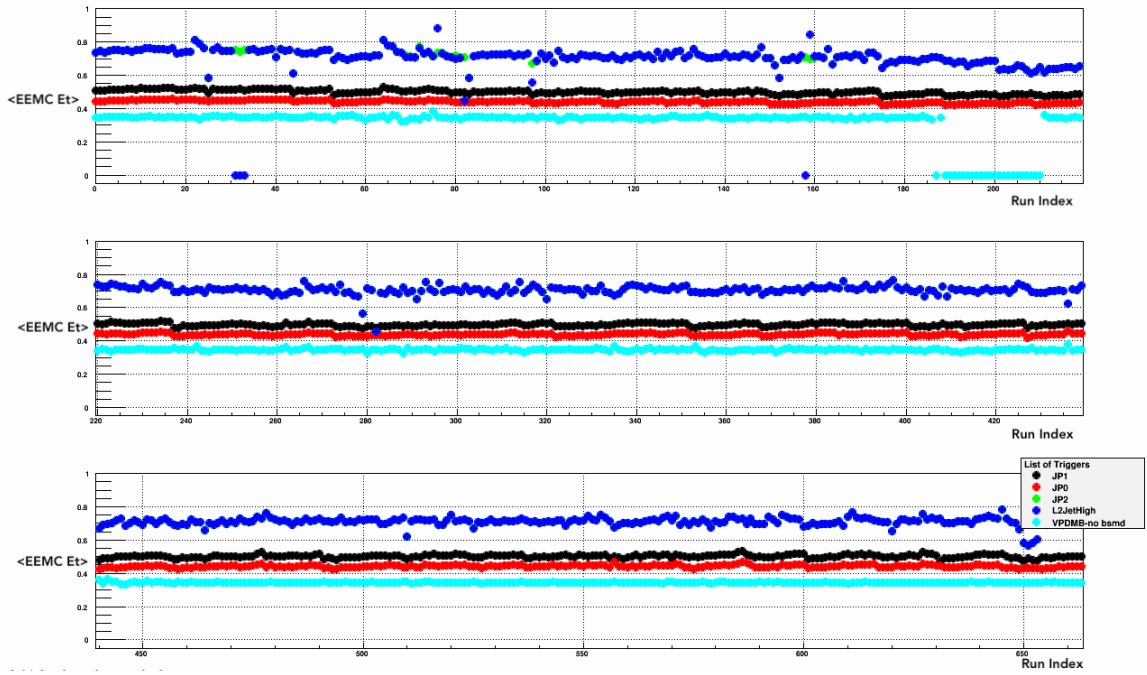


Figure 3.4: Average EEMC  $E_T$  vs. Run Index - The average EEMC  $E_T$  after removing the outliers.

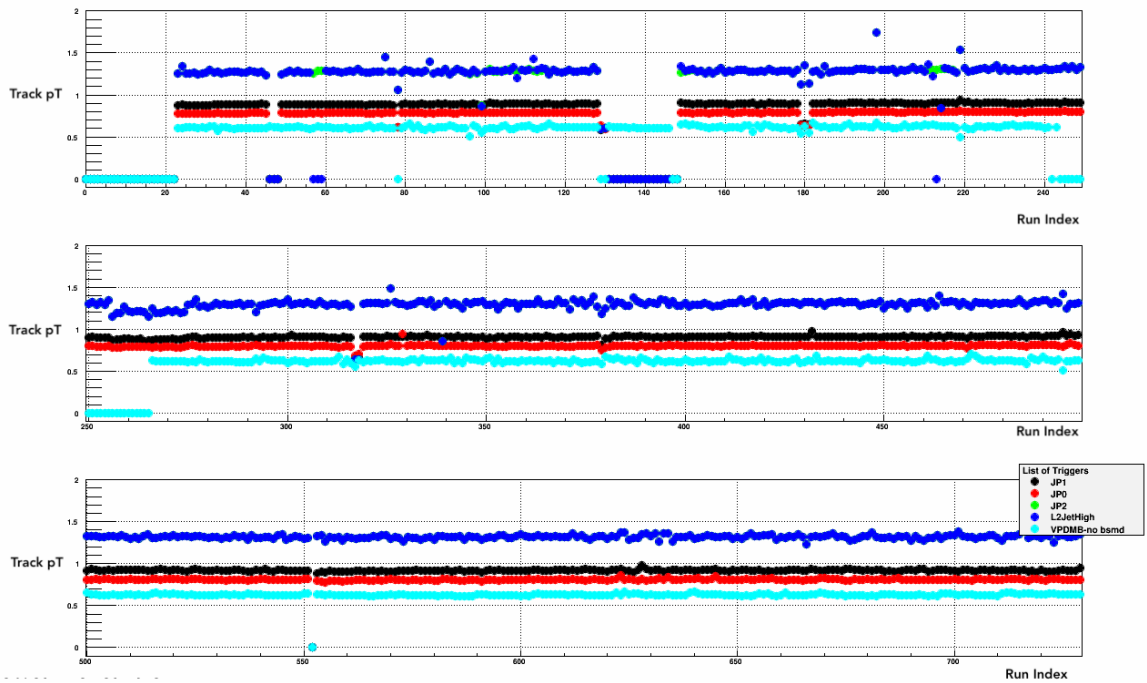


Figure 3.5: Average track  $p_T$  vs. Run Index - The average track  $p_T$  before QA.

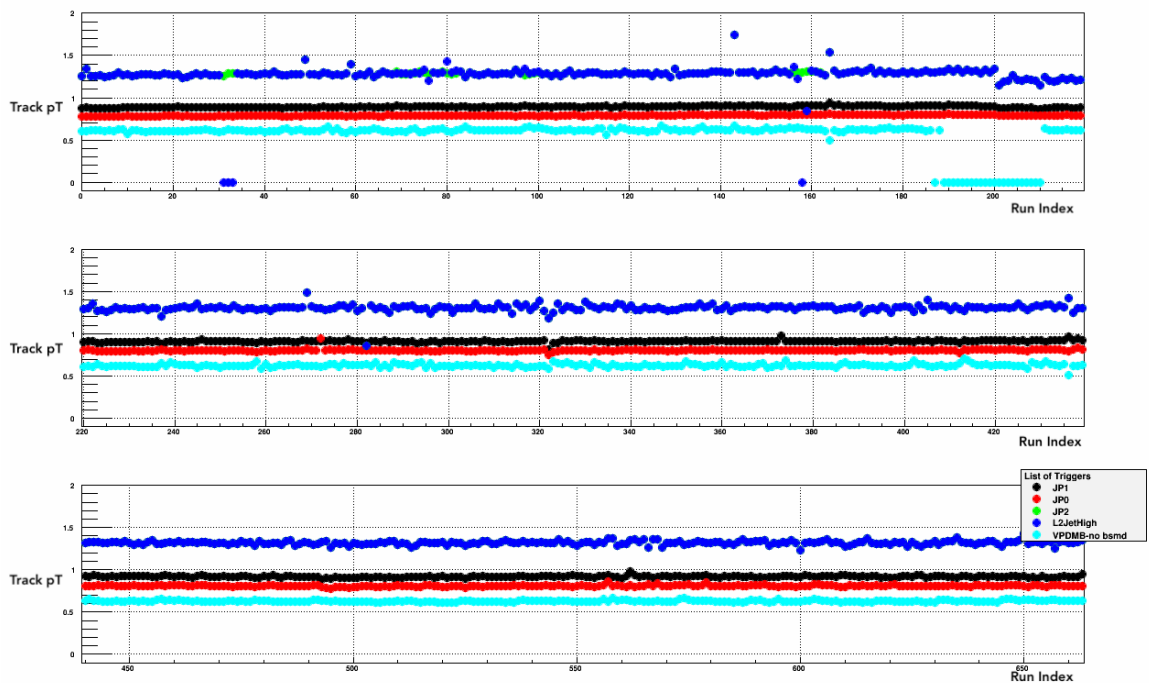


Figure 3.6: Average track  $p_T$  vs. Run Index - The average track  $p_T$  after removing the outliers.



## Chapter 4 Jet and Dijet Reconstruction

### 4.1 Jets

In high energy proton-proton collisions, the final state usually consists of showers of particles produced from the hadronization of quarks and gluons, known as jets. By measuring the 4-momentum of the jet, properties of the original parton that produced them can be studied. Jets can be analyzed at different levels - at the detector level in data and at the parton, particle and detector level in simulation. The detector level jets are reconstructed from TPC tracks and the energy deposits in the EMC towers. Particle level jets are formed from stable final state particles produced during hadronization, and parton level jets from the scattered partons produced in the hard collision as well as those from final and initial state radiation. More details about studying the jets in simulation can be found in Chapter 5.

#### 4.1.1 Jet Reconstruction

Jet algorithms belong to one of two categories - sequential clustering algorithms and cone algorithms. Sequential clustering algorithms identify the pair of particles that are closest in a specific distance scale, and recombine them depending on the transverse momentum  $p_T$  and then repeat the procedure until specific stopping criteria are met. Cone algorithms aggregate particles within angular regions, accumulating them such that the sum of the four-momenta of the particles contained in a given cone coincides with the cone axis. Before 2009, the STAR jet analyses used the midpoint cone algorithm, and for all later runs the FastJet *Anti* -  $k_T$  algorithm [31].

### 4.1.2 *Anti* – $k_T$ Algorithm

The *Anti* –  $k_T$  algorithm is a sequential clustering algorithm that combines particles depending on their transverse momentum and the distance between the particles and the beam line. Using the cone radius ( $R$ ), inverse transverse momentum ( $k_T$ ), rapidity ( $y$ ) and azimuthal angle ( $\phi$ ), two distances are defined: the distance between any two entities (tracks, towers),  $d_{ij}$  (Eq. 4.1), and the distance between an entity and the beam,  $d_{iB}$  (Eq. 4.2).

$$d_{ij} = \min \left( \frac{1}{k_{Ti}^2}, \frac{1}{k_{Tj}^2} \right) \times \frac{\Delta_{ij}^2}{R^2} \quad (4.1)$$

$$d_{iB} = \frac{1}{k_{Ti}^2} \quad (4.2)$$

$$\Delta_{ij}^2 = (y_i - y_j)^2 + (\phi_i - \phi_j)^2 \quad (4.3)$$

If the minimum of  $d_{ij}$  and  $d_{iB}$  is  $d_{ij}$ , the entities  $i$  and  $j$  are combined by adding the 4-vectors associated with them, and the iteration continues. If  $d_{iB}$  is the minimum, then  $i$  is called a jet and all the particles in that jet are removed from the list of particles. The distances are recalculated and this process is repeated until no entities are left. The *Anti* –  $k_T$  algorithm behaves like an idealized cone algorithm, and is less susceptible to effects from pile-up and underlying event contributions. Since this algorithm relies on distances between entities and not on a seed particle like in the cone algorithms to define the jets, it is collinear and infrared safe to all orders. Collinear safety means that the algorithm provides the same output jet in an event with collinear splitting of the fragmenting parton. Infrared safety refers to how the jets are reconstructed in the presence of soft radiation. For this analysis, the *Anti* –  $k_T$  algorithm with a radius parameter of  $R=0.5$  cm has been used.

### 4.1.3 Jet-finding Cuts

The jet-finder takes in the charged particle tracks and the energy deposited in towers for the reconstruction of jets, on an event-by-event basis. The vertex where the two protons collide is known as the primary vertex. From the reconstructed primary vertex, the primary tracks are selected. The pile-up proof vertex finder was used in this analysis. After finding all of the possible primary vertices in an event, the highest ranked vertex is selected for the analysis. This is done using the PPV finder, it assigns vertices that could be from pile-up events a negative ranking, and the highest ranked vertex chosen is required to have a positive ranking. Only the tracks that are associated with the highest ranked vertex are used for the analysis. In addition to the *Anti* -  $k_T$  radius parameter, a number of cuts are applied on the tracks and towers during the process of jet reconstruction as well.

The number of TPC hits is required to be greater than 51% of the total possible hits for that track, in order to minimize the chance of the reconstructed tracks being split tracks. A cut on the distance of closest approach (DCA) between the closest TPC hit on the track and the primary reconstructed vertex is applied depending on the track  $p_T$  in order to reduce the background. The DCA must be within 2 cm for track  $p_T < 0.5$  GeV/c and within 1 cm for track  $p_T > 1.5$  GeV/c. For track  $p_T$  values in the intermediate region, the DCA must satisfy a linearly decreasing cut. The last hit in the TPC padrows has to be a maximum of 125 cm from the center to avoid historical issues with the outer pads. In addition to that, tracks were required to have a  $p_T$  greater than 0.2 GeV and  $\eta$  between -2.5 and 2.5.

A series of cuts were applied on the towers as well. The offline status for each tower was required to be set to 1, meaning the tower did not have any issues and was functioning properly. These offline tower status values are calculated from data in real time at the end of each run. In order to make sure that the hits in the towers are true physics hits, and not from the pedestal, the difference between the tower

ADC and pedestal was required to be greater than 4 ADC bins. Finally, the tower  $E_T$  was required to be greater than 0.2 GeV as well. All of the cuts that are applied on the tracks and towers used in jet reconstruction are summarized in Table 4.1. The tracks and towers then serve as input to the jet-finder where the jet reconstruction algorithm is applied. The track momentum and tower energy, which are measured, are converted into four vectors. All of the towers are assumed to have zero rest mass (as if they were decay photons from neutral pions) and all of the tracks are assumed to have the charged pion mass. These discrepancies are corrected out when the invariant mass corrections are done.

Table 4.1: **Track and tower cuts** - Cuts applied to the tracks and towers.

Cut	Value
Track $N_{hits}/N_{possible}$	$> 0.51$
Distance of Closest Approach (DCA) to vertex	Track $p_T$ dependent
Track $p_T$	$0.2 \text{ GeV}/c < p_T < 200 \text{ GeV}/c$
Track $\eta$	$-2.5 < \eta < 2.5$
Radius of last track fit point	$R > 125 \text{ cm}$
Track "flag"	$> 0$
Offline EMC tower status	1
EMC tower $ADC - pedestal$	$> 4 \text{ ADC bins}$
EMC tower $ADC - pedestal$	$> RMS_{pedestal}$
EMC tower $E_T$	$> 0.2 \text{ GeV}$

During jet reconstruction, adding the energy from EMC towers and tracks from TPC may lead to double counting. For electrons and positrons, the entire energy will be included twice, while charged hadrons like charged pions only deposit a MIPs worth of energy in the calorimeters. This effect is mitigated by first "matching" geometrically a TPC track to the EMC tower and then subtracting the  $p_T$  of the track (multiplied by  $c$ ) from the  $E_T$  of the tower.

## 4.2 Dijets

A dijet event is defined as any event with at least two jets. In a dijet event, the dijet pair consists of the two jets with highest  $p_T$ . The four-momentum of the dijet is given by the four-vector sum of the two jets, as in eq 4.4 where  $p_3$  and  $p_4$  are the four-momenta of the individual jets:

$$p_{dijet} = p_3 + p_4 \quad (4.4)$$

The dijet invariant mass ( $M_{inv}$ ) is defined as:

$$M_{inv} = \sqrt{E^2 - \vec{p}^2} \quad (4.5)$$

where  $E$  and  $\vec{p}$  are components of the four-vector  $p_{dijet}$ .

### 4.2.1 Underlying Event Subtraction

During a proton-proton collision, the scattering process which is of most interest is the hard scattering of the partons. However, the final signals measured could also have contributions from other soft scatterings from the same event - two examples for these possible soft scatterings are multiple parton interactions and contributions from the proton remnants. The background generated due to these soft scatterings is known as the underlying event. There are several methods to estimate the underlying event contribution. In this analysis, this contribution is studied on a jet-by-jet basis, and the method used is called the "Off-Axis Cones method". This was developed by Zilong Chang for the 2012 Inclusive Jet analysis at 510 GeV, and was adapted from the perpendicular cones method developed for the ALICE experiment [32].

This method is based on existing evidence that the underlying event is on average isotropic. This allows to estimate the underlying event contributions by looking outside of the jet. In this method, for every reconstructed jet, two off-axis cones are drawn, each of which is centered at the same  $\eta$  as the jet but  $\pm\pi/2$  away in  $\phi$

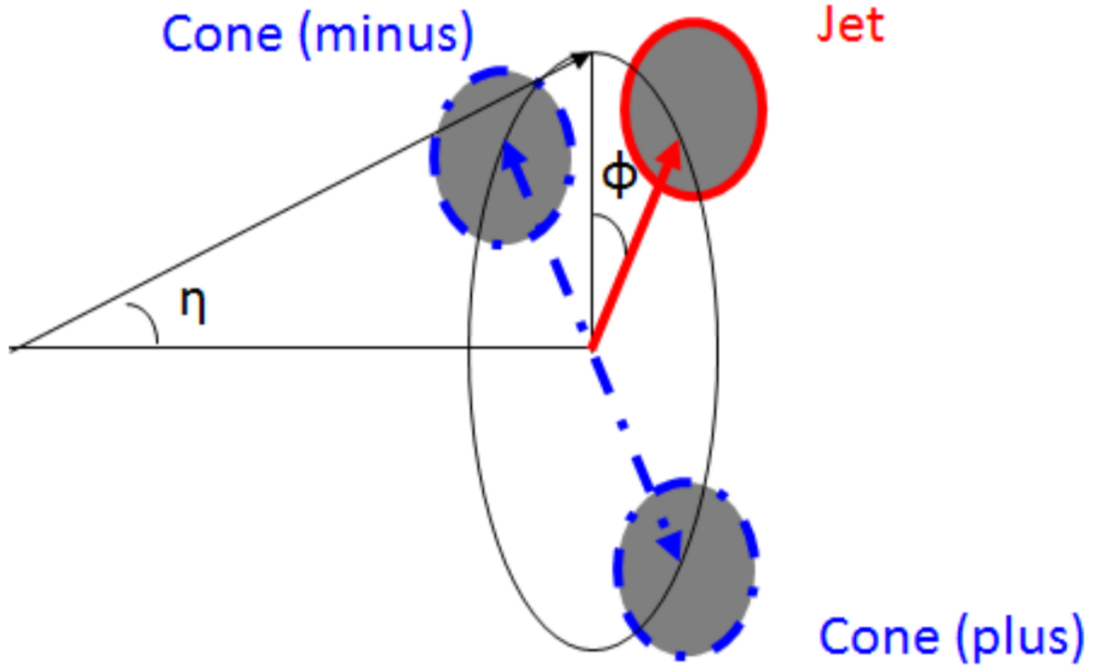


Figure 4.1: **Off-Axis Cones** - The schematic illustration of the two off-axis cones relative to the position of the jet.

from the jet as shown in Figure 4.1. The off-axis cone radius is chosen to be 0.5 cm, same as the radius parameter of the *Anti -  $k_T$*  algorithm used for this analysis. Then all of the tracks and towers inside these two cones are collected. As with jet reconstruction, the tracks are assigned mass of a pion (139 MeV) and the towers are assigned a mass of zero, in order to construct the four-momenta of the tracks and towers in the cones. After adding all of the track and tower four-momenta in each cone (Eq. 4.6), the resultant four-vector from each cone is rotated back in  $\pm\pi/2$  in order to align them back along the direction of the jet. Once this is done, the average underlying event four-vector is calculated from the four-vectors of the two cones (Eq. 4.7). Then, in order to obtain the the final four-momentum of the corrected jet, the underlying event four-momentum is scaled to the area of the jet, and subtracted from the four-momentum of the jet (Eq. 4.8). The jet area is given by the *Anti -  $k_T$*

algorithm, by using the technique of ghost particles [33].

$$p_{UE}^{cone} = \Sigma Track(p_T, \eta, \phi, M_\pi) + \Sigma Tower(p_T, \eta, \phi, 0) \quad (4.6)$$

$$p_{UE} = 1/2(p_{UE}^{cone1} + p_{UE}^{cone2}) \quad (4.7)$$

$$p_{jet}^{UEcorr} = p_{jet} - (p_{UE} * A_{jet}/\pi R^2) \quad (4.8)$$

### 4.2.2 Dijet Cuts

In order to select dijet events for the analysis, various cuts are applied on the event, and on the individual jets in the dijet. The cuts and the order of implementation are listed below:

1. Select events with one or more reconstructed vertices with rank  $> 0$ .
2. Select the highest ranked vertex in the event.
3. Select events with at least two jets.
4. Select the two highest  $p_T$  jets in the event.
5. Subtract the underlying event from both the jets, to obtain the corrected jet four-momenta.
6. Require at least one of the jets to satisfy the geometric trigger matching condition. The geometric trigger matching requires the axis of the jet to point to a jet patch that satisfies either the JP0, JP1 or JP2 trigger conditions. The jet that passes the JP0, JP1 or JP2 geometric trigger is required to have an associated  $p_T$  threshold  $> 6, 8$  and  $15$  GeV.
7. Require  $|Z_{vertex}| < 90$  cm.
8. Ensure that jets in the dijet are back-to-back:  $\cos\Delta\phi > 0.5$ . This limits the inclusion of jets that arise from a hard gluon emission from a parton that participated in the hard scattering interaction.

9. Require that both jets have neutral fraction ( $R_t$ )  $< 0.95$ .
10. Apply asymmetric  $p_T$  cut on the underlying event subtracted jet  $p_T$  ( $p_{T_3} > 8$  GeV and  $p_{T_4} > 6$  GeV.).
11. Require that both jets satisfy  $-0.7 < \eta_{detector} < 0.9$
12. Require that both jets satisfy  $-0.9 < \eta_{physics} < 0.9$
13. Apply  $p_T$  matching cut: Defined by the function in Eq. 4.9 where  $p_T^{track_{max}}$  denotes the  $p_T$  of the track with the highest transverse momentum in the jet. This cut is aimed at removing fake jets that are composed primarily of a single poorly reconstructed track. This cut was tuned in data, and the plots shown below in Figures 4.2 and 4.3 illustrate the events cut off by this cut.

$$p_T^{leading} / p_T^{away-side} < (-0.08 * p_T^{track_{max}}) + 6.0 \quad (4.9)$$

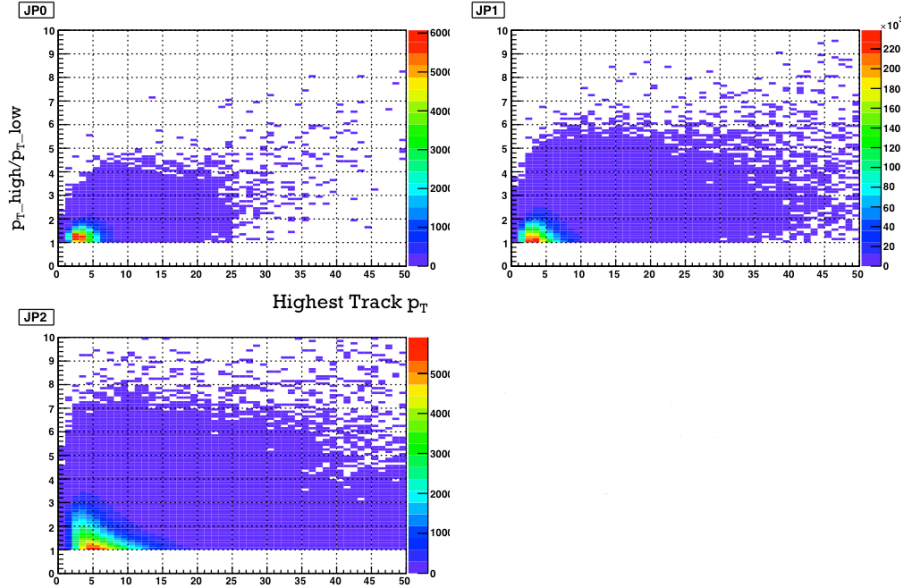


Figure 4.2: **Track  $p_T$  vs jet  $p_T$  ratio - Before cut** - The distribution of  $p_T$  of the track with the highest transverse momentum in the jet to the ratio of the transverse momenta of the two jets, before applying the cut.



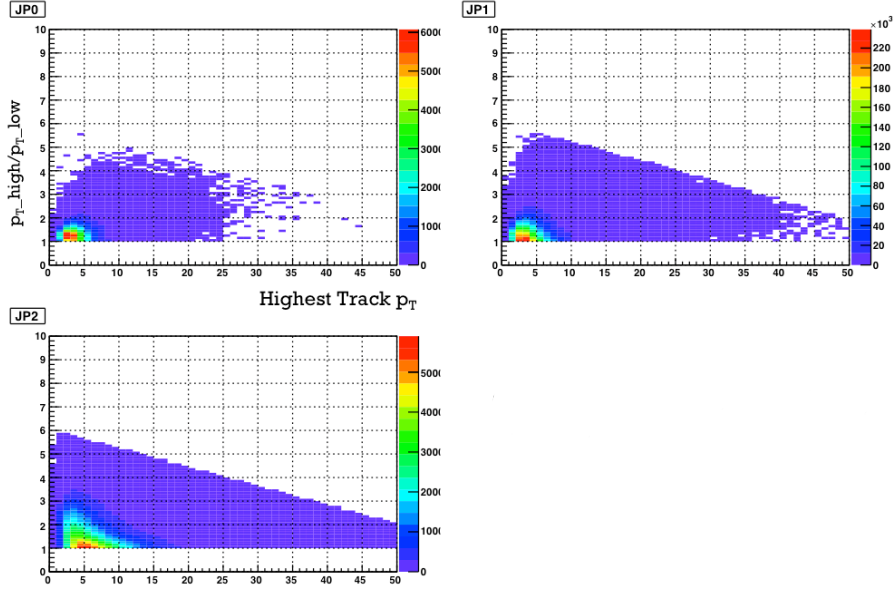


Figure 4.3: **Track  $p_T$  vs jet  $p_T$  ratio - After cut** - The distribution of  $p_T$  of the track with the highest transverse momentum in the jet to the ratio of the transverse momenta of the two jets, after applying the cut.

14. Remove the events if the underlying event correction makes either of the jet  $p_T$  shift down more than two bins.

The triggers used in this analysis are the JP0, JP1 and JP2 triggers. The JP0 and JP1 events were pre-scaled while the JP2 events were not, during data taking. Obtaining a mutually exclusive sample among these triggers will help understand the effects contributed by each individual trigger. The trigger categorization algorithm is explained in detail below.

For each event, the information if a trigger was actually fired ("didfire") can be found in the event record. The didfire flag would be set to one if the trigger was fired, and would be set to zero if it did not. An offline trigger simulator was applied where the trigger decision was simulated by imitating the online trigger system ("shouldfire"). The raw ADC from the BEMC and EEMC towers was used as the input data and the same trigger algorithm was implemented. If a trigger was fired in

the trigger simulator, the shouldfire flag is set to one, and zero otherwise. The main objective of the offline trigger simulator is that it helps select events in the simulation which will be used for the estimation of the systematics. In the analysis of real data, requiring both didfire and shouldfire flags to be one ensures a consistent event selection method between data and simulation. Another advantage of this process is that the online trigger simulator helps tag the events skipped during pre-scaling, and can be used to promote a heavily pre-scaled trigger category in comparison with the others.

The trigger thresholds for JP2, JP1 and JP0 are 14.4 GeV, 7.3 GeV and 5.4 GeV. After giving some room for the track contributions to the jet momentum, extra trigger- $p_T$  cuts are introduced for each of these triggers (15 GeV, 8 GeV and 6 GeV respectively). For each jet, a geometric matching condition is also imposed to make sure that the same jet fires the jet patch. The condition requires that the jet  $\eta$  and  $\phi$  are within the range of  $\pm 0.6$  of the  $\eta$  and  $\phi$  of the jet patch, and that the jet patch sum ADC should be above the specific trigger threshold. In order for a jet to be classified as a JP2 jet, the didfire and shouldfire flags should be one, and the jet should pass the geometric matching condition and the trigger  $p_T$  cut of 15 GeV. For a jet that does not pass these conditions, it is checked if it falls into the JP1 category. If the jet passes the geometric matching condition and the trigger  $p_T$  cut corresponding to JP1, and the didfire and shouldfire flags for JP1 are one, the jet is classified as a JP1 jet. In addition to that, if the jet satisfies the JP1 jet  $p_T$  requirement, the didfire flag for JP0 is one and shouldfire flag for JP1 is one, then the jet is promoted from a JP0 jet to JP1. Once the jet does not satisfy the JP2 and JP1 category requirements, it is classified as a JP0 jet as long as both didfire and shouldfire flags are one, the jet passes the geometric matching cut and the trigger  $p_T$  cut for JP0.

After checking these conditions, both the jets in the dijet are tagged as either JP2, JP1 or JP0. Then, if at least one jet in the dijet pair is tagged as a JP2 jet, the

event is categorized as a JP2 event. If not, and if at least one jet is a JP1 jet, it is categorized as a JP1 event. And finally, if it is neither JP2 nor JP1, and at least one jet falls in the JP0 category, the event is categorized as a JP0 event.

## Chapter 5 Monte Carlo Simulation

Simulated events are used to correct for detector effects and to estimate systematic errors. Events are generated using the PYTHIA Monte Carlo generator [34], and processed through GEANT4 [35] in order to simulate the detector geometry. In an effort to incorporate background and pile-up effects into the simulation, detector responses from zero-bias events taken during the run are embedded into the simulated events and mixed with the GEANT detector responses. The zero-bias events are randomly triggered during the nominal time for a beam crossing to occur. Zero-bias events are collected under the same beam conditions as the JP0, JP1 and JP2 events used in this analysis, allowing the simulation to track accurately the same beam background, pile-up and detector conditions as the actual dataset.

For this analysis, PYTHIA 6.4.28 with the Perugia 2012 tune is used to generate the events. An optimization of the tune was done in order to accommodate the lower center of mass energies at RHIC compared to the LHC where the PYTHIA tunes are generally developed. The change was motivated by the comparisons to published STAR single particle yields [36] [37]. Along with the hard QCD process, the initial state radiation, final state radiation, beam remnants and underlying event contributions are included in the input. The final state stable particles generated using PYTHIA are reconstructed using the same *Anti-k<sub>T</sub>* jet finding algorithm, used in the data analysis. These jets are called particle jets. Jets are also reconstructed at the parton level in order to study the hadronization effects. In this case, the hard scattered partons and those from the initial and final state radiations are used as input to the jet finding algorithm.

## 5.1 Embedding

The inelastic p+p scattering cross-section drops off very quickly as a function of partonic  $p_T$ , the transverse momentum of the scattered partons in the partonic center of mass frame. If the simulation was generated according to this minimum-bias cross-section, a prohibitive number of events would be required to match the number of high  $p_T$  events in the jet patch triggered data sample. In order to mitigate this issue, events are generated in bins of partonic  $p_T$  and weighted into a combined sample according to their luminosity,  $L = \sigma N$  where  $\sigma$  is the partonic cross-section and  $N$  is the number of events shown in columns 2 and 3 of Table 5.1. Note that PYTHIA overestimates the partonic cross-sections near the multi-parton interaction threshold, and to overcome this, "soft reweighting factors" are used to get the accurate weights from each of the partonic  $p_T$  bins. By applying these soft reweighting factors, a smooth partonic  $p_T$  spectrum will be obtained from the  $p_T$  distributions from all the partonic  $p_T$  bins (Figure 5.1). The partonic  $p_T$  bins, number of events generated,

Table 5.1: **Simulation statistics for the 2012 analysis** - Partonic  $p_T$  bins, number of events generated, cross sections and soft reweighting factors

$p_T$ Bin (GeV)	No. events	$\sigma$ ( $pb^{-1}$ )	Soft reweighting factor
2 - 3	593428	$2.87 \times 10^{10}$	0.60
3 - 4	388546	$5.87 \times 10^9$	0.83
4 - 5	362603	$2.87 \times 10^9$	0.93
5 - 7	616155	$5.87 \times 10^8$	0.97
7 - 9	410523	$2.87 \times 10^8$	1.0
9 - 11	388270	$5.87 \times 10^7$	0.99
11 - 15	638591	$2.87 \times 10^7$	0.99
15 - 20	447404	$5.87 \times 10^6$	0.99
20 - 25	291488	$2.87 \times 10^6$	1.0
25 - 35	324920	$5.87 \times 10^5$	1.0
35 - 45	137433	$2.87 \times 10^4$	1.0
45 - 55	85110	$5.87 \times 10^3$	0.99
55 - $\infty$	79807	$2.87 \times 10^3$	1.0

cross-sections and the soft reweighting factors used for this analysis are given in Table 5.1.

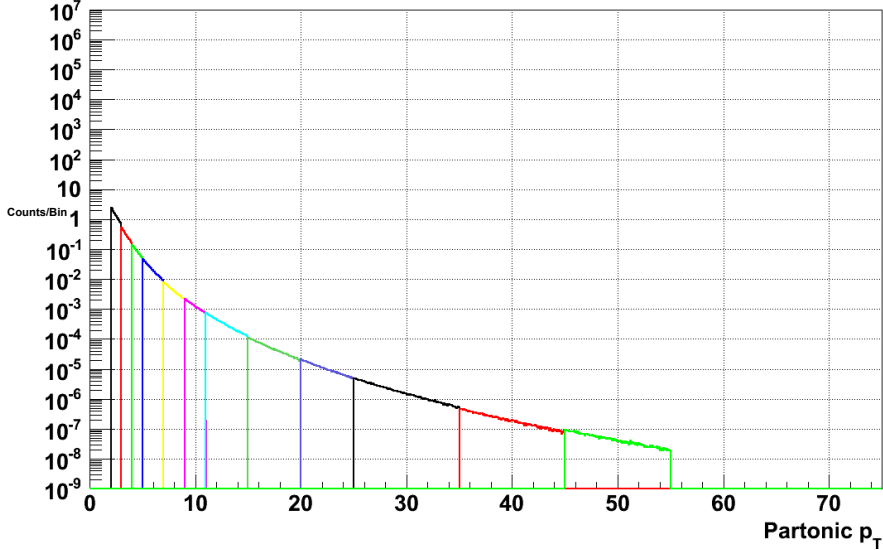


Figure 5.1: **Partonic  $p_T$  spectrum** - The partonic  $p_T$  spectrum after combining all the partonic  $p_T$  bins with the associated weights.

## 5.2 Data - Embedding Comparison

The integrity of the kinematic corrections and systematic errors determined using the embedding sample depends on how well the simulations emulate the data. To investigate this, comparisons of various jet and dijet variables in data and embedding were done. These include the underlying event corrected  $p_T$ ,  $\eta$ ,  $\phi$  and neutral energy fraction  $R_T$  for the leading and away-side jet in the dijet pair. The leading jet is defined as the highest  $p_T$  jet of the dijet pair. These also include the dijet  $M_{INV}$ ,  $\Delta\phi$  and  $\Delta\eta$  and the Z Vertex. The comparisons are shown in the following Figures.

The agreement between  $\eta$  and  $\phi$  in data and simulation is excellent and reflects the fact that the time dependence of the fiducial regions and the status of the detectors are correctly implemented. The track and tower multiplicities have the poorest agreement (compared to the other variables). This is a known issue in the STAR simulation and the main cause of the disagreement between the data and embedding is the underlying

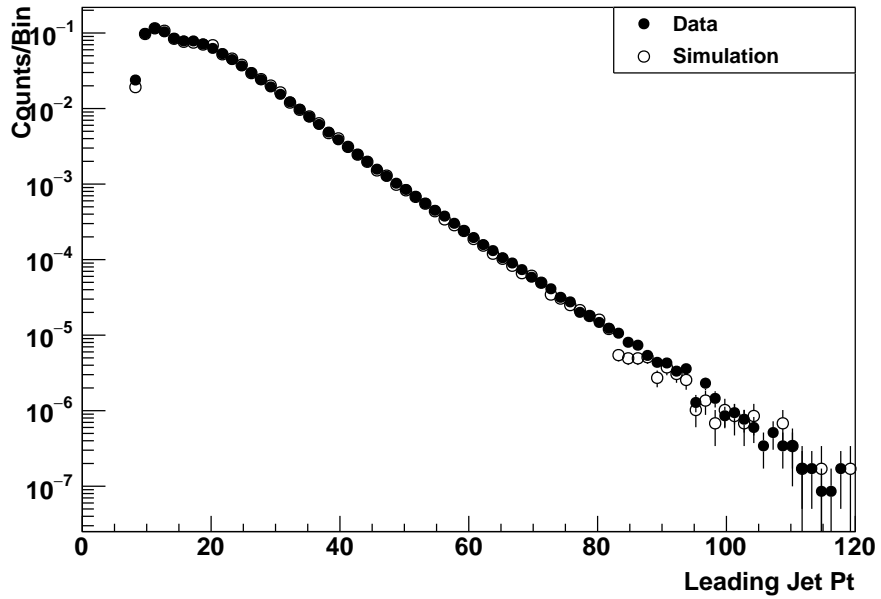


Figure 5.2: **Leading jet  $p_T$**  - The leading jet  $p_T$  distributions in data and simulation.

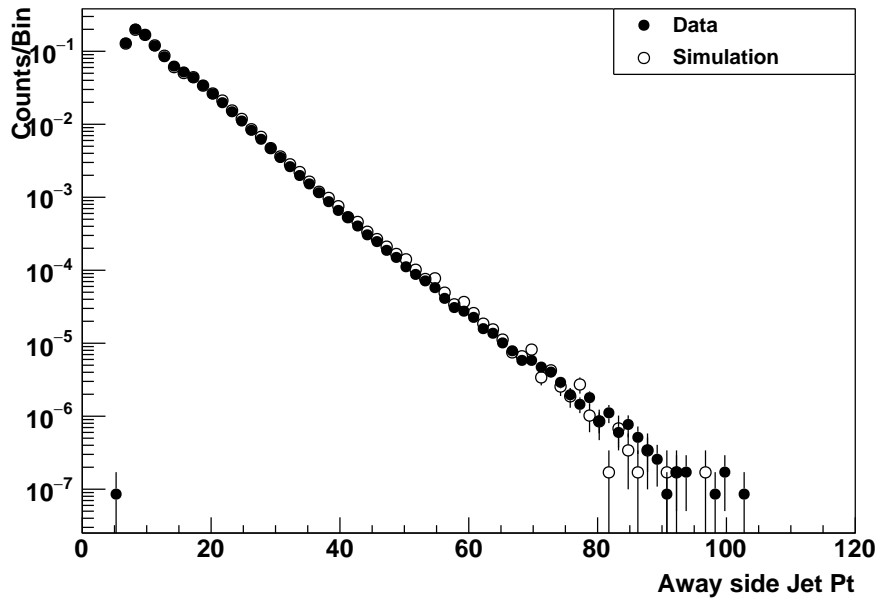


Figure 5.3: **Away-side jet  $p_T$**  - The away-side jet  $p_T$  distributions in data and simulation.

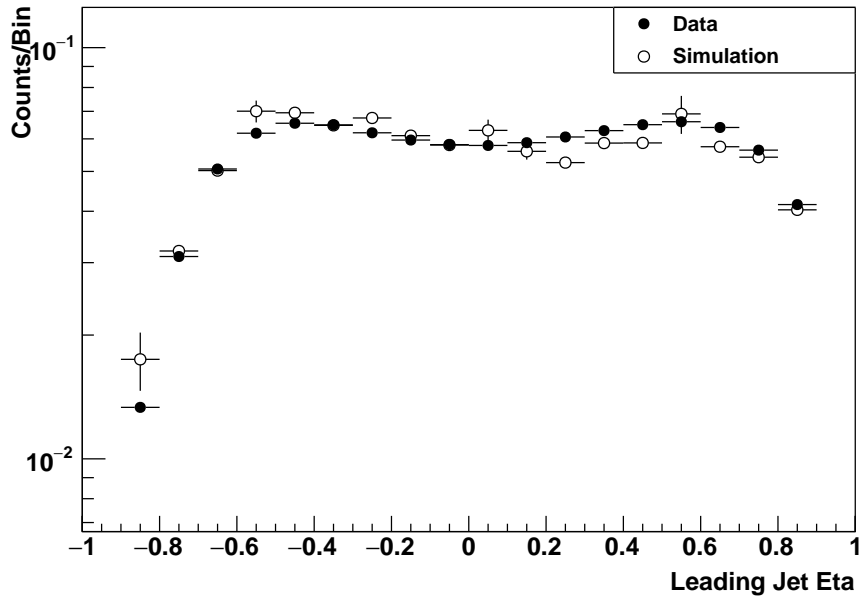


Figure 5.4: **Leading jet  $\eta$**  - The leading jet  $\eta$  distributions in data and simulation.

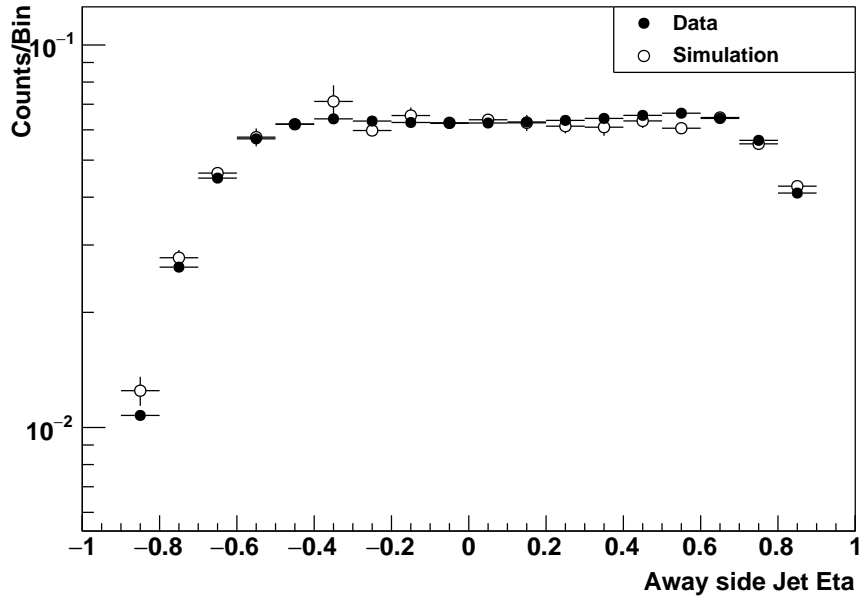


Figure 5.5: **Away-side jet  $\eta$**  - The away-side jet  $\eta$  distributions in data and simulation.



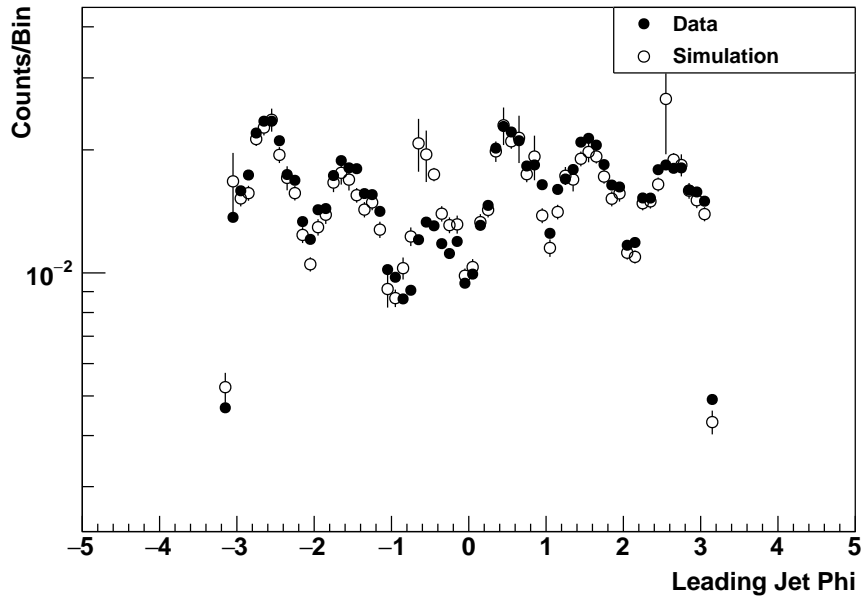


Figure 5.6: **Leading jet  $\phi$**  - The leading jet  $\phi$  distributions in data and simulation.

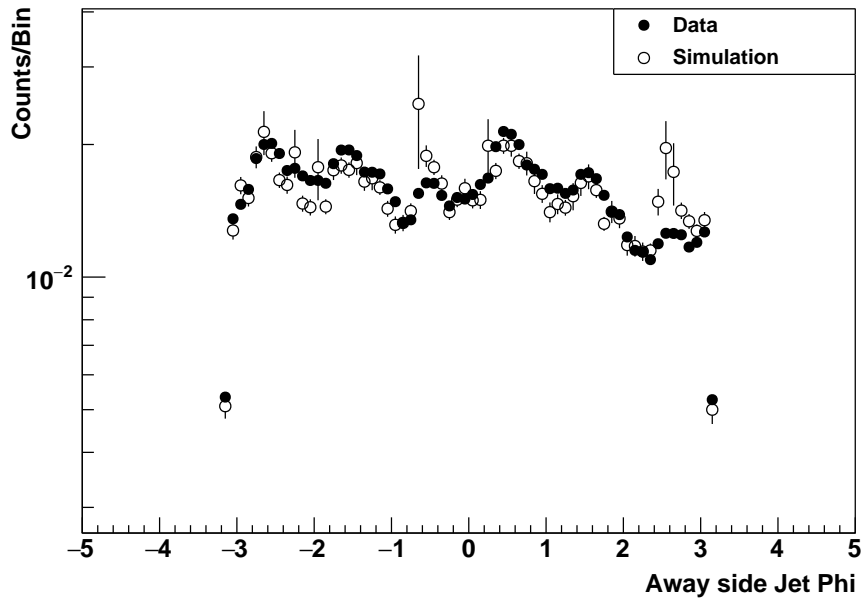


Figure 5.7: **Away-side jet  $\phi$**  - The away-side jet  $\phi$  distributions in data and simulation.

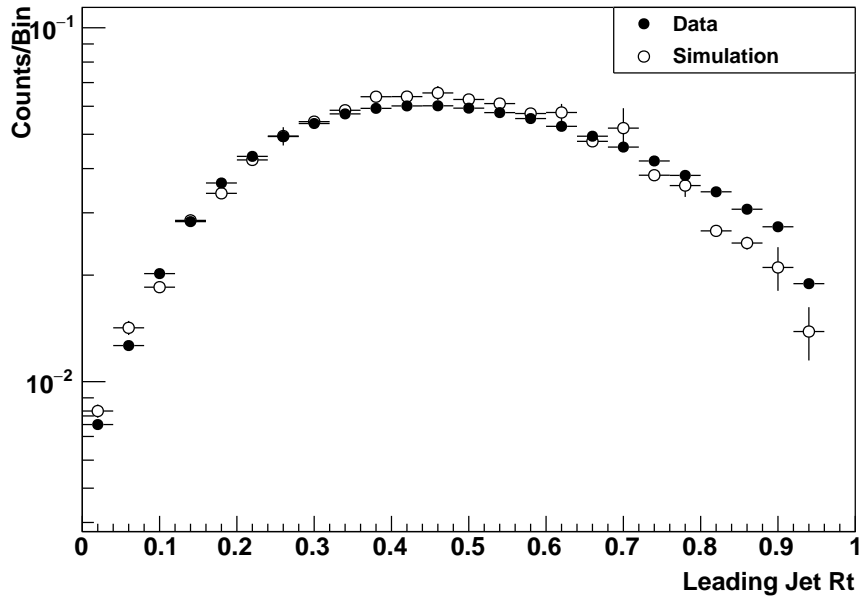


Figure 5.8: **Leading jet  $R_T$**  - The leading jet  $R_T$  distributions in data and simulation.

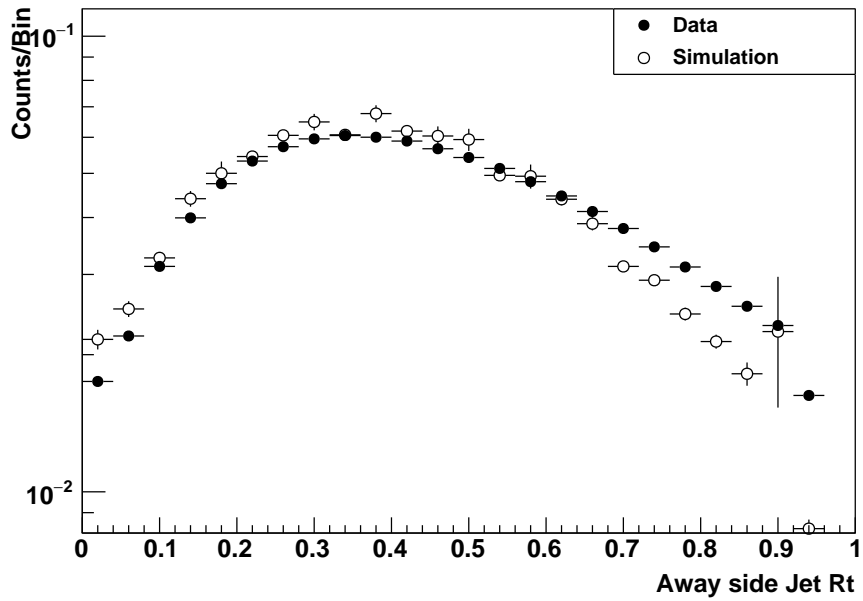


Figure 5.9: **Away-side jet  $R_T$**  - The away-side jet  $R_T$  distributions in data and simulation.

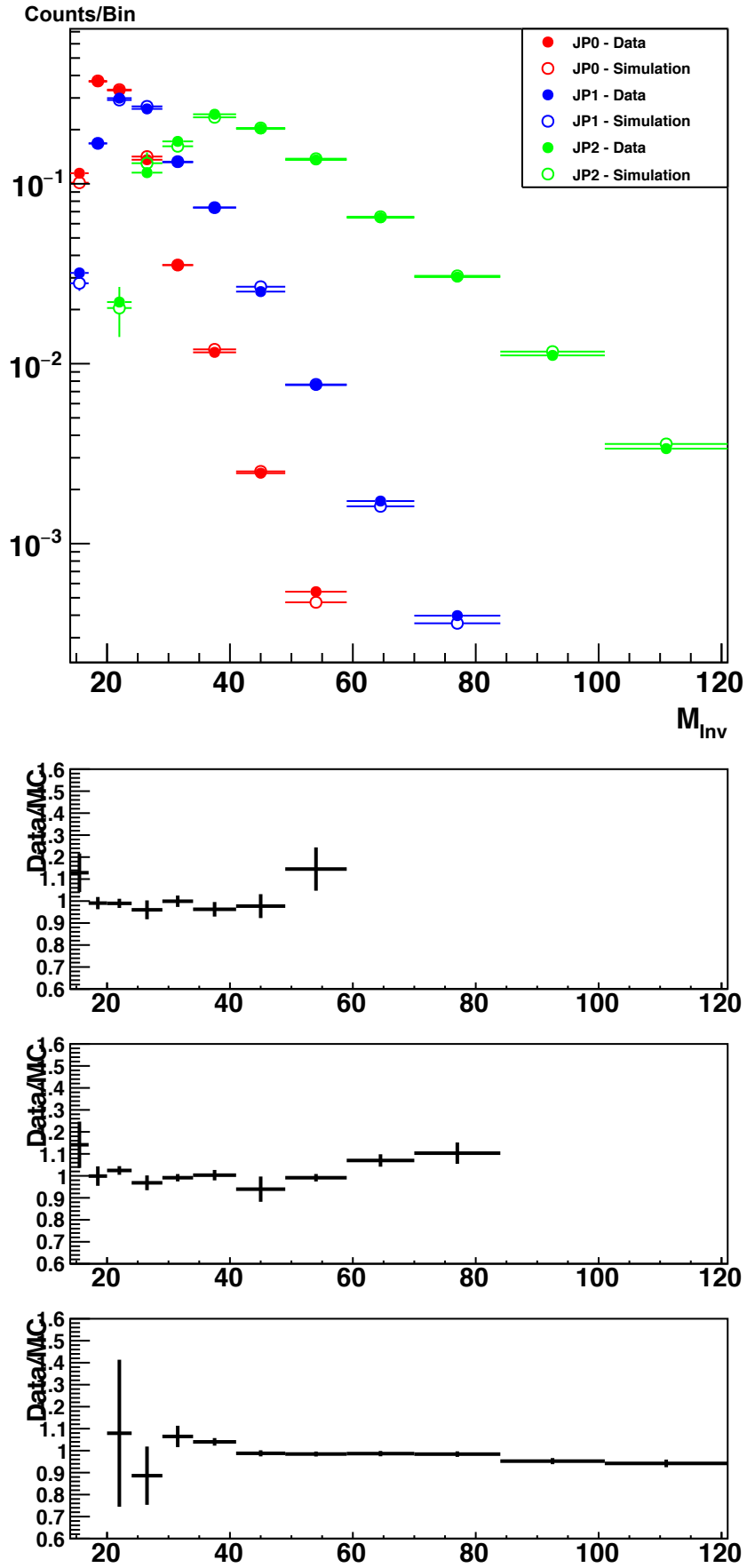


Figure 5.10: Dijet  $M_{inv}$  - The dijet  $M_{inv}^{A7}$  distributions in data and simulation.

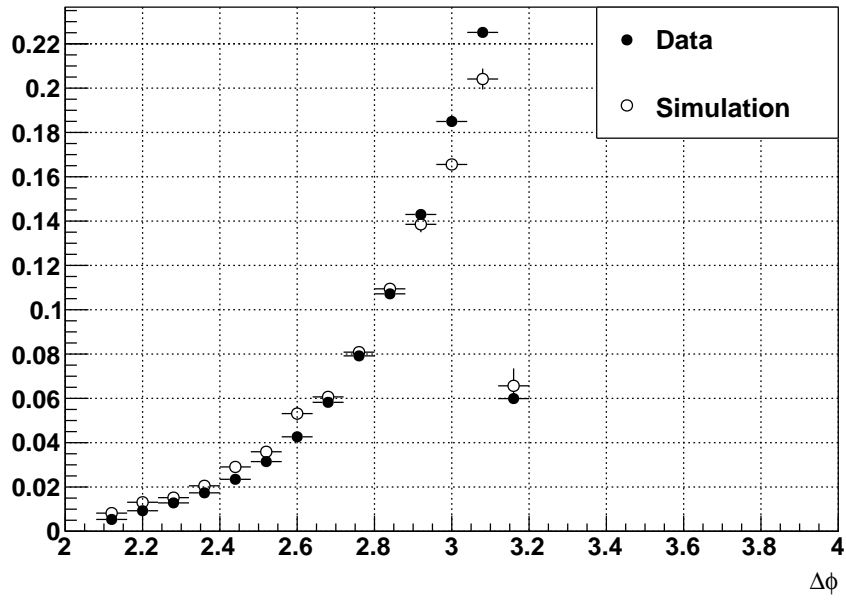


Figure 5.11: **Dijet  $\Delta\phi$**  - The dijet  $\Delta\phi$  distributions in data and simulation.

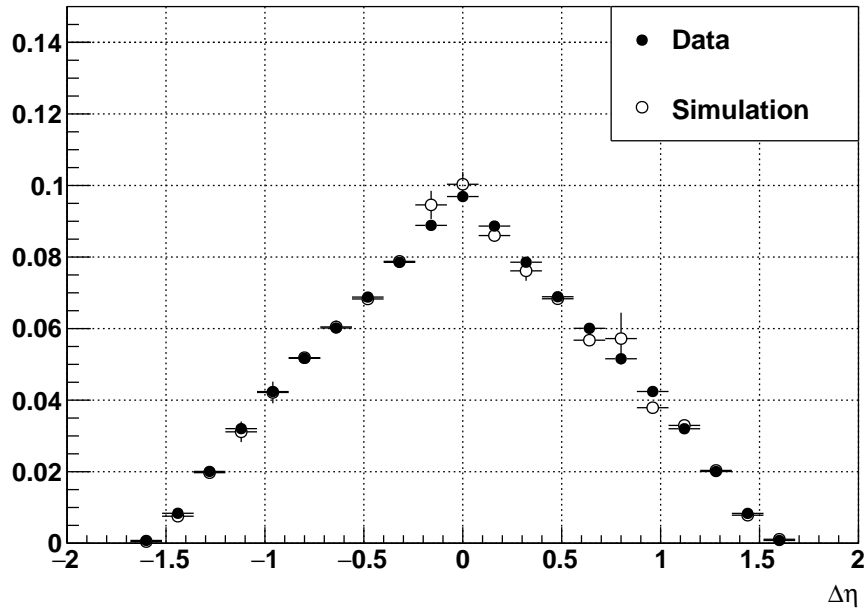


Figure 5.12: **Dijet  $\Delta\eta$**  - The dijet  $\Delta\eta$  distributions in data and simulation.

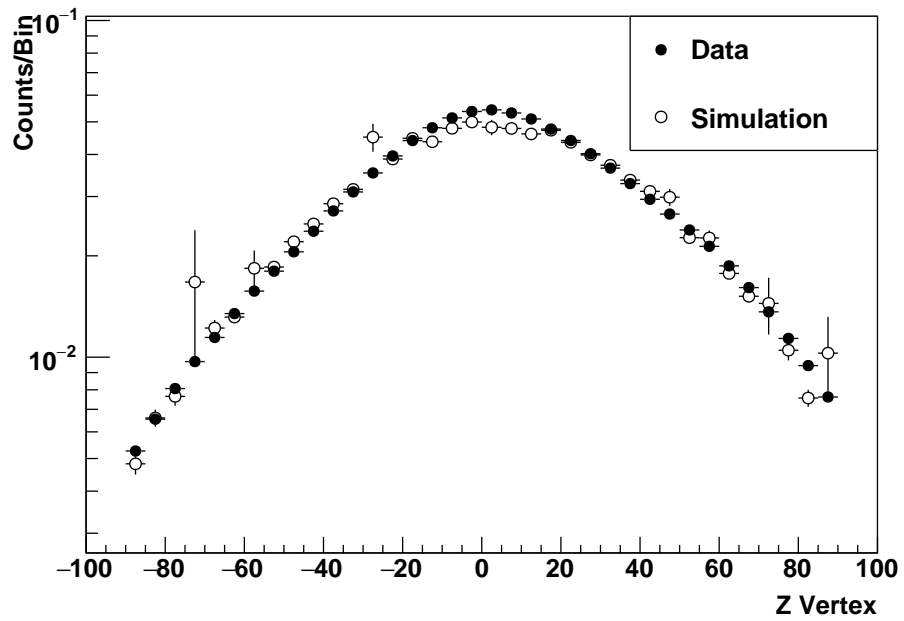


Figure 5.13: **Z Vertex** - The Z Vertex distributions in data and simulation.

event correction. The  $M_{inv}$  embedding is used to correct for the dijet invariant mass.

To summarize, all of the data - embedding comparisons show very good agreement.

## Chapter 6 Dijet Longitudinal Double Spin Asymmetry

### 6.1 Introduction

At RHIC, the primary observable used to study the gluon spin contribution ( $\Delta G$ ) to the spin of the proton, is the longitudinal double spin asymmetry,  $A_{LL}$ .  $A_{LL}$  is defined as the ratio of the difference to the sum of the cross sections for parallel and anti-parallel initial spin states, as given by Eq. 6.1.

$$A_{LL} = \frac{\sigma^{++} - \sigma^{+-}}{\sigma^{++} + \sigma^{+-}} \quad (6.1)$$

where  $\sigma^{++}$  and  $\sigma^{+-}$  are the dijet cross sections with same and opposite helicities for the initial state protons.

### 6.2 Calculation of $A_{LL}$

#### 6.2.1 Spin Bits

At STAR, the spin configurations of the colliding bunches are number-coded (also known as spin bits). Each spin bit indicates a unique combination of the the spin states of the initial protons. Table 6.1 shows the spin configurations and the corresponding helicities for the yellow and blue beams.

Table 6.1: **Spin configurations** - Spin configurations and corresponding beam helicities

Spin Bit	Yellow	Blue
5	+	+
6	-	+
9	+	-
10	-	-

### 6.2.2 Definition of $A_{LL}$

In this analysis, instead of directly measuring the total cross sections for the four different spin configurations, the dijet yields, plotted as a function of invariant mass bins, for the four spin states and relative luminosities are used. The dijet yields ( $N$ ) can be correlated to the cross sections ( $\sigma$ ) as shown in Eq. 6.2, where  $L$  denotes the luminosity.

$$N = L \times \sigma \quad (6.2)$$

The ratio of integrated luminosities is defined as  $R_3$  (relative luminosity):

$$R_3 = \frac{L^{++} + L^{--}}{L^{+-} + L^{-+}} \quad (6.3)$$

The experimentally observed asymmetry needs to also account for the polarizations of the two beams. Eq 6.4 shows how  $A_{LL}$  is experimentally determined for a single run:

$$A_{LL} = \frac{1}{P_Y P_B} \frac{(N^{++} + N^{--}) - R_3(N^{+-} + N^{-+})}{(N^{++} + N^{--}) + R_3(N^{+-} + N^{-+})} \quad (6.4)$$

Here  $P_A$  and  $P_B$  denote the polarizations of the yellow and blue beams,  $N^{++}$ ,  $N^{--}$ ,  $N^{+-}$  and  $N^{-+}$  denote the spin-sorted yields.

The statistical error on  $A_{LL}$  for a single run is calculated using the technique of partial derivatives as:

$$\sigma_{A_{LL}} = \left[ \left( \frac{\partial A_{LL}}{\partial P_B} \sigma_{P_B} \right)^2 + \left( \frac{\partial A_{LL}}{\partial P_Y} \sigma_{P_Y} \right)^2 + \left( \frac{\partial A_{LL}}{\partial R_3} \sigma_{R_3} \right)^2 + \sum_{spinstates} \left( \frac{\partial A_{LL}}{\partial N_{ij}} \sigma_{N_{ij}} \right)^2 \right]^{\frac{1}{2}} \quad (6.5)$$

After calculating the  $A_{LL}$  and its error for a single run, the method of weighted averages is used to calculate the  $A_{LL}$  and the error on  $A_{LL}$  for the full 479 runs. Eq. 6.6 and Eq. 6.7 show the calculation of  $A_{LL}$  and its error for the entire Run.

$$A_{LL}^{Total} = \sum_{run} \frac{A_{LL}^{run}}{(\sigma_{A_{LL}}^{run})^2} / \sum_{run} \left( \frac{1}{\sigma_{A_{LL}}^{run}} \right)^2 \quad (6.6)$$

$$\sigma_{A_{LL}}^{Total} = \sqrt{\sum_{run} \left( \frac{1}{\sigma_{A_{LL}}^{run}} \right)^2} \quad (6.7)$$

For each run, the dijet yields for the four spin configurations are counted and categorized using a trigger algorithm to ensure that a mutually exclusive sample is obtained.

### 6.2.3 Relative Luminosities

In order to account for the different numbers of collisions for the four different spin configurations of the two beams, ++, +-, -+ and --, each count must be normalized by the associated luminosity. There are six relative luminosity ratios defined by Eqs. 6.8 - 6.13.  $R_1$  and  $R_2$  are associated with the single spin asymmetry measurements for the yellow and blue beams respectively.  $R_3$  is used for the  $A_{LL}$  calculation, and  $R_4$ ,  $R_5$  and  $R_6$  are used in the calculation of the like and unlike sign spin asymmetries. Relative luminosities are calculated on a run-by-run basis, from the numbers of events recorded using the STAR relative luminosity sub-detectors BBC, ZDC and VPD. A scaler system counts the number of coincidences, east and west singles are detected by the VPD. The coincidences are corrected for accidentals and multiple coincidences. The BBC and ZDC scalers were used to provide a systematic error estimate on the VPD relative luminosity determination.

$$R_1 = \frac{L^{++} + L^{-+}}{L^{+-} + L^{--}} \quad (6.8)$$



$$R_2 = \frac{L^{++} + L^{+-}}{L^{-+} + L^{--}} \quad (6.9)$$

$$R_3 = \frac{L^{++} + L^{--}}{L^{+-} + L^{-+}} \quad (6.10)$$

$$R_4 = \frac{L^{++}}{L^{--}} \quad (6.11)$$

$$R_5 = \frac{L^{-+}}{L^{--}} \quad (6.12)$$

$$R_6 = \frac{L^{+-}}{L^{--}} \quad (6.13)$$

#### 6.2.4 Beam Polarization

The proton-Carbon (pC) [38] polarimeter and Hydrogen-jet polarimeter [39] are used to measure the beam polarization. The H-jet polarimeter provides an absolute beam polarization measurement, while the pC polarimeter measures a series of intensity averaged polarizations over the period of one fill. The measured polarizations are then fitted to the form  $P(t) = P_0 - P' \times t$ , where  $P(t)$  is the polarization measured at time  $t$ ,  $P_0$  is the polarization at the start of the fill ( $t_0$ ) and  $P'$  is the absolute polarization loss rate. The fill-by-fill fitted parameters  $P_0$  and  $P'$  and the starting time  $t_0$  are obtained. For a specific run, the polarization is calculated using the expression  $P(t) = P_0 - P' \times t$ .

The relative luminosity and beam polarization values used in this analysis were initially calculated by Dr. Zilong Chang for the 2012 Inclusive Jet  $A_{LL}$  at 510GeV [36].

### 6.2.5 Detector Topologies

Reconstruction of dijets gives access to the initial partonic kinematics. Equations 6.14 and 6.15 express  $x_1$  and  $x_2$ , the partonic momentum fractions in the infinite momentum frame, in terms of the jet  $p_T$ ,  $\eta$  and  $s$ . Note that this formulation is true only at leading order.

$$x_1 = \frac{1}{\sqrt{s}}(p_{T_3}e^{\eta_3} + p_{T_4}e^{\eta_4}) \quad (6.14)$$

$$x_2 = \frac{1}{\sqrt{s}}(p_{T_3}e^{-\eta_3} + p_{T_4}e^{-\eta_4}) \quad (6.15)$$

Table 6.2: **Detector Topologies** - The four detector topologies along with the corresponding jet  $\eta$  regions. The approximate values of  $x_1$  and  $x_2$  are given based on  $p_T = 10$  GeV

Topology	Jet 1	Jet 2	$x_1$	$x_2$
A	Forward	Forward	0.071	0.022
	Backward	Backward	0.022	0.071
B	Forward	Middle	0.055	0.030
	Middle	Forward	0.055	0.030
	Backward	Middle	0.030	0.055
	Middle	Backward	0.030	0.055
C	Middle	Middle	0.039	0.039
D	Forward	Backward	0.046	0.046
	Backward	Forward	0.046	0.046

Accessing dijets in different detector topologies gives access to different  $x$  regions. It also gives access to different  $\cos(\theta^*)$  regions.  $\cos(\theta^*)$ , where  $\theta^*$  is the scattering angle in the parton center of mass frame, enters into the theoretical expression for the partonic  $a_{LL}$ . In order to do this, three different detector ( $\eta$ ) regions are defined - Forward ( $0.3 < \eta < 0.9$ ), Middle ( $-0.3 < \eta < 0.3$ ) and Backward ( $-0.9 < \eta < -0.3$ ). These three  $\eta$  regions help define four different topologies as shown in Table 6.2.

Topologies A and C accesses collisions where  $\cos(\theta^*)$  is close to zero, while topologies B and D accesses collisions with larger values of  $\cos(\theta^*)$ .

### 6.3 False Asymmetries

In addition to the longitudinal double spin asymmetry ( $A_{LL}$ ), four additional asymmetries can be calculated in order to provide cross checks on the analysis scheme and the relative luminosity determinations. These asymmetries are the yellow beam single spin asymmetry ( $A_Y$ ), the blue beam single spin asymmetry ( $A_B$ ), the like sign double spin asymmetry ( $A_{LS}$ ) and unlike sign double spin asymmetry ( $A_{US}$ ). They can be calculated using equations 6.16 - 6.19 where  $P_B$  and  $P_Y$  are the yellow and the blue beam polarizations and  $R_1, R_2, R_4, R_5$  and  $R_6$  are the relative luminosities.

$$A_Y = \frac{1}{P_Y} \frac{(N^{++} + N^{-+}) - R_1(N^{+-} + N^{--})}{(N^{++} + N^{-+}) + R_1(N^{+-} + N^{--})} \quad (6.16)$$

$$A_B = \frac{1}{P_B} \frac{(N^{++} + N^{+-}) - R_2(N^{-+} + N^{--})}{(N^{++} + N^{+-}) + R_3(N^{-+} + N^{--})} \quad (6.17)$$

$$A_{LS} = \frac{1}{P_Y P_B} \frac{(N^{++} - R_4 N^{--})}{(N^{++} + R_4 N^{--})} \quad (6.18)$$

$$A_{US} = \frac{1}{P_Y P_B} \frac{(R_5 N^{+-} - R_6 N^{-+})}{(R_5 N^{+-} + R_6 N^{-+})} \quad (6.19)$$

These asymmetries are sensitive to parity violating interactions, but should be consistent with zero for the current statistical precision. As seen from Figures 6.1 - 6.4, all four of the false asymmetries are consistent with zero.

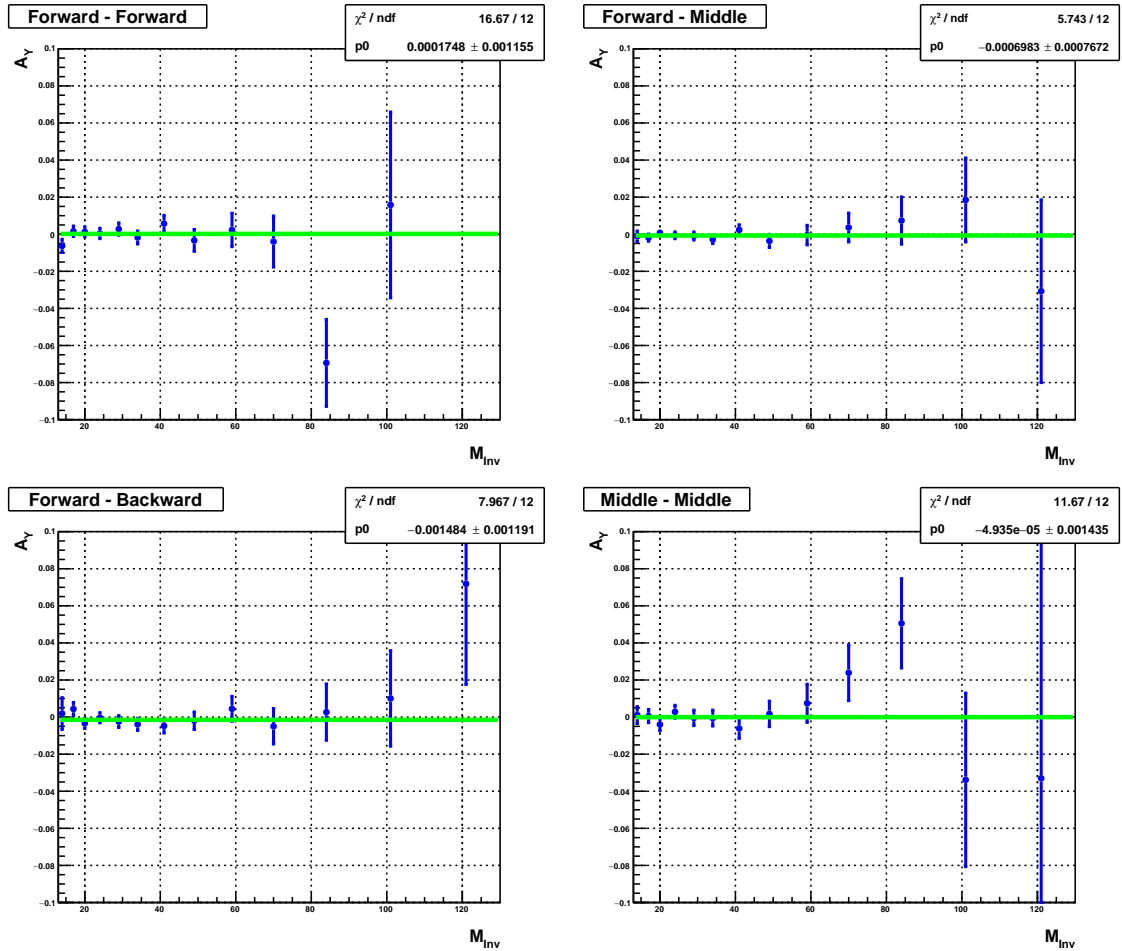


Figure 6.1:  $A_Y$  - Single spin asymmetry for the yellow beam for the different topologies.

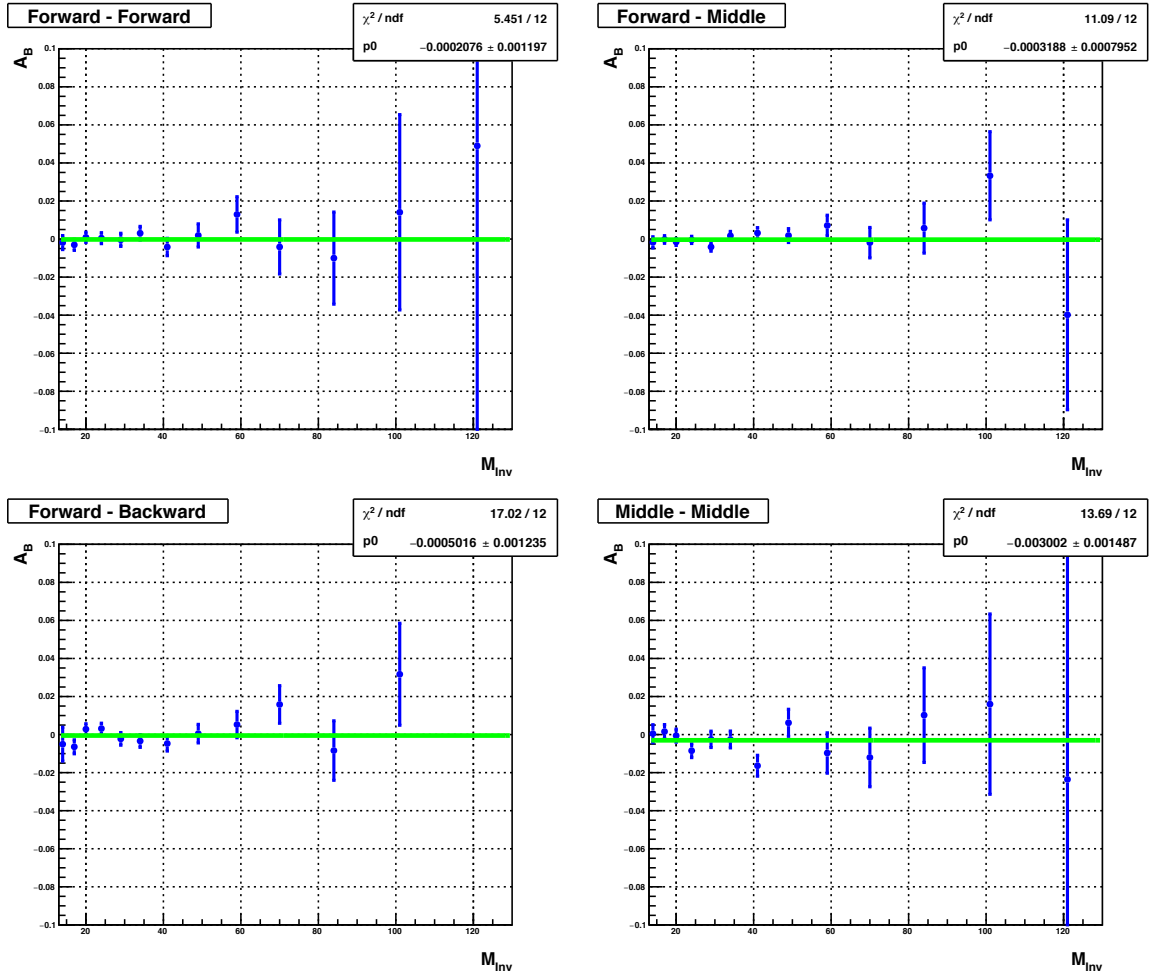


Figure 6.2:  $A_B$  - Single spin asymmetry for the blue beam for the different topologies.

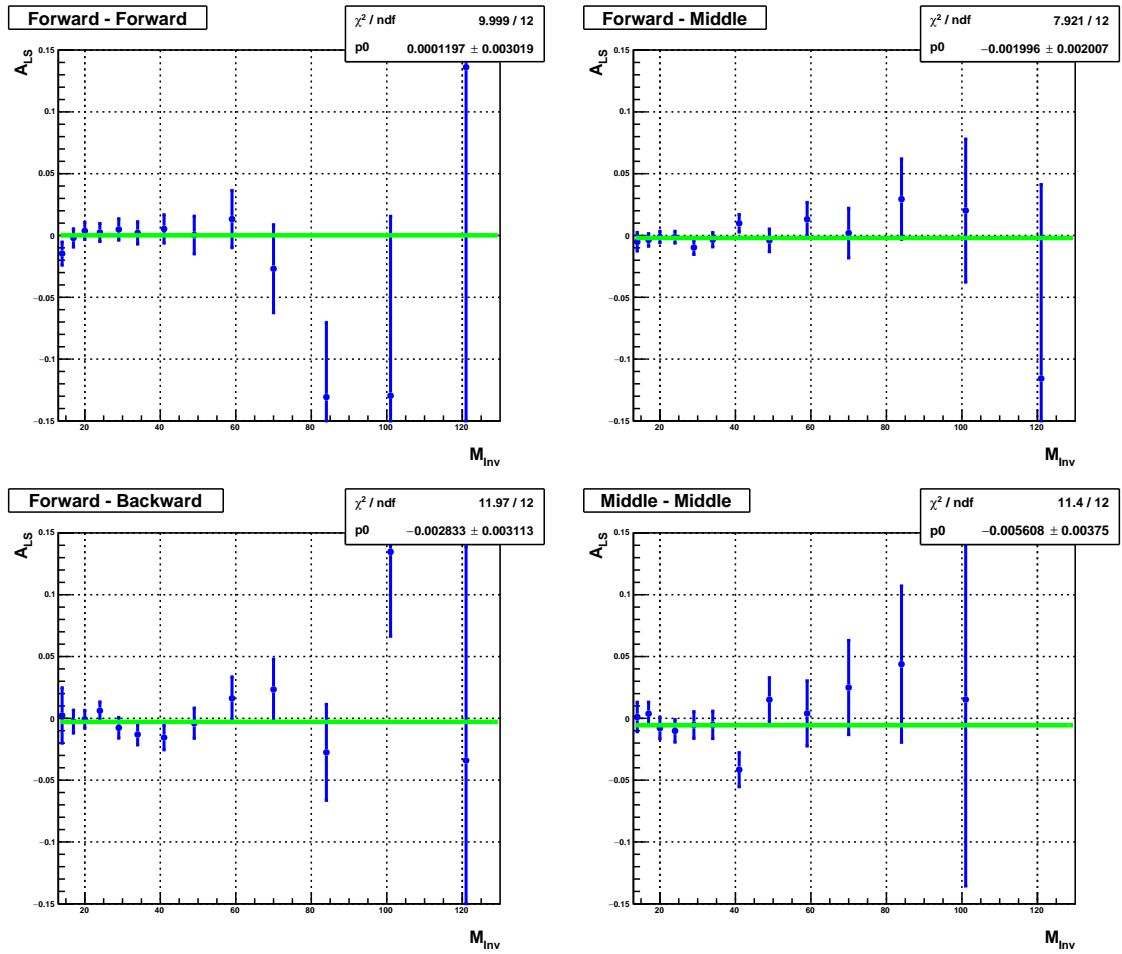


Figure 6.3:  $A_{LS}$  - Like sign double spin asymmetry for the different topologies.

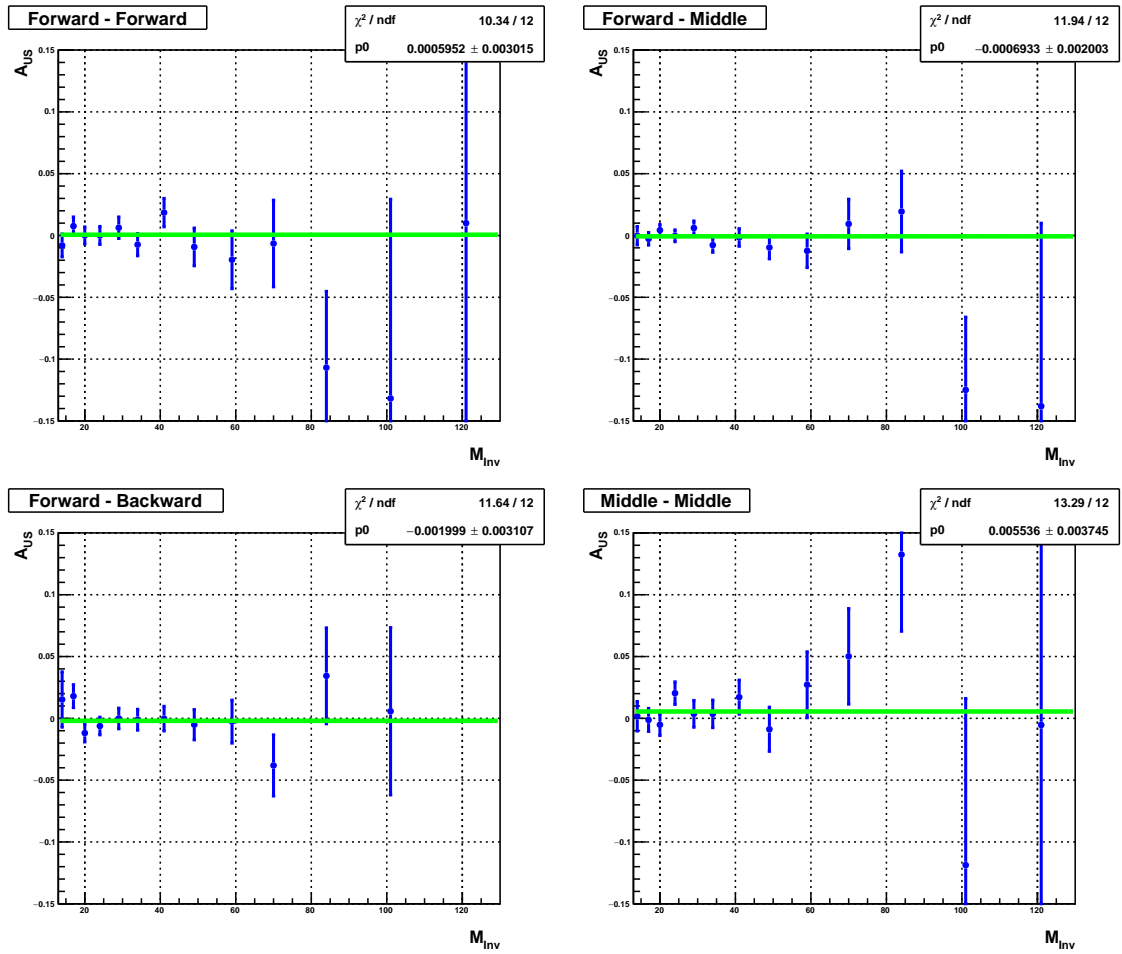


Figure 6.4:  $A_{US}$  - Unlike sign double spin asymmetry for the different topologies.

## 6.4 Corrections

### 6.4.1 Invariant Mass Shift

The theoretical predictions corresponding to the dijet  $A_{LL}$  results are calculated at next-to-leading order. These NLO calculations do not include hadronization effects. Therefore, to do comparisons with theory, the corrections on the dijet invariant mass needs to be scaled back to the parton level. In order to do this, first the detector level invariant mass and the matching parton level invariant mass in simulation are plotted event-by-event in a 2D graph. Then using a profile histogram, the corresponding parton level invariant mass, also referred to as the "corrected invariant mass" is extracted for each detector invariant mass bin. The final data points are plotted at these corrected invariant mass points. Figure 6.5 shows the parton-detector matching and the corrected invariant mass points for all the four different detector topologies.

### 6.4.2 Trigger and Reconstruction Bias

The three dominant 2-2 partonic scattering subprocesses in proton-proton collisions at  $\sqrt{s} = 510\text{GeV}$  are quark-quark, quark-gluon and gluon-gluon scattering. The measured dijet  $A_{LL}$  is a mixture of the partonic  $a_{LL}$  of these subprocesses. The probability of each type of scattering is well known and determined by the unpolarized PDFs. The fraction of qq,qg and gg for a given dijet  $M_{inv}$  bin may be altered by biases in both the jet reconstruction and trigger algorithm. For example, on average gluon jets are less collimated than quark jets. The fixed size of the jet patch trigger favors more collimated jets that can fit more of their total energy inside of a patch. In this case the trigger may enhance the collection of quark vs. gluon jets. This, in the end, leads to more sensitivity towards certain sub-processes than others, resulting in a "trigger and reconstruction bias".



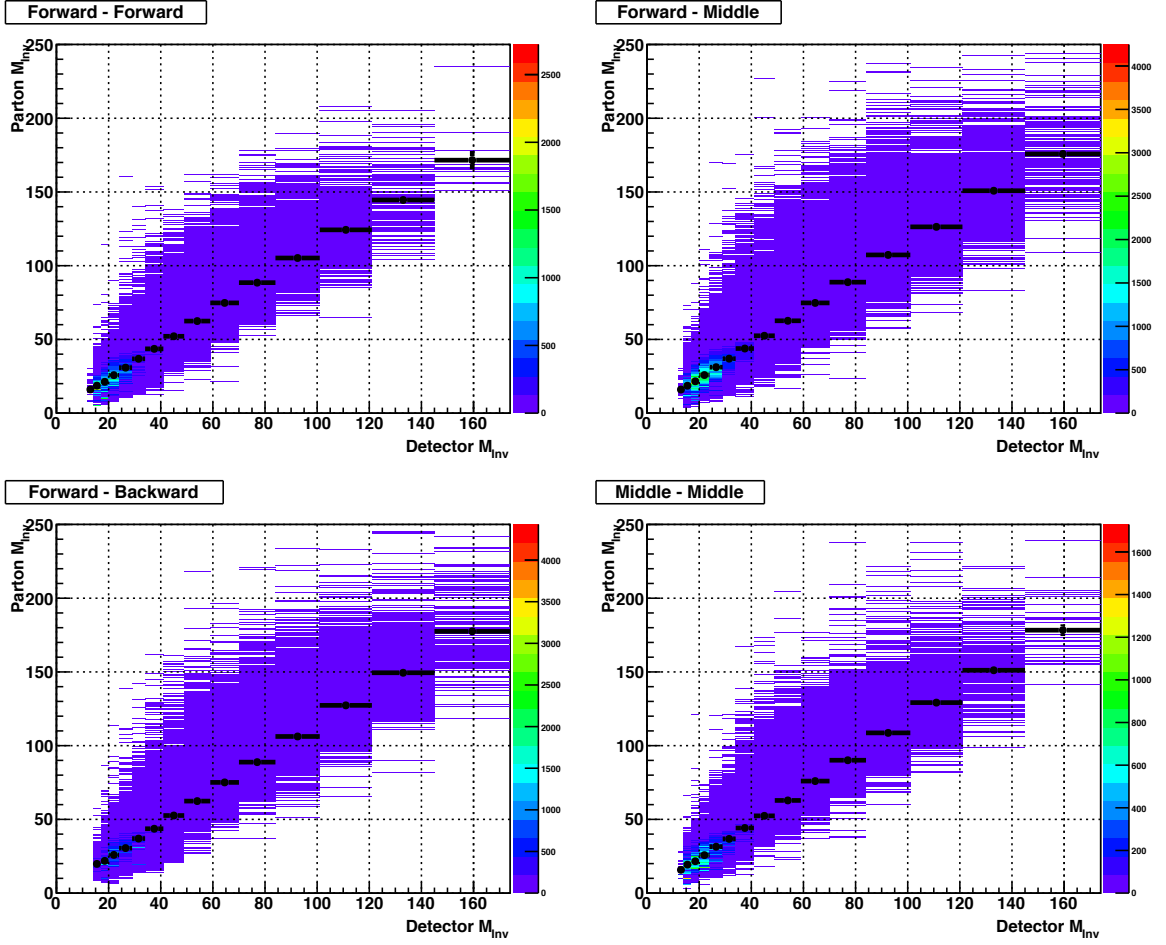


Figure 6.5: **Corrected  $M_{inv}$**  - The dijet  $M_{inv}$  distributions at the detector and parton levels in simulation, with the profile histograms denoting the corrected invariant mass points for each detector bin, for the different detector topologies.

For the reasons discussed above the magnitude of the trigger bias depends on the same polarized PDFs we aim to constrain with our measurements. Therefore the general approach to estimating jet reconstruction and trigger bias correction is to use a sampling of PDFs that represent equally probable gluon helicity distributions.  $A_{LL}$  predictions as a function of the dijet invariant mass are generated by using the parametrization of the polarized parton distribution functions combined with the PYTHIA partonic kinematics, both at the detector and parton level. The polarized PDFs used here are the 100 replicas from the NNPDF group for their NNPDFpol1.1 global fit [6] and the unpolarized PDF is the unpolarized PDF from the same group

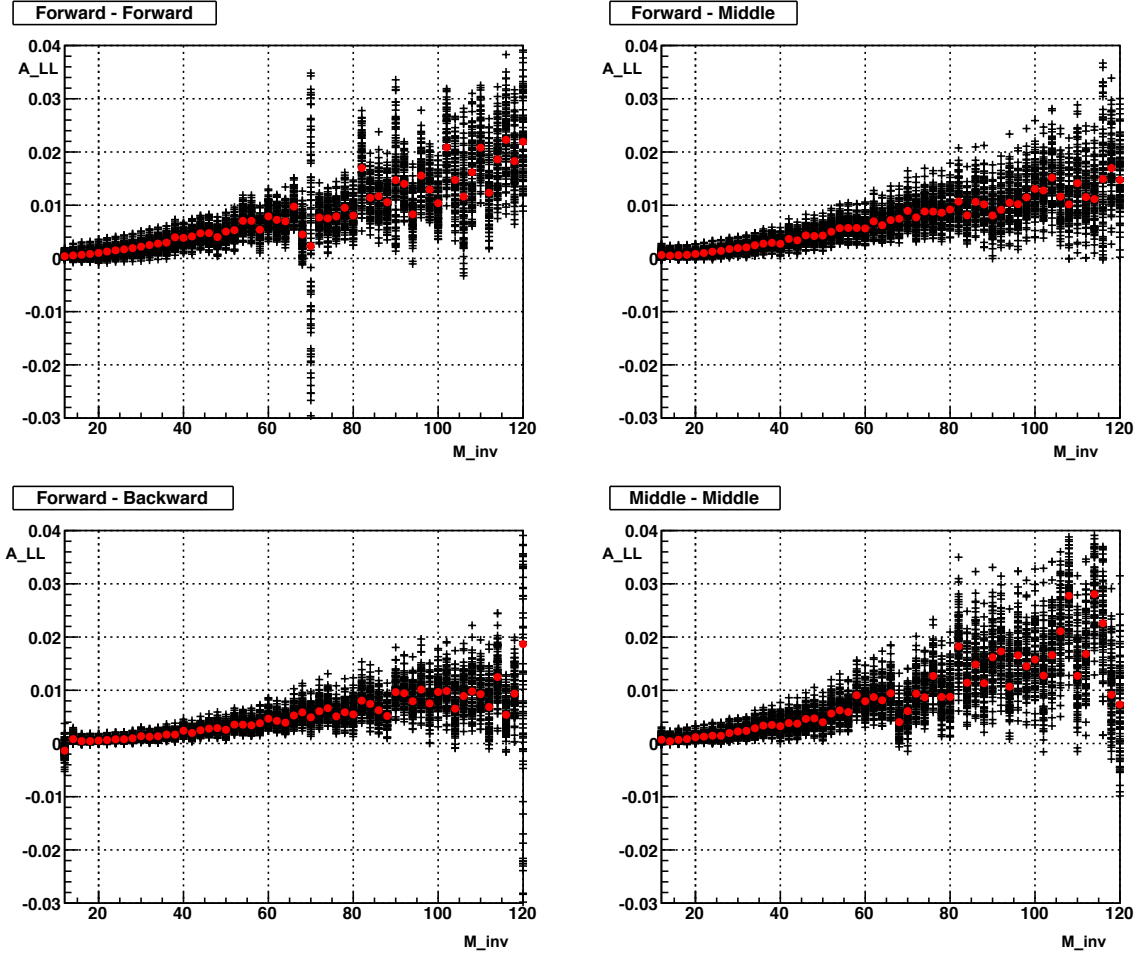


Figure 6.6: **Parton level Dijet  $A_{LL}$**  - Dijet  $A_{LL}$  for the parton level jets from embedding, for the 100 NNPDF replicas (black) and the NNPDF best fit (red).

NNPDF2.3 [40]. For each event, the parton level dijet  $A_{LL}$  from the full PYTHIA sample is calculated, after applying the dijet  $\Delta\phi$  cut, the jet  $\eta$  cuts and the asymmetric  $p_T$  cut. Similarly, the detector level dijet  $A_{LL}$  is also calculated, but from the triggered simulation sample after applying all the detector level cuts. Figures 6.6 and 6.7 show the parton and detector level  $A_{LL}$  distributions for the 100 replicas for the four different topologies. Each black point represents one of the replicas and the red points are from the NNPDF best fit. Then, the difference between detector level  $A_{LL}$  and parton level  $A_{LL}$  (evaluated at the corrected mass points) is calculated for the 100 NNPDF replicas. The mean of these 100 differences is called the "model correction"

and is applied as a shift to the final measured  $A_{LL}$ .

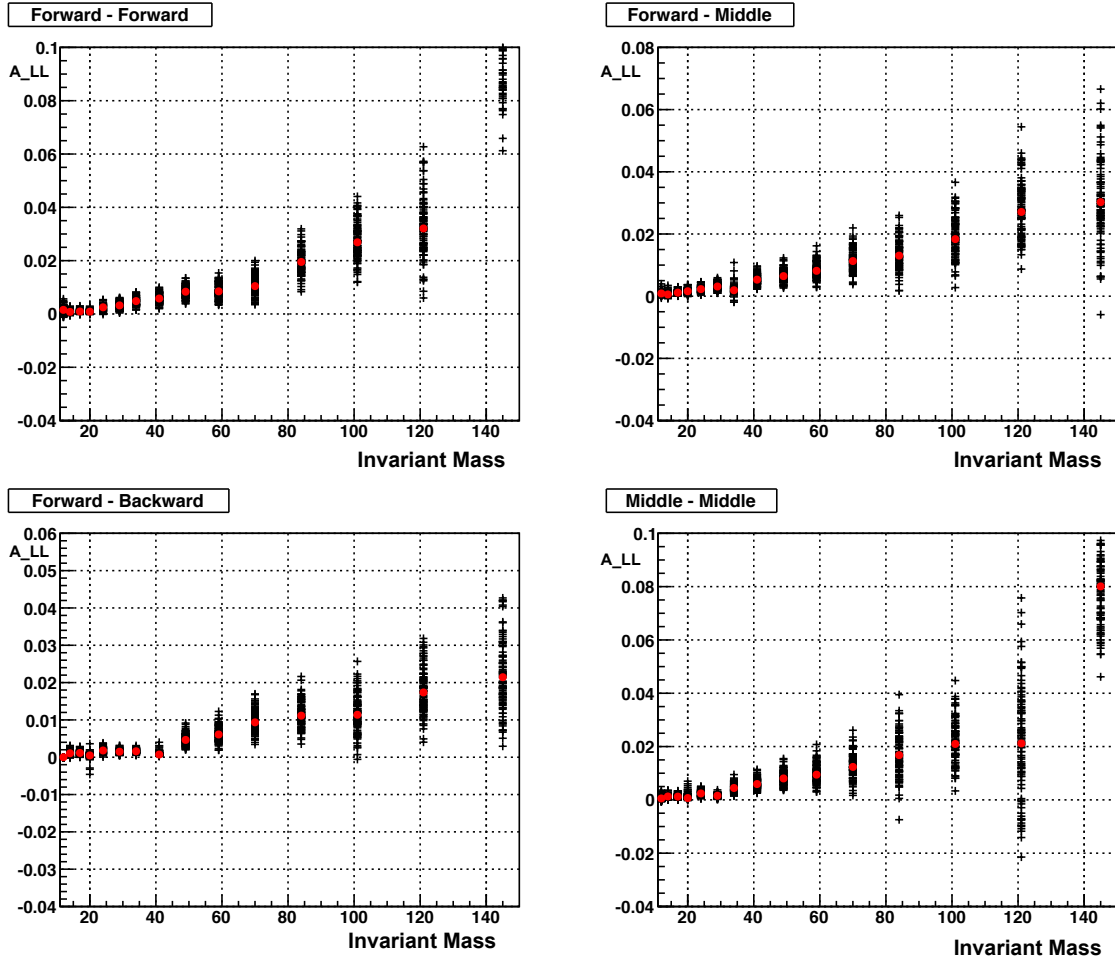


Figure 6.7: **Detector level Dijet  $A_{LL}$  - Dijet  $A_{LL}$**  for the detector level jets from embedding, for the 100 NNPf replicas (black) and the NNPf best fit (red).

## Chapter 7 Systematic Uncertainties

The systematic uncertainties associated with the dijet  $A_{LL}$  include contributions from the relative luminosity, the underlying event, the trigger and reconstruction bias, the dilution due to vertex finding and the uncertainties due to the transverse residual double spin asymmetry and non-collision background. The uncertainty on the dijet  $M_{inv}$  are also calculated. The jet energy scale uncertainty contributes to the uncertainty on the dijet  $M_{inv}$ , and all of the others contribute towards the uncertainty on the dijet  $A_{LL}$ .

### 7.1 Underlying Event and Relative Luminosity Systematic

For this dataset, the relative luminosities were measured at STAR by the spin-sorted yields from the BBC, ZDC and VPD sub-detectors, and the yields from the VPD were used for the final values. Relative luminosities were also calculated using the ZDC system, and the difference between the BBC and ZDC values, was used in estimating systematic errors. The  $\Delta A_{LL}$  due to the systematic uncertainty of relative luminosity was calculated as follows - the dijet  $A_{LL}$  can be re-written as:

$$A_{LL} = \frac{1}{P_A P_B} \frac{N^+/N^- - R_3}{N^+/N^- + R_3} \quad (7.1)$$

Denoting  $R_N = N^+/N^-$ , the uncertainty on  $A_{LL}$  due to the relative luminosity uncertainty, can be written as:

$$\Delta A_{LL} = \frac{1}{P_A P_B} \frac{2 * R_N}{(R_N + R_3)^2} \Delta R_3 \quad (7.2)$$

Rewriting  $R_N$  in terms of the polarizations and  $A_{LL}$ , the above equation becomes:

$$\Delta A_{LL} = \frac{1}{P_A P_B} \frac{1 - (P_A P_B A_{LL})^2}{2} \frac{\Delta R_3}{R_3} \quad (7.3)$$

Assuming the approximate values of polarizations as 0.54 and 0.55, and neglecting the second order term in  $A_L L$ , the simplified equation then becomes:

$$\Delta A_{LL} = \frac{1}{2P_A P_B} \frac{\Delta R_3}{R_3} \quad (7.4)$$

The value of  $\Delta R_3/R_3$  was calculated for the 2012 inclusive jet analysis [36] as 0.00013, and using this the systematic uncertainty on  $A_L L$  due to the relative luminosity uncertainty can be calculated to be 0.0002.

The systematic uncertainty due to the underlying event contribution can be split into the spin-dependent and spin-independent contributions. The spin-independent piece goes into the Jet Energy Scale systematic, while the spin-dependent piece is combined with the relative luminosity systematic.

If the UE has a spin dependence, it can distort the measured dijet  $A_{LL}$  values. To examine this possibility, the longitudinal double-spin asymmetry of the underlying event contributions,  $A_{LL}^{dM_{inv}}$  is measured. It can be defined as:

$$A_{LL}^{dM} = \frac{1}{P_A P_B} \frac{\langle dM \rangle^{++} - \langle dM \rangle^{+-}}{\langle dM \rangle^{++} + \langle dM \rangle^{+-}}, \quad (7.5)$$

where  $\langle dM \rangle^{++}$  and  $\langle dM \rangle^{+-}$  are the average underlying event corrections for same and opposite beam helicity combinations. Figure 7.1 shows the observed  $A_{LL}^{dM}$  as a function of the dijet  $M_{inv}$ . The values of  $A_{LL}^{dM}$  for each topology bin can be found using the constant fit values. The constant fit to the measured UE  $A_{LL}^{dM}$  for bin A =  $-0.0013 \pm 0.0017$ , bin B =  $0.0013 \pm 0.001$ , bin C =  $-0.0031 \pm 0.0021$  and bin D =  $0.0029 \pm 0.0015$ . Within the present statistics, the  $A_{LL}^{dM}$  for all of the topologies is considered to be consistent with zero and independent of the dijet  $M_{inv}$ .

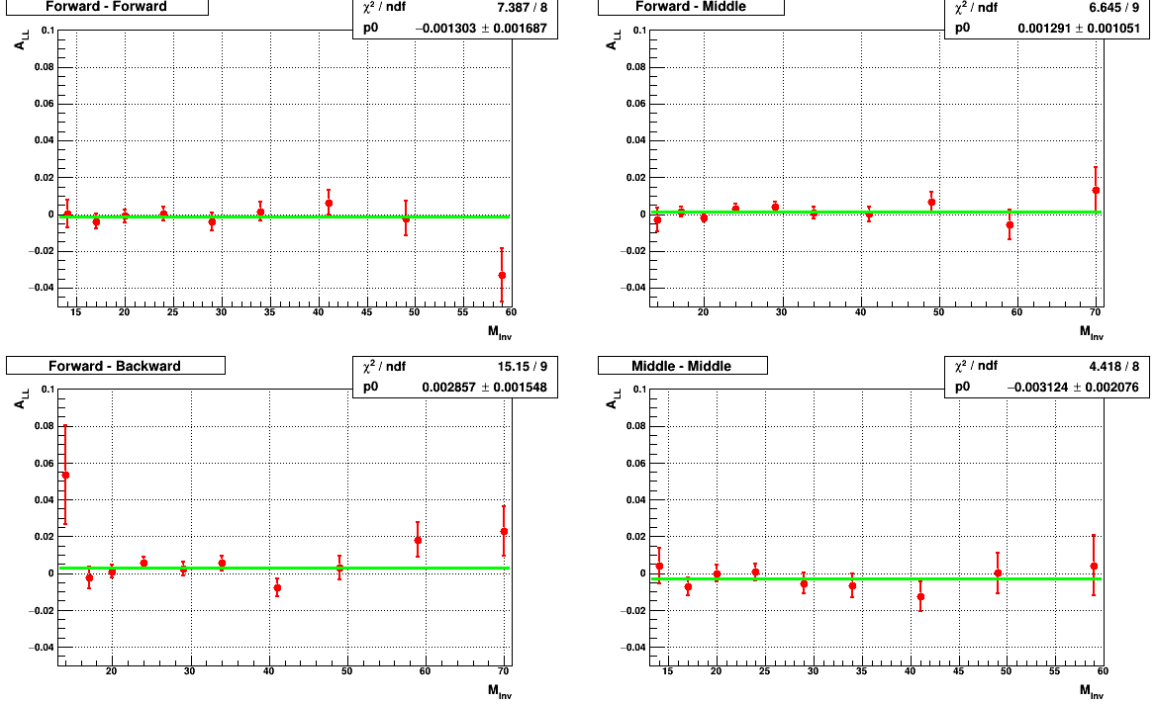


Figure 7.1:  $A_{LL}$  from UE -  $A_{LL}$  from UE for the four topologies.

To estimate the systematic contribution that the UE makes to the dijet  $A_{LL}$  values, the change in the cross section that would occur if the effective boundaries of the dijet  $M_{inv}$  bins shift in a spin-dependent manner are calculated, using the equation:

$$\delta A_{LL} = \frac{\int_{M_{min} - \langle dM \rangle}^{M_{max} + \langle dM \rangle} A_{LL}^{dM} \frac{d\sigma}{dM} dM - \int_{M_{min} + \langle dM \rangle}^{M_{max} + \langle dM \rangle} A_{LL}^{dM} \frac{d\sigma}{dM} dM}{\int_{M_{min} - \langle dM \rangle}^{M_{max} + \langle dM \rangle} A_{LL}^{dM} \frac{d\sigma}{dM} dM + \int_{M_{min} + \langle dM \rangle}^{M_{max} + \langle dM \rangle} A_{LL}^{dM} \frac{d\sigma}{dM} dM} \quad (7.6)$$

where  $d\sigma/dM$  is the unpolarized cross-section and  $\langle dM \rangle$  is the average spin independent underlying event correction. The integral is calculated using the p0 or error (whichever is higher in magnitude) on the constant fit to the measured UE  $A_{LL}^{dM}$  for each invariant mass bin. Since there is no evidence for  $M_{inv}$  dependence, this error is correlated across all the invariant mass bins and therefore it is combined with the relative luminosity systematic error. The corresponding systematic uncertainties are included in Table 7.2.

## 7.2 Dilution due to Vertex Finding

Comparison of the reconstructed primary vertex in data to the vertex thrown at the beginning of the simulation shows excellent agreement. This indicates that there is very minimal distortion in  $A_{LL}$  due to the vertex finding algorithm. Hence the dilution due to vertex finding is considered negligible.

## 7.3 Residual Transverse $A_{LL}$ Uncertainty

Since the longitudinally polarized proton beams are not always perfectly polarized along the z-direction, the measured asymmetry has contributions from the longitudinal double spin asymmetry and from the residual transverse asymmetry. The local transverse asymmetry measured by the ZDC is used to find the transverse component. The local transverse asymmetry for the yellow and blue beams changed from 5.5% and 5% during the beginning of the run to 0.3% each after the spin rotators were turned on. For pp collisions at 200 GeV, the residual transverse asymmetry was found to be less than 0.008 for jet  $p_T < 15$  GeV, implying that it would be less than 0.008 for  $M_{inv}$  of  $\sim 70\text{GeV}$  ( $x_T = 2 p_T/\sqrt{s}$ ). The contribution from the residual transverse component calculated from these would be negligible compared to other systematic uncertainties for the 2012 data.

## 7.4 Non-Collision Background Uncertainty

The data from the abort gaps was used in comparison with the data from the normal bunch crossings, in order to estimate the fraction of non-collision background contributions to the real jet signals. The 2012 inclusive jet analysis [36] found the jet yield to be suppressed by a factor of 1000 in the abort gaps, putting an upper bound on the possible non-collision background. The systematic effect on the inclusive analysis was found to be negligible. The suppression for dijet yields should be as much or

more. Therefore systematic effects due to non-collision backgrounds are considered negligible.

## 7.5 Jet Energy Scale Uncertainties

The systematic uncertainty on the reconstructed dijet  $M_{Inv}$  is primarily due to the jet energy scale uncertainty. The discrepancies between the embedding and the data for the TPC track reconstruction efficiency,  $\delta M_{inv,track-loss}$ , is calculated by removing 7% of the tracks from each event and running the jet finding algorithm again. Comparing the jets with tracks removed to jets with no tracks removed gives a conservative estimate on effect of any efficiency mis-matches between the embedding and the data. To account for any differences in TPC efficiency, a systematic uncertainty is included which is calculated as difference in the shifts using both tracking efficiencies. The second contribution,  $\delta M_{inv,stat.}$ , is the statistical uncertainty calculated for each detector bin.

The energy deposited in the BEMC has its uncertainties, which in turn contributes to the jet  $p_T$  and thus the dijet  $M_{inv}$  measured in this analysis. Both charged tracks and neutral particles deposit energy in the towers, and therefore the systematic uncertainty has contributions from both the neutral energy uncertainty and the track uncertainty. The error due to the BEMC can be calculated from two contributions - the uncertainty on the efficiency set to 1%, and the uncertainty on the gain calibration to be a conservative value of 3.8%. Using these, and the neutral fraction of energy in the jet ( $R_t$ ) (averaged for both the jets in the dijet pair) measured by BEMC, the error in the dijet  $M_{inv}$  due the BEMC is

$$\delta M_{inv,BEMC} = \langle M_{inv} \rangle \times R_t \times \sqrt{\delta_{gain}^2 + \delta_{eff}^2} \quad (7.7)$$

The systematic error due to the track uncertainty is from the charged portion of the jets:  $(1-R_t)$ . The systematics due to the uncertainty in the track momentum is set



at 1%, calculated simply as  $\delta M_{inv,tracks} = \langle M_{inv} \rangle \times (1 - R_t) \times 0.01$ . There is another contribution that encapsulates how well the simulation emulates hadronic interactions from charged hadrons and the neutral particles in the towers. The systematic error associated with how well the hadronic effects are emulated, was determined to be 0.09 from the analysis in Ref. [41]. Multiplying this by the charged hadronic portion of the jet  $M_{inv}$  and applying the appropriate scaling parameters gives the error in the jet energy scale due to charged tracks in the BEMC:

$$\delta M_{inv,BEMCtracks} = \langle M_{inv} \rangle (1 - R_t) \delta f_{E_{had}} \left\{ \frac{f_{E_{dep}} (S_{neutral} - \epsilon_{track} f_{track_{dep}})}{\epsilon_{track}} \right\} \quad (7.8)$$

The charged component is the product  $\langle M_{inv} \rangle (1 - R_t)$ . The inefficiency of the TPC detection of these tracks is accounted for, by dividing by the efficiency of the TPC ( $\epsilon_{track}$ ) which is set to  $\epsilon_{track} = 65\%$ . The average fraction of hadronic energy deposited in the BEMC is ( $f_{E_{dep}} = 0.3$ ). The neutral hadrons which are not detected by the TPC, but deposit energy in the BEMC, are accounted for - as the neutral hadron scale-up,  $S_{neutral}$ , and is set to  $1/0.86 = 1.163$  [41].  $S_{neutral}$  is offset by the fraction of energy deposited by hadrons into a single isolated tower,  $f_{track_{dep}} = 0.5$ , which is a conservative value since we use the 100% energy subtraction scheme for BEMC towers in our jet finding algorithm. Therefore, the appropriate factor is  $(S_{neutral} - f_{track_{dep}} \epsilon_{track})$ , where the  $\epsilon_{track}$  factor offsets the value in the denominator of Equation 7.8.

The total track uncertainty is then obtained by adding these results added in quadrature:

$$\delta M_{inv,tracks} = \sqrt{\delta M_{inv,tracks}^2 + \delta M_{inv,BEMCtracks}^2} \quad (7.9)$$

The final result for the jet energy scale is  $\delta M_{inv,tracks}$  and  $\delta M_{inv,BEMC}$  added in quadrature. For the dijet  $M_{inv}$  shift error, this is all we need, and the result may be

calculated by following Equation 7.10.

$$\delta M_{inv,true} = \sqrt{\delta M_{inv,track-loss}^2 + \delta M_{inv,stat.}^2 + M_{inv,BEMC}^2 + \delta M_{inv,tracks}^2} \quad (7.10)$$

Changing the parameters of the Perugia 2012 PYTHIA tune can cause a shift in the average dijet  $M_{inv}$ . The uncertainties due to PYTHIA tune parameters is estimated by using the different variants provided for Perugia 2012 in the PYTHIA version of 6.4.28 and recalculating the corrections.

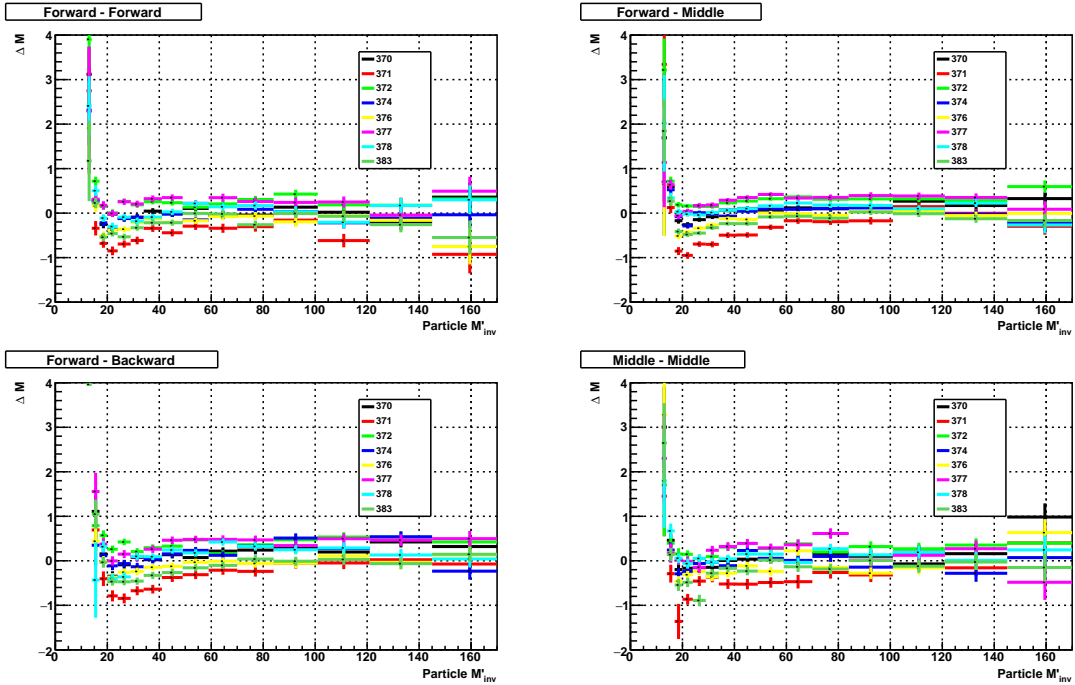


Figure 7.2:  $\Delta M$  for various tunes - Average  $M_{inv}$  shift using the different tunes for the four topologies.

The alternative tunes selected include the choice of  $\alpha_s(p/2)$  for higher (tune 371) and  $\alpha_s(2p)$  for lower (tune 372) initial + final state radiation, the modification to less color re-connections (tune 374), the increase in either longitudinal (376) or transverse (377) fragmentations, a switch to MSTW 2008 LO PDFs rather than CTEQ6L1 LO PDFs (378), and a set of Innsbruck hadronization parameters (383). The dijet  $M_{inv}$  shifts are studied for these variants, and their differences to the default tune are

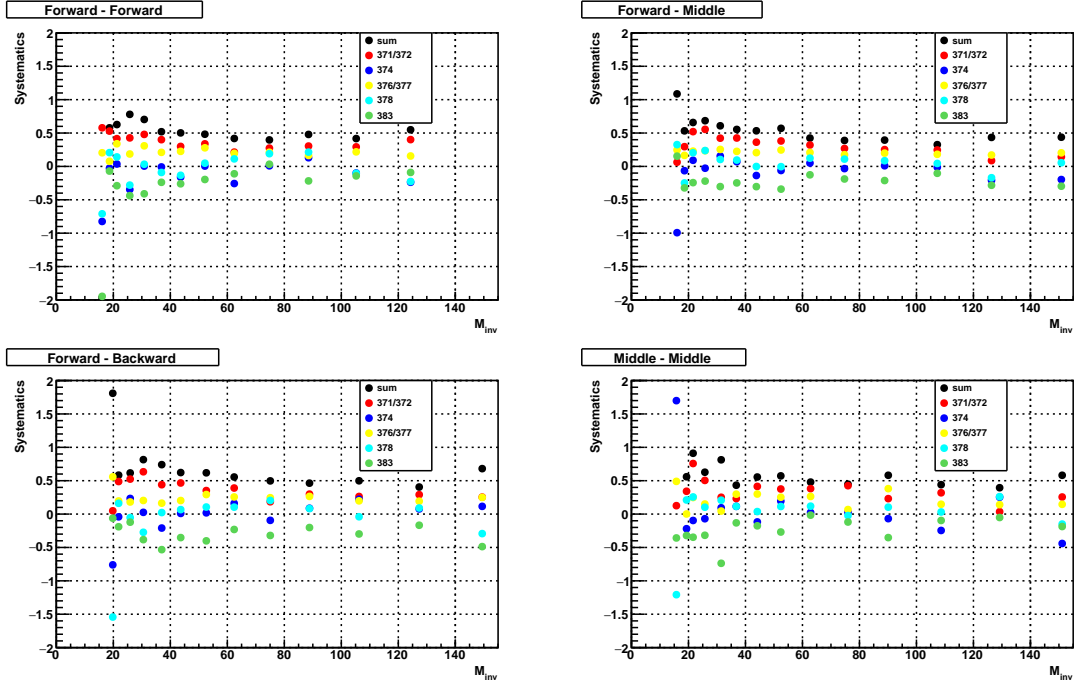


Figure 7.3: **Systematic Uncertainties** - Systematics using the different tunes and the final quadrature sum (black) for the four topologies.

calculated. Both particle and parton jets are reconstructed from the various tunes by using the same algorithm as used in the  $A_{LL}$  analysis. The particle jets are then matched to the parton jets, and the average shifts in  $M_{inv}$  are calculated in each bin. This procedure is repeated for all of the four topologies.

To calculate the corrections for alternative tune pairs (371,372) and (376,377), which relate to initial+final state radiation and fragmentation respectively, half of the absolute difference of the pair is taken as its contribution to the tune systematic uncertainty. Together with the difference in scale shift from the remaining tunes, they are added in quadrature to construct the total PYTHIA tune systematic error. Figure 7.2 shows the average  $M_{inv}$  shift using the various tunes and Figure 7.3 shows the systematic uncertainties due to the different tunes, and the quadrature sum (black).

The spin-independent UE systematic uncertainty on jet energy is measured as the difference between the UE contribution to the dijet  $M_{inv}$  between data and simulation. Figure 7.4 shows the average UE contribution in data and simulation for each of the

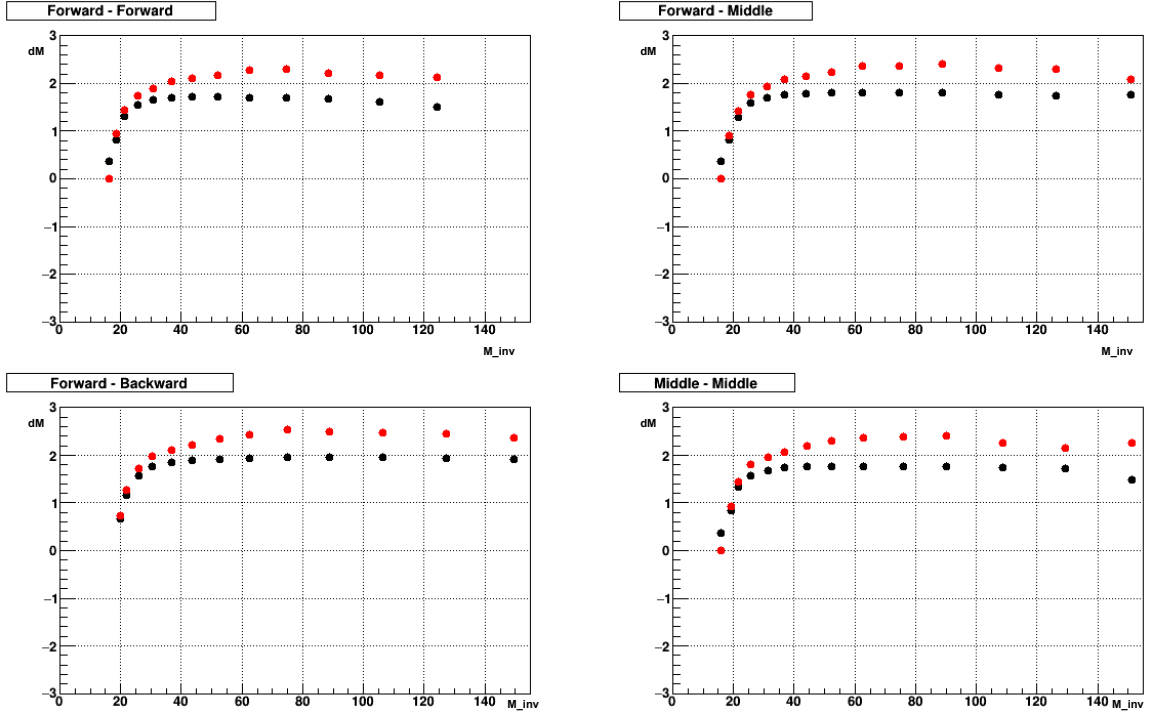


Figure 7.4: **UE contribution in data and simulation** - The average UE contribution in data (black) and simulation (red) for the four topologies.

four topologies, in bins of dijet  $M_{inv}$ .

Table 7.1 lists the corrections and systematic uncertainties for each dijet  $M_{inv}$  bin at the detector -level, for the four topologies.

## 7.6 Trigger and Reconstruction Bias Errors

As explained in the previous chapter, after calculating the mean of the 100 differences in detector and parton  $A_{LL}$  as the "model correction", the standard deviation of these 100 differences is denoted as the "model error". In addition to that, the statistical uncertainty on the detector level  $A_{LL}$  from the NNPDF best fit, denoted as the "statistical error" is also calculated. A quadrature sum of the model error and statistical error gives the total trigger and reconstruction bias error. The values of these errors are detailed in the table 7.2.

Table 7.1: The corrections and systematic uncertainties assigning parton dijet  $M_{inv}$  to the detector-level dijet  $M_{Inv}$  bins for the four topologies.  $\delta M_{inv} = \langle M_{inv,parton} - M_{inv,detector} \rangle$ . All values are in  $\text{GeV}/c^2$ .

Detector dijet			$\delta M_{Inv}$	Hadron resp.	EM resp.	UE syst.	Tune syst.	Parton dijet
Bin	$M_{Inv}$	$\langle M_{Inv} \rangle$						$M_{Inv}$
Topology A: Forward-Forward Dijets								
A1	14 – 17	15.88	$2.77 \pm 0.24$	0.51	0.30	0.14	0.578	$18.65 \pm 0.87$
A2	17 – 20	18.48	$2.76 \pm 0.21$	0.67	0.34	0.14	0.627	$21.24 \pm 1.02$
A3	20 – 24	21.90	$3.87 \pm 0.14$	0.70	0.40	0.20	0.780	$25.77 \pm 1.15$
A4	24 – 29	26.33	$4.51 \pm 0.18$	0.93	0.49	0.25	0.703	$30.84 \pm 1.30$
A5	29 – 34	31.34	$5.53 \pm 0.16$	1.04	0.60	0.34	0.519	$36.87 \pm 1.36$
A6	34 – 41	37.17	$6.44 \pm 0.16$	1.34	0.71	0.39	0.502	$43.61 \pm 1.65$
A7	41 – 49	44.54	$7.58 \pm 0.19$	1.27	0.82	0.46	0.482	$52.12 \pm 1.66$
A8	49 – 59	53.23	$9.21 \pm 0.24$	1.68	0.94	0.58	0.418	$62.44 \pm 2.07$
A9	59 – 70	63.58	$11.18 \pm 0.33$	2.19	1.09	0.60	0.397	$74.76 \pm 2.56$
Topology B: Forward-Middle Dijets								
B1	14 – 17	16.02	$2.58 \pm 0.22$	0.38	0.31	0.08	0.53	$18.60 \pm 0.54$
B2	17 – 20	18.51	$3.09 \pm 0.14$	0.59	0.35	0.12	0.66	$21.60 \pm 0.71$
B3	20 – 24	21.92	$3.92 \pm 0.11$	0.93	0.41	0.19	0.69	$25.84 \pm 1.03$
B4	24 – 29	26.34	$4.81 \pm 0.10$	0.90	0.49	0.25	0.61	$31.15 \pm 1.06$
B5	29 – 34	31.35	$5.60 \pm 0.11$	1.02	0.60	0.33	0.55	$36.95 \pm 1.24$
B6	34 – 41	37.20	$6.62 \pm 0.11$	1.22	0.72	0.37	0.53	$43.82 \pm 1.47$
B7	41 – 49	44.57	$7.91 \pm 0.13$	1.56	0.85	0.45	0.57	$52.48 \pm 1.83$
B8	49 – 59	53.30	$9.33 \pm 0.16$	1.76	0.98	0.56	0.42	$62.63 \pm 2.09$
B9	59 – 70	63.67	$11.08 \pm 0.22$	2.12	1.12	0.57	0.39	$74.75 \pm 2.48$
B10	70 – 84	75.66	$13.17 \pm 0.27$	2.41	1.30	0.62	0.39	$88.83 \pm 2.82$
Topology C: Middle-Middle Dijets								
C1	14 – 17	15.89	$3.43 \pm 0.31$	0.47	0.32	0.08	0.56	$19.32 \pm 0.86$
C2	17 – 20	18.48	$3.14 \pm 0.22$	0.64	0.36	0.12	0.91	$21.62 \pm 1.19$
C3	20 – 24	21.91	$3.84 \pm 0.20$	0.84	0.41	0.23	0.63	$25.75 \pm 1.17$
C4	24 – 29	26.34	$5.14 \pm 0.17$	0.90	0.50	0.27	0.81	$31.48 \pm 1.35$
C5	29 – 34	31.35	$5.42 \pm 0.21$	1.26	0.62	0.33	0.43	$36.77 \pm 1.52$
C6	34 – 41	37.20	$6.95 \pm 0.19$	1.21	0.74	0.43	0.56	$44.15 \pm 1.59$
C7	41 – 49	44.57	$7.83 \pm 0.23$	1.42	0.86	0.54	0.57	$52.40 \pm 1.85$
C8	49 – 59	53.31	$9.54 \pm 0.30$	1.80	0.99	0.60	0.48	$62.85 \pm 2.21$
C9	59 – 70	63.65	$12.32 \pm 0.36$	2.33	1.14	0.62	0.45	$75.97 \pm 2.72$
Topology D: Forward-Backward Dijets								
D1	14 – 17	16.34	$3.46 \pm 0.51$	1.00	0.32	0.06	1.81	$19.80 \pm 2.15$
D2	17 – 20	18.67	$3.18 \pm 0.29$	0.78	0.36	0.10	0.58	$21.85 \pm 1.08$
D3	20 – 24	21.96	$3.95 \pm 0.21$	0.67	0.40	0.14	0.62	$25.91 \pm 1.03$
D4	24 – 29	26.36	$4.17 \pm 0.37$	0.74	0.48	0.21	0.82	$30.53 \pm 1.27$
D5	29 – 34	31.36	$5.62 \pm 0.26$	1.05	0.58	0.26	0.74	$36.98 \pm 1.46$
D6	34 – 41	37.23	$6.41 \pm 0.20$	1.20	0.71	0.32	0.62	$43.64 \pm 1.57$
D7	41 – 49	44.64	$7.98 \pm 0.22$	1.47	0.84	0.43	0.62	$52.62 \pm 1.86$
D8	49 – 59	53.39	$9.01 \pm 0.26$	1.86	0.97	0.51	0.56	$62.40 \pm 2.25$
D9	59 – 70	63.72	$11.35 \pm 0.33$	2.10	1.12	0.59	0.50	$75.07 \pm 2.52$
D10	70 – 84	75.76	$13.07 \pm 0.42$	2.37	1.29	0.55	0.46	$88.83 \pm 2.82$

Table 7.2: The corrections and systematic uncertainties in  $A_{LL}$  for dijet production. In addition to the uncertainties enumerated here, there are two that are common to all the points, a shift uncertainty of  $\pm 0.00022$  associated with the relative luminosity measurement and a scale uncertainty of  $\pm 6.5\%$  associated with the beam polarization.

Bin	Dijet $M_{inv}$ (GeV/ $c^2$ )	UE syst.	Trigger and Reconstruction Bias			
			Model Correction	Model Error	Stat. Error	Total Error
Topology A: Forward-Forward Dijets						
A1	18.65	-0.00003	0.00004	0.00022	0.00019	0.0003
A2	21.24	0.00013	-0.00025	0.00041	0.00026	0.0005
A3	25.77	0.00014	0.00080	0.00028	0.00006	0.0003
A4	30.84	0.00013	0.00088	0.00031	0.00002	0.0003
A5	36.87	0.00011	0.00143	0.00042	0.00004	0.0004
A6	43.61	0.00010	0.00124	0.00055	0.00004	0.0005
A7	52.12	0.00009	0.00303	0.00088	0.00004	0.0009
A8	62.44	0.00007	0.00144	0.00122	0.00017	0.0012
A9	74.76	0.00007	0.00318	0.00187	0.00021	0.0019
Topology B: Forward-Middle Dijets						
B1	18.60	-0.00013	0.00041	0.00017	0.00007	0.0002
B2	21.60	0.00023	0.00058	0.00018	0.00009	0.0002
B3	25.84	0.00013	0.00086	0.00029	0.00003	0.0003
B4	31.15	0.00014	0.00112	0.00032	0.00001	0.0003
B5	36.95	0.00011	-0.00065	0.00167	0.00082	0.0019
B6	43.82	0.00011	0.00195	0.00061	0.00004	0.0006
B7	52.48	0.00008	0.00134	0.00069	0.00004	0.0007
B8	62.63	0.00008	0.00153	0.00103	0.00015	0.0010
B9	74.75	0.00006	0.00261	0.00134	0.00007	0.0013
B10	88.83	0.00005	0.00389	0.00188	0.00005	0.0019
Topology C: Middle-Middle Dijets						
C1	19.32	-0.00003	0.00017	0.00017	0.00008	0.0002
C2	21.62	0.00012	0.00001	0.00114	0.00016	0.0011
C3	25.75	0.00014	0.00094	0.00037	0.00003	0.0004
C4	31.48	0.00015	-0.00079	0.00051	0.00057	0.0008
C5	36.77	0.00015	0.00108	0.00059	0.00006	0.0006
C6	44.15	0.00009	0.00223	0.00075	0.00005	0.0008
C7	52.40	0.00009	0.00228	0.00115	0.00010	0.0012
C8	62.85	0.00007	0.00122	0.00149	0.00015	0.0015
C9	75.97	0.00007	-0.00008	0.00185	0.00023	0.0019
Topology D: Forward-Backward Dijets						
D1	19.80	-0.00034	0.00058	0.00021	0.00005	0.0002
D2	21.85	-0.00001	-0.00019	0.00088	0.00033	0.0009
D3	25.91	0.00018	0.00097	0.00031	0.00007	0.0003
D4	30.53	0.00012	0.00011	0.00023	0.00034	0.0004
D5	36.98	0.00013	-0.00010	0.00023	0.00044	0.0005
D6	43.64	0.00010	-0.00146	0.00086	0.00037	0.0009
D7	52.62	0.00010	0.00119	0.00065	0.00004	0.0006
D8	62.40	0.00007	0.00198	0.00090	0.00008	0.0009
D9	75.07	0.00007	0.00376	0.00208	0.00011	0.0021
D10	88.83	0.00007	0.00430	0.00150	0.00008	0.0015

## Chapter 8 Results and Conclusions

This thesis presents the dijet  $A_{LL}$  results from the 2012 RHIC run at  $\sqrt{s} = 510$  GeV as a function of the parton level dijet  $M_{inv}$  in four different topologies defined using three defined detector regions of the STAR detector. The statistical and systematic uncertainties are tabulated in Table 8.1. Topological bins A-D correspond to forward-forward, forward-middle, middle-middle and forward-backward configurations for the jets in the dijet pair. Figures 8.2, 8.4, 8.8 and 8.6 show the dijet  $A_{LL}$  as a function of the fully corrected parton-level  $M_{inv}$  for the four different topological bins. The statistical errors are shown in black while the vertical and horizontal widths of the red boxes represent the systematic uncertainties on the asymmetries and the  $M_{inv}$  respectively. In addition, the correlated errors which include the underlying event systematic uncertainty on  $A_{LL}$  combined with the relative luminosity systematic, are plotted as a red shaded band on the horizontal axis.

The dijet asymmetries are also compared to the theoretical predictions DSSV14 [5] (blue) and NNPDFpol1.1 [6] (green). The yellow and green hatched bands represent the scale and PDF systematic uncertainties for the NNPDFpol1.1 curves. These PDFs are input into a pQCD NLO code that then produces these curves. While in general the data shows very good agreement with the theoretical predictions, there is some sign of a significant deviation at low  $M_{inv}$  for Figure 8.2. This is precisely the region where this data provides a unique input - the region of low  $x$  where the 200 GeV data does not have access to. It is possible that this is the first sign of a more significant  $\Delta G$  at lower  $x$ . As seen in Figure 1.6, with the current understanding the error bars are large in the  $x < 0.05$  region that these measurements are done. This first measurement of the dijet  $A_{LL}$  will provide significant constraints in this  $x$  region.

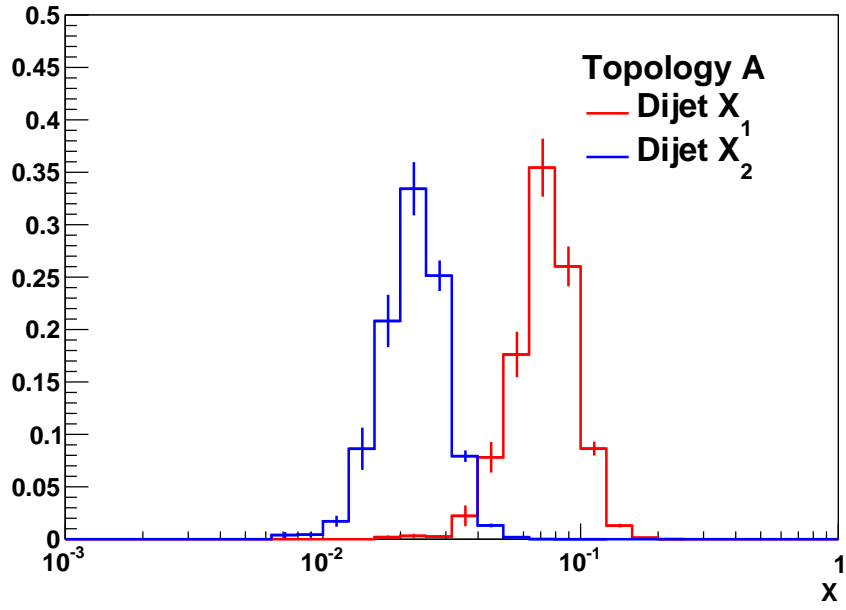


Figure 8.1: **Dijet  $x_1$  and  $x_2$**  - Dijet  $x_1$  and  $x_2$  for Topology A for  $M_{inv}$  17-20 GeV.

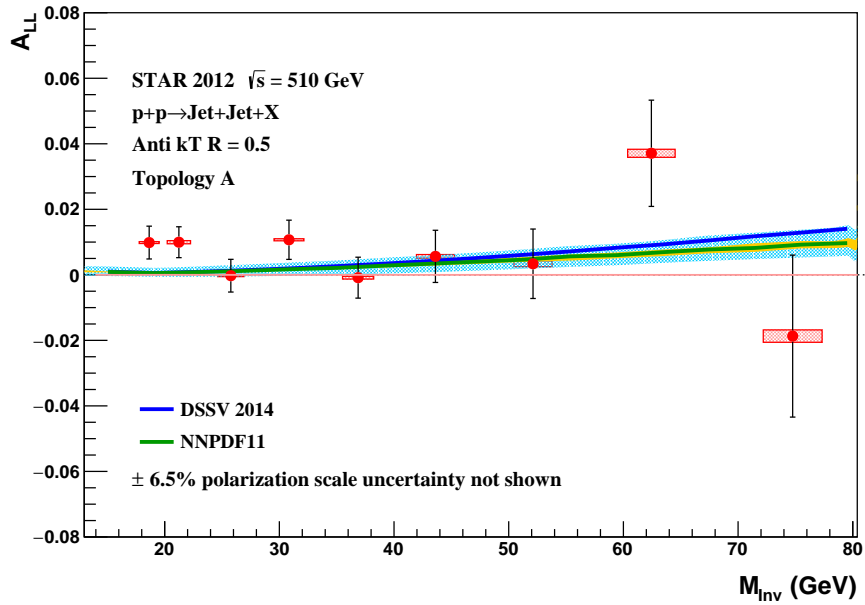


Figure 8.2:  $A_{LL}$  - Dijet  $A_{LL}$  for Topology A.



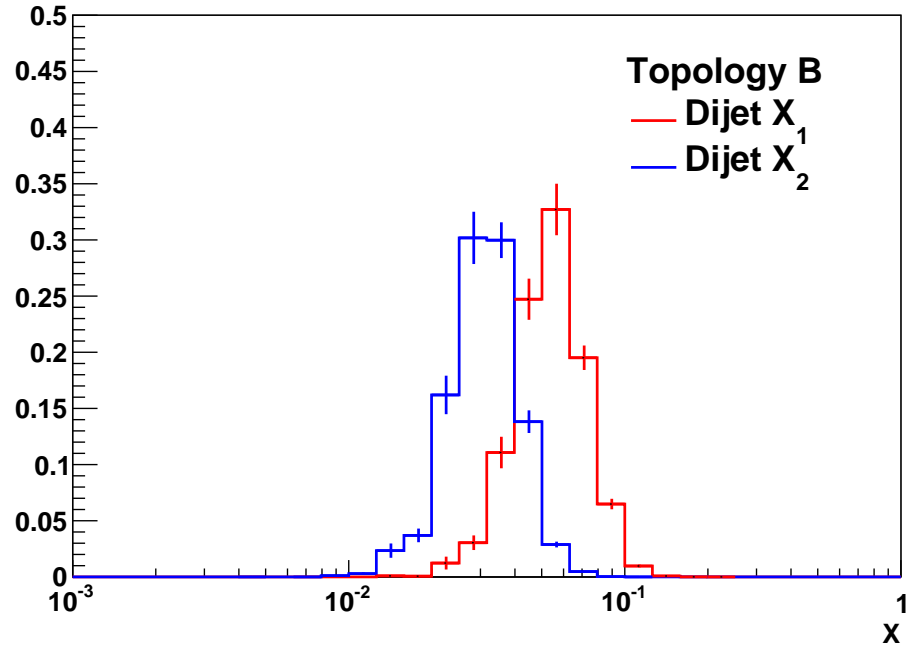


Figure 8.3: **Dijet  $x_1$  and  $x_2$**  - Dijet  $x_1$  and  $x_2$  for Topology B for  $M_{inv}$  17-20 GeV.

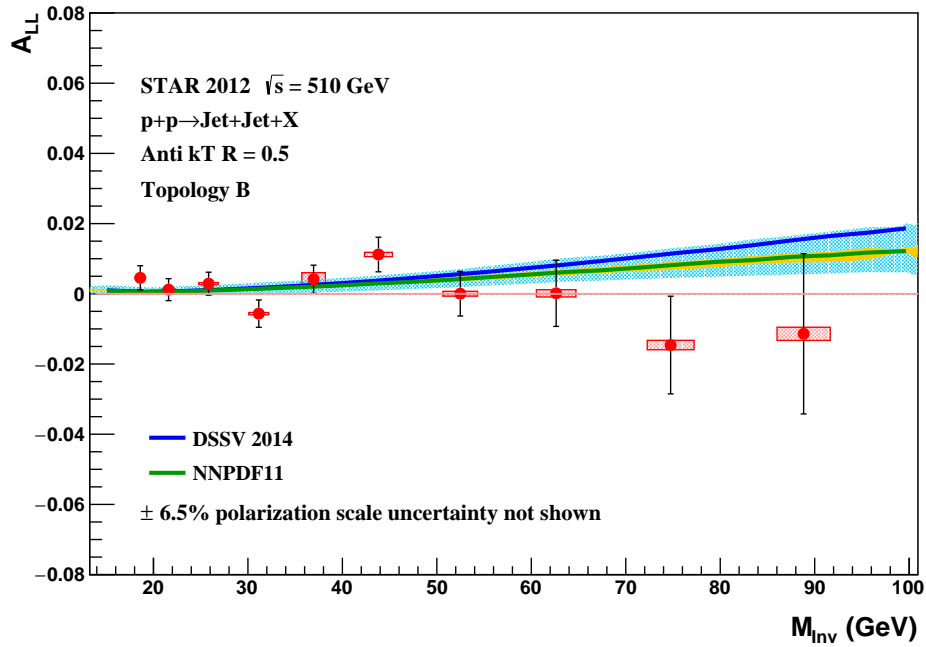


Figure 8.4:  $A_{LL}$  - Dijet  $A_{LL}$  for Topology B.

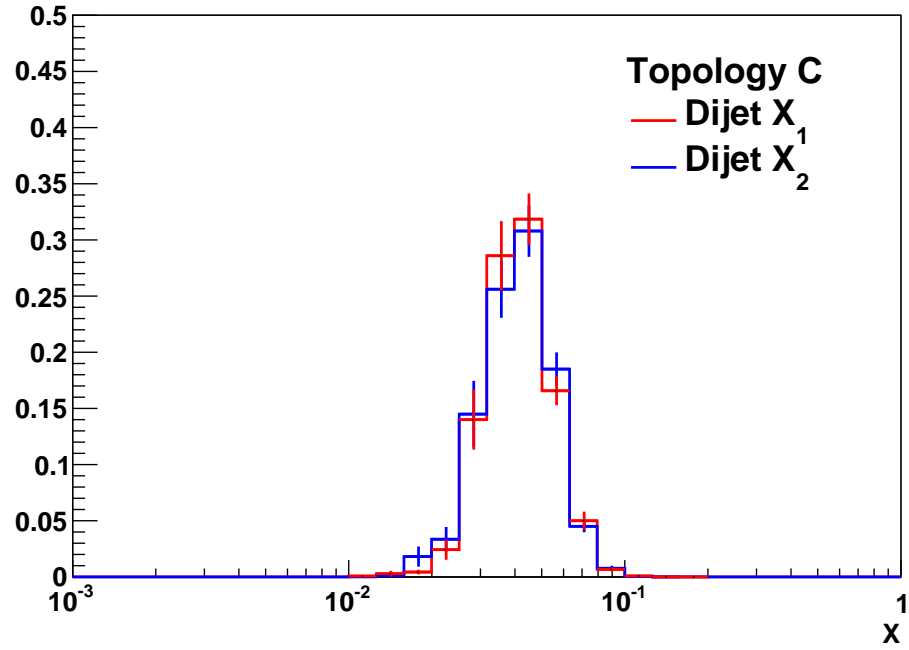


Figure 8.5: **Dijet  $x_1$  and  $x_2$**  - Dijet  $x_1$  and  $x_2$  for Topology C for  $M_{inv}$  17-20 GeV.

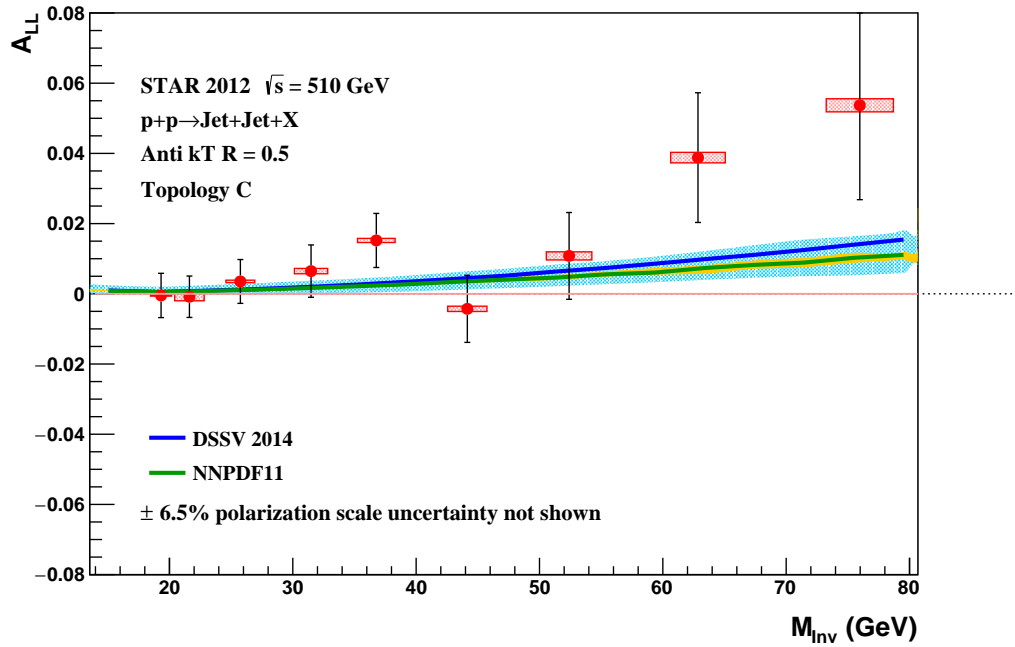


Figure 8.6:  $A_{LL}$  - Dijet  $A_{LL}$  for Topology C.

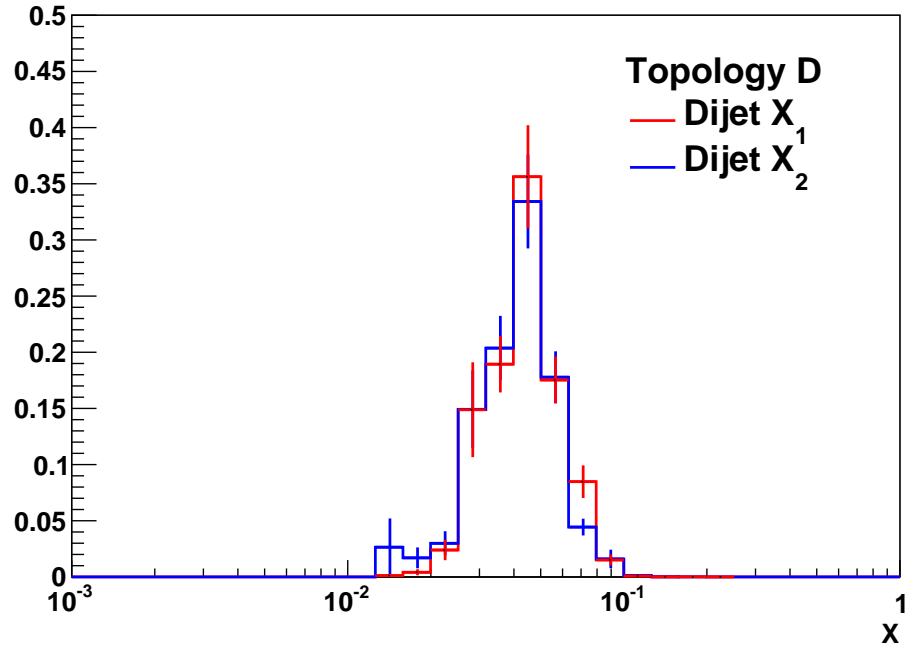


Figure 8.7: **Dijet  $x_1$  and  $x_2$**  - Dijet  $x_1$  and  $x_2$  for Topology D for  $M_{inv}$  17-20 GeV.

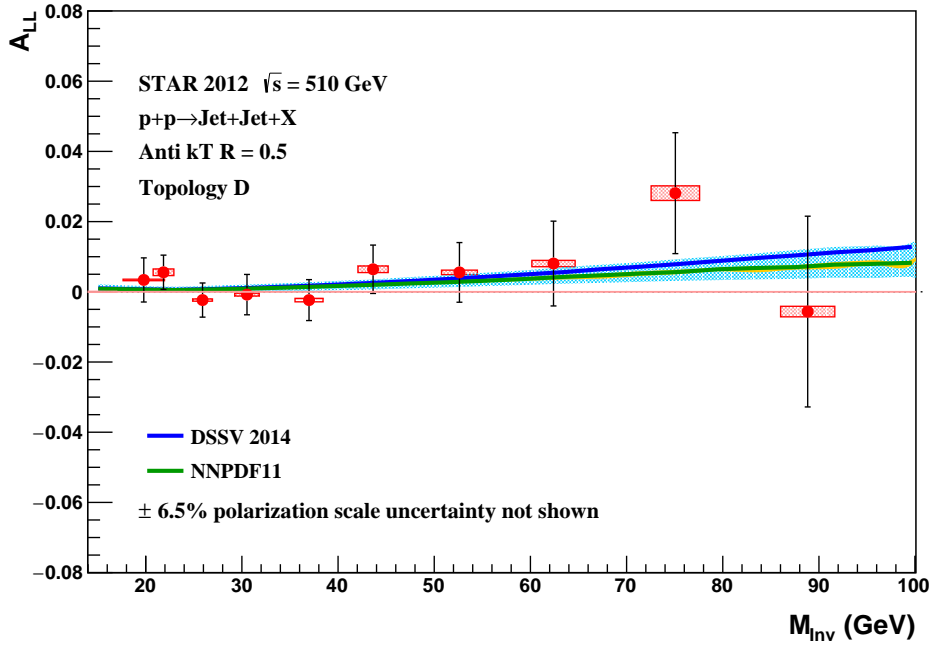


Figure 8.8:  $A_{LL}$  - Dijet  $A_{LL}$  for Topology D.

Reconstructing dijets permit the full reconstruction of the the initial  $x_1$  and  $x_2$  at leading order. Figures 8.1, 8.3, 8.5 and 8.7 show the leading order extractions of the  $x_1$  (blue) and  $x_2$  (red) distributions from the simulation sample for a single dijet bin  $M_{inv} = 17\text{-}20 \text{ GeV}/c^2$ . The asymmetry between  $x_1$  and  $x_2$  is largest for topological bin A and decreases until they are identical in topological bins C and D. As mentioned earlier, topologies A and C accesses collisions where  $\cos(\theta^*)$  is close to zero, while topologies B and D accesses collisions with larger values of  $\cos(\theta^*)$ .

The results from these  $A_{LL}$  measurements are sensitive to the gluon polarization in the momentum range  $x \sim 0.015$  to  $\sim 0.2$ . The results will provide important constraints on both the magnitude and the shape of  $\Delta g(x)$  when they are included in future global analyses of the polarized PDFs, especially in the region  $x < 0.05$  that has been unconstrained in previous global analyses.

Table 8.1:  $A_{LL}$  as a function of parton dijet  $M_{Inv}$  (in  $\text{GeV}/c^2$ ) in  $\sqrt{s} = 510$  GeV  $pp$  collisions. There is an additional  $\pm 6.5\%$  scale uncertainty from the beam polarization that is common to all the measurements.

Bin	Dijet $M_{Inv}$	$A_{LL} \pm \text{stat.} \pm \text{syst.}$	UE/RL syst.
Topology A: Forward-Forward Dijets			
A1	$18.65 \pm 0.87$	$0.0099 \pm 0.0050 \pm 0.0003$	0.0002
A2	$21.24 \pm 1.02$	$0.0010 \pm 0.0047 \pm 0.0004$	0.0003
A3	$25.77 \pm 1.15$	$-0.0003 \pm 0.0050 \pm 0.0003$	0.0003
A4	$30.84 \pm 1.30$	$0.0107 \pm 0.0060 \pm 0.0003$	0.0003
A5	$36.87 \pm 1.36$	$-0.0009 \pm 0.0062 \pm 0.0004$	0.0003
A6	$43.61 \pm 1.65$	$0.0056 \pm 0.0080 \pm 0.0006$	0.0002
A7	$52.12 \pm 1.66$	$0.0034 \pm 0.0106 \pm 0.0009$	0.0002
A8	$62.44 \pm 2.07$	$0.0371 \pm 0.0162 \pm 0.0012$	0.0002
A9	$74.76 \pm 2.56$	$-0.0187 \pm 0.0247 \pm 0.0019$	0.0002
Topology B: Forward-Middle Dijets			
B1	$18.6 \pm 0.54$	$0.0046 \pm 0.0035 \pm 0.0002$	0.0003
B2	$21.6 \pm 0.71$	$0.0012 \pm 0.0031 \pm 0.0002$	0.0003
B3	$25.84 \pm 1.03$	$0.0029 \pm 0.0033 \pm 0.0003$	0.0003
B4	$31.15 \pm 1.06$	$-0.0057 \pm 0.0039 \pm 0.0003$	0.0003
B5	$36.95 \pm 1.24$	$0.0042 \pm 0.0040 \pm 0.0019$	0.0003
B6	$43.82 \pm 1.48$	$0.0112 \pm 0.0049 \pm 0.0006$	0.0003
B7	$52.48 \pm 1.83$	$0.0003 \pm 0.0063 \pm 0.0007$	0.0002
B8	$62.63 \pm 2.09$	$0.0014 \pm 0.0094 \pm 0.0010$	0.0002
B9	$74.75 \pm 2.48$	$-0.0146 \pm 0.0139 \pm 0.0013$	0.0002
B10	$88.83 \pm 2.82$	$-0.0114 \pm 0.0228 \pm 0.0019$	0.0002
Topology C: Middle-Middle Dijets			
C1	$19.32 \pm 0.86$	$-0.0005 \pm 0.0063 \pm 0.0002$	0.0002
C2	$21.62 \pm 1.19$	$-0.0008 \pm 0.0059 \pm 0.0012$	0.0003
C3	$25.75 \pm 1.17$	$0.0035 \pm 0.0062 \pm 0.0004$	0.0003
C4	$31.48 \pm 1.35$	$0.0065 \pm 0.0075 \pm 0.0008$	0.0003
C5	$36.77 \pm 1.52$	$0.0152 \pm 0.0077 \pm 0.0006$	0.0003
C6	$44.15 \pm 1.59$	$-0.0043 \pm 0.0096 \pm 0.0008$	0.0002
C7	$52.4 \pm 1.85$	$0.0108 \pm 0.0124 \pm 0.0012$	0.0002
C8	$62.85 \pm 2.21$	$0.0388 \pm 0.0185 \pm 0.0015$	0.0002
C9	$75.97 \pm 2.72$	$0.0537 \pm 0.0269 \pm 0.0019$	0.0002
Topology D: Forward-Backward Dijets			
D1	$19.8 \pm 2.15$	$0.0034 \pm 0.0063 \pm 0.0002$	0.0004
D2	$21.85 \pm 1.08$	$0.0056 \pm 0.0049 \pm 0.0009$	0.0002
D3	$25.91 \pm 1.03$	$-0.0024 \pm 0.0049 \pm 0.0003$	0.0003
D4	$30.53 \pm 1.27$	$-0.0008 \pm 0.0057 \pm 0.0004$	0.0003
D5	$36.98 \pm 1.46$	$-0.0024 \pm 0.0058 \pm 0.0005$	0.0003
D6	$43.64 \pm 1.57$	$0.0064 \pm 0.0069 \pm 0.0009$	0.0002
D7	$52.62 \pm 1.86$	$0.0055 \pm 0.0085 \pm 0.0007$	0.0002
D8	$62.4 \pm 2.25$	$0.0081 \pm 0.0121 \pm 0.0009$	0.0002
D9	$75.07 \pm 2.52$	$0.0281 \pm 0.0172 \pm 0.0021$	0.0002
D10	$88.83 \pm 2.82$	$-0.0056 \pm 0.0272 \pm 0.0015$	0.0002

## Appendix : List of Runs

13077066 13077067 13077068 13077069 13077070 13077073 13077076 13077078  
13077081 13078001 13078002 13078003 13078004 13078006 13078007 13078009 13078011  
13078012 13078014 13078028 13078035 13078036 13078037 13078039 13078040 13078042  
13078043 13078045 13078050 13078051 13078052 13078054 13078055 13078057 13078058  
13078063 13078070 13079032 13079033 13079034 13079035 13079036 13079037 13079038  
13079073 13079074 13079075 13079076 13079077 13079079 13080001 13080002 13080003  
13080004 13080005 13080010 13080011 13080013 13080015 13080090 13080091 13080092  
13080093 13080094 13080095 13080096 13080097 13080098 13080099 13081001 13081004  
13081005 13081007 13081020 13082001 13082002 13082003 13082004 13082005 13082006  
13082007 13082008 13082009 13082010 13082011 13083067 13083068 13083069 13083070  
13083073 13083074 13083076 13083081 13083082 13083084 13084001 13084007 13084008  
13084023 13084024 13084027 13084028 13084032 13084034 13084035 13084036 13084037  
13084038 13084039 13084040 13084041 13085004 13085005 13085006 13085008 13085009  
13085010 13085011 13085028 13085029 13085030 13085031 13085032 13085033 13085034  
13085035 13085036 13085040 13085041 13085047 13085061 13086002 13086003 13086065  
13086067 13086070 13086071 13086072 13086073 13086078 13086079 13086080 13086081  
13086082 13086083 13086085 13086087 13086088 13087009 13087010 13087011 13087012  
13087013 13087015 13087016 13087025 13089021 13089022 13089023 13089024 13089025  
13089026 13089027 13089028 13090005 13090006 13090007 13090008 13090011 13090012  
13090015 13090016 13090017 13090018 13090019 13090021 13090022 13090023 13090035  
13090037 13090038 13090039 13090040 13090043 13090048 13090049 13091001 13091005  
13091009 13091011 13091012 13091019 13091020 13091023 13091024 13091025 13091027  
13091032 13091033 13091034 13091035 13091036 13091037 13091038 13091041 13091042  
13091043 13091044 13091045 13092005 13092006 13092007 13092008 13092036 13092037  
13092038 13092039 13092040 13092042 13092044 13092045 13092046 13093015 13093017

13093018 13093020 13093023 13093024 13093025 13093029 13093030 13093034 13093035  
13093036 13093037 13093038 13093044 13093045 13093046 13094001 13094003 13094004  
13094005 13094007 13094008 13094009 13094010 13094011 13094013 13094014 13094015  
13094016 13094017 13094018 13094020 13094021 13094045 13094050 13094052 13094053  
13094054 13094081 13094082 13094083 13094089 13094091 13095001 13095002 13095003  
13095004 13095006 13095008 13095009 13095012 13095013 13095014 13095015 13095016  
13095017 13095043 13095049 13096001 13096002 13096003 13096004 13096005 13096006  
13096060 13096061 13096062 13096063 13096064 13096065 13096066 13096069 13096070  
13097001 13097002 13097003 13097004 13097005 13097006 13097007 13097021 13097022  
13097023 13097024 13097026 13097027 13097028 13097029 13097032 13097033 13097034  
13097035 13097036 13097037 13097038 13097039 13100003 13100004 13100005 13100006  
13100008 13100010 13100011 13100012 13100013 13100014 13100015 13100025 13100026  
13100027 13100029 13100030 13100031 13100032 13100033 13100034 13100035 13100037  
13100038 13100040 13100041 13100042 13100051 13100053 13100054 13100055 13100056  
13100057 13100059 13100060 13101001 13101002 13101003 13101004 13101005 13101006  
13101007 13101013 13101015 13101021 13101024 13101026 13101027 13101040 13101041  
13101042 13101043 13101044 13101045 13101046 13101047 13101048 13101049 13101050  
13103003 13103004 13103011 13103013 13103014 13103015 13103016 13103017 13104003  
13104004 13104008 13104011 13104012 13104013 13104014 13104019 13104044 13104054  
13104056 13104057 13104058 13104059 13104060 13104061 13104062 13104063 13105006  
13105007 13105008 13105009 13105010 13105011 13105012 13105014 13105015 13105016  
13105017 13105018 13105022 13105038 13105039 13105040 13105041 13106064 13106069  
13106071 13106072 13106073 13106074 13106075 13106076 13107001 13107002 13107003  
13107015 13107016 13107017 13107019 13107021 13107024 13107025 13107026 13107027  
13107028 13107029 13107030 13107032 13107033 13107034 13107059 13107060 13107062  
13108001 13108008 13108009 13108010 13108011 13108012 13108013 13108016 13108025  
13108026 13108028 13108029 13108031 13108033 13108034 13108040 13108050 13108071

13108072 13108073 13108074 13108079 13109014 13109015 13109016 13109017 13109018  
13109025 13109026 13109027



## Bibliography

- [1] H. Abramowicz *et al.*, “Combination of measurements of inclusive deep inelastic  $e^\pm p$  scattering cross sections and QCD analysis of HERA data,” *Eur. Phys. J.*, vol. C75, no. 12, p. 580, 2015.
- [2] J. Ashman *et al.*, “A Measurement of the Spin Asymmetry and Determination of the Structure Function  $g(1)$  in Deep Inelastic Muon-Proton Scattering,” *Phys. Lett.*, vol. B206, p. 364, 1988. [340(1987)].
- [3] R. L. Jaffe and A. Manohar, “The  $g_1$  problem: Deep inelastic electron scattering and the spin of the proton,” *Nuclear Physics B*, vol. 337, pp. 509–546, 1990.
- [4] J. Ashman *et al.*, “An Investigation of the Spin Structure of the Proton in Deep Inelastic Scattering of Polarized Muons on Polarized Protons,” *Nucl. Phys.*, vol. B328, p. 1, 1989. [351(1989)].
- [5] D. de Florian, R. Sassot, M. Stratmann, and W. Vogelsang, “Evidence for polarization of gluons in the proton,” *Phys. Rev. Lett.*, vol. 113, p. 012001, Jul 2014.
- [6] E. R. Nocera, R. D. Ball, S. Forte, G. Ridolfi, and J. Rojo, “A first unbiased global determination of polarized PDFs and their uncertainties,” *Nucl. Phys.*, vol. B887, pp. 276–308, 2014.
- [7] D. de Florian, R. Sassot, M. Stratmann, and W. Vogelsang, “Extraction of spin-dependent parton densities and their uncertainties,” *Phys. Rev. D*, vol. 80, p. 034030, Aug 2009.
- [8] J. Pumplin, D. R. Stump, J. Huston, H. L. Lai, P. M. Nadolsky, and W. K. Tung, “New generation of parton distributions with uncertainties from global QCD analysis,” *JHEP*, vol. 07, p. 012, 2002.
- [9] A. Mukherjee and W. Vogelsang, “Jet production in (un)polarized  $pp$  collisions: Dependence on jet algorithm,” *Phys. Rev. D*, vol. 86, p. 094009, Nov 2012.
- [10] D. de Florian, R. Sassot, M. Stratmann, and W. Vogelsang, “Global analysis of helicity parton densities and their uncertainties,” *Phys. Rev. Lett.*, vol. 101, p. 072001, Aug 2008.
- [11] D. de Florian, R. Sassot, M. Stratmann, and W. Vogelsang, “Global Analysis of Helicity Parton Densities and Their Uncertainties,” *Phys. Rev. Lett.*, vol. 101, p. 072001, 2008.
- [12] Z. Chang, “Gluon Polarization in Longitudinally Polarized  $pp$  Collisions at STAR,” *Int. J. Mod. Phys. Conf. Ser.*, vol. 40, p. 1660021, 2016.

- [13] L. Adamczyk *et al.*, “Measurement of the cross section and longitudinal double-spin asymmetry for di-jet production in polarized  $pp$  collisions at  $\sqrt{s} = 200$  GeV,” *Phys. Rev.*, vol. D95, no. 7, p. 071103, 2017.
- [14] A. Zelenski, J. Alessi, B. Briscoe, G. Dutto, H. Huang, A. Kponou, S. Kokhanovski, V. Klenov, A. Lehrach, P. Levy, *et al.*, “Optically pumped polarized h-ion source for rhic spin physics,” *Review of scientific instruments*, vol. 73, no. 2, pp. 888–891, 2002.
- [15] M. Bai, “Accelerating Polarized Protons to High Energy,” *Conf. Proc.*, vol. C100523, p. THPPMH01, 2010.
- [16] I. Alekseev *et al.*, *Configuration manual polarized proton collider at RHIC*, 2012.
- [17] A. Zelenski *et al.*, “Absolute polarized H-jet polarimeter development, for RHIC,” *Nucl. Instrum. Meth.*, vol. A536, pp. 248–254, 2005.
- [18] H. Huang *et al.*, “Commissioning of RHIC p carbon CNI polarimeter,” *Nucl. Phys.*, vol. A721, pp. 356–359, 2003. [,795(2000)].
- [19] RHIC Polarimetry Group, “RHIC Polarization for Runs 9 – 15.” Local analysis note, 2016.
- [20] K. H. Ackermann *et al.*, “STAR detector overview,” *Nucl. Instrum. Meth.*, vol. A499, pp. 624–632, 2003.
- [21] T. Sakuma, *Inclusive Jet and Dijet Production in Polarized Proton-Proton Collisions at  $\sqrt{s} = 200$  GeV at RHIC*. PhD thesis, Massachusetts Institute of Technology, 2010.
- [22] L. Kochenda, S. Kozlov, P. Kravtsov, A. Markov, M. Strikhanov, B. Stringfellow, V. Trofimov, R. Wells, and H. Wieman, “STAR TPC gas system,” *Nucl. Instrum. Meth.*, vol. A499, pp. 703–712, 2003.
- [23] M. Anderson *et al.*, “The Star time projection chamber: A Unique tool for studying high multiplicity events at RHIC,” *Nucl. Instrum. Meth.*, vol. A499, pp. 659–678, 2003.
- [24] F. Bergsma *et al.*, “The STAR detector magnet subsystem,” *Nucl. Instrum. Meth.*, vol. A499, pp. 633–639, 2003.
- [25] M. Beddo *et al.*, “The STAR barrel electromagnetic calorimeter,” *Nucl. Instrum. Meth.*, vol. A499, pp. 725–739, 2003.
- [26] C. Allgower *et al.*, “The star endcap electromagnetic calorimeter,” *Nuclear Instruments and Methods in Physics Research Section A: Accelerators, Spectrometers, Detectors and Associated Equipment*, vol. 499, no. 2, pp. 740–750, 2003.

- [27] J. Kiryluk, “Local polarimetry for proton beams with the STAR beam beam counters,” in *Spin physics. Polarized electron sources and polarimeters. Proceedings, 16th International Symposium, SPIN 2004, Trieste, Italy, October 10-16, 2004, and Workshop, PESP 2004, Mainz, Germany, October 7-9, 2004*, pp. 718–721, 2005.
- [28] W. J. Llope *et al.*, “The STAR Vertex Position Detector,” *Nucl. Instrum. Meth.*, vol. A759, pp. 23–28, 2014.
- [29] C. Adler, A. Denisov, E. Garcia, M. Murray, H. Strobele, and S. White, “The RHIC zero-degree calorimeters,” *Nuclear Instruments and Methods in Physics Research A*, vol. 461, pp. 337–340, Apr. 2001.
- [30] F. Bieser *et al.*, “The STAR trigger,” *Nucl. Instrum. Meth. A*, vol. 499, pp. 766–777, March 2003.
- [31] M. Cacciari, G. P. Salam, and G. Soyez, “The Anti- $k_T$  jet clustering algorithm,” *JHEP*, vol. 0804, p. 063, 2008.
- [32] B. B. Abelev *et al.*, “Charged jet cross sections and properties in proton-proton collisions at  $\sqrt{s} = 7$  TeV,” *Phys. Rev.*, vol. D91, no. 11, p. 112012, 2015.
- [33] M. Cacciari and G. P. Salam, “Pileup subtraction using jet areas,” *Phys. Lett.*, vol. B659, pp. 119–126, 2008.
- [34] T. Sjostrand, S. Mrenna, and P. Z. Skands, “PYTHIA 6.4 Physics and Manual,” *JHEP*, vol. 05, p. 026, 2006.
- [35] S. Agostinelli *et al.*, “GEANT4: A Simulation toolkit,” *Nucl. Instrum. Meth.*, vol. A506, pp. 250–303, 2003.
- [36] Z. Chang, *Inclusive Jet Longitudinal Double-Spin Asymmetry ALL Measurements in 510 GeV Polarized pp Collisions at STAR*. PhD thesis, Texas A and M University, 2016.
- [37] J. K. Adkins, *Studying Transverse Momentum Dependent Distributions in Polarized Proton Collisions via Azimuthal Single Spin Asymmetries of Charged Pions in Jets*. PhD thesis, University of Kentucky, 2017.
- [38] O. Jinnouchi *et al.*, “Measurement of the analyzing power of proton-carbon elastic scattering in the CNI region at RHIC,” in *Spin physics. Polarized electron sources and polarimeters. Proceedings, 16th International Symposium, SPIN 2004, Trieste, Italy, October 10-16, 2004, and Workshop, PESP 2004, Mainz, Germany, October 7-9, 2004*, pp. 515–518, 2004.
- [39] H. Okada *et al.*, “Measurement of the analyzing power A(N) in pp elastic scattering in the CNI region with a polarized atomic hydrogen gas jet target,” 2006.
- [40] R. D. Ball *et al.*, “Parton distributions for the LHC Run II,” *JHEP*, vol. 04, p. 040, 2015.

- [41] J. Adams *et al.*, “Measurements of transverse energy distributions in Au + Au collisions at  $\sqrt{s_{NN}} = 200$  GeV,” *Phys. Rev.*, vol. C70, p. 054907, 2004.

## VITA

Suvarna Ramachandran

### Place of Birth:

Kerala, India

### Education:

University of Kentucky  
Lexington, KY  
M.S., Physics  
December 2013

University of Hyderabad  
Telangana, India  
M.Sc., Physics  
June 2009

CMS College  
Kerala, India  
B.Sc., Physics  
June 2007

### Professional Positions:

University of Kentucky  
Research Assistant  
August 2012 - Present

University of Kentucky  
Teaching Assistant  
August 2010 - July 2012

**Publications:**

"Probing Gluon Helicity with Dijets from  $\sqrt{s} = 500$  GeV Polarized Proton Collisions at STAR", S. Ramachandran, *PoS*, **231** (2016).